COO-2218-150/EPRI-AFR-120

A STUDY OF FUSION PRODUCT EFFECTS IN FIELD-REVERSED MIRRORS

BY

DANIEL EDWARD DRIEMEYER

B. S., University of Illinois, 1974
M. S., University of Illinois, 1975

THESIS

Submitted in partial fulfillment of the requirements
for the degree of Doctor of Philosophy in Nuclear Engineering
in the Graduate College of the
University of Illinois at Urbana-Champaign, 1980

Urbana, Illinois

DISCLAIMER

A STUDY OF FUSION PRODUCT EFFECTS IN FIELD-REVERSED MIRRORS

Daniel Edward Driemeyer, Ph.D.
Nuclear Engineering Program
University of Illinois, 1980

The effect of fusion products (fps) on Field-Reversed Mirror (FRM) reactor concepts has been evaluated through the development of two new computer models. The first code (MCFRM) treats fps as test particles in a fixed background plasma, which is represented as a fluid. MCFRM includes a Monte Carlo treatment of Coulomb scattering and thus provides an accurate treatment of fp behavior even at lower energies where pitch-angle scattering becomes important. The second code (FRMOD) is a steady-state, globally averaged, two-fluid (ion and electron), point model of the FRM plasma that incorporates fp heating and ash buildup values which are consistent with the MCFRM calculations. These values are obtained by expressing the fp energy and particle retention in the closed field region in terms of the fraction of marginally confined fps (i.e., those fps that can interact with both the open and closed field plasma but still do not have a "loss cone"). Both codes employ an approximate representation of the field-reversed equilibrium based on Hill's vortex model.

These codes have been used extensively in the development of an advanced-fuel FRM reactor design (SAFFIRE). These studies show that a significant amount of fp energy (and associated ash) deposition occurs in the closed field region of the FRM, despite the relative small size of the plasma (radius equal ~ 5 to 15 ion gyroradii). Typically 50% of the fp energy (and the resulting thermal fps) are deposited in the closed field region of the reference SAFFIRE designs. This is particu-

larly important from the standpoint of advanced-fuel operation, where attractive ($Q > 10$) systems are found within the current "stable" limits on the plasma size, together with the possibility of "ignited" operation if the present stability limits are extended by 50%. These results are illustrated through a discussion of the SAFFIRE reactor optimization studies and through several summaries of reference case reactor parameters. Typical parameters for a D-^{3}He type SAFFIRE plant cell are: 2.3 MW from a 3/1 elongated, 21.5-cm mirror radius plasma, with ion and electron temperatures of 80 and 75 keV and a plasma ion density of $4.4 \times 10^{14} cm^{-3}$. Larger powers can be obtained by stacking cells.

A Catalyzed-D version of the plant is also discussed along with an investigation of the steady-state energy distribution of fps in the FRM. User guides for the two computer codes are also included.

ACKNOWLEDGMENTS

It is the author's distinct pleasure to gratefully acknowledge the several years of encouragement and support provided by many individuals in the course of this research. In particular, I wish to thank my thesis advisor, Professor George Miley, for his guidance and encouragement. This effort could not have been completed without them. I would also like to thank Dr. W. C. Condit of Lawrence Livermore Laboratory. His advice and assistance are deeply appreciated. In addition, the cooperation and interest of Doctors Jack Byers, Gustav Carlson, Stephen Devoto, Thomas Kaiser, Ralph Moir, Thomas Rognlien, Adrian (Chip) Smith and Mr. Terry Chu, all of Lawrence Livermore Laboratory, are noted with special thanks. The unselfish consideration of the members of the Nuclear Engineering faculty, in particular Doctors John Gilligan and Chan Choi, is also appreciated.

Many of the author's fellow students have aided in the completion of this project through stimulating discussions both of a technical and general nature. A list of names would be too long and probably left incomplete; however, the mention of the NRL II lounge and 304 Ceramics should allow these individuals to identify themselves.

A special note of thanks should also be given to Mrs. Chris Stalker for her assistance in the typing and compilation of this manuscript. Her positive attitude and patience have always been appreciated.

Finally, the author wishes to thank his family for their moral and financial support throughout the years. This goal would never have been achieved without their love and encouragement. In particular, I wish to thank my wife, Jamie, for her love and patience. Her unselfish and positive attitude have made the completion of this work an enjoyable experience.

TABLE OF CONTENTS

CHAPTER 1

INTRODUCTION

1.1 Background

Closed field line geometries, where all of the field lines that penetrate the plasma never intercept a wall, have always appeared to be one of the best ways of obtaining the long confinement times required for fusion. Because particles must diffuse across field lines to be lost from a closed field system (e.g. a tokamak) their loss rate is much slower than that for an open ended system such as a mirror. Therefore, in the short term, tokamaks are more attractive, because they are closer to demonstrating the plasma conditions necessary for fusion; namely, a temperature of ~10-keV, and a product of density and confinement time ($n\tau$) that surpasses the Lawson criterion of $\sim 1.0 \times 10^{14}$ sec/cm^3. Mirrors do, however, offer some key advantages over tokamaks in other areas. The most significant of these is their high β (defined as the ratio of the average plasma pressure to the vacuum

magnetic pressure). This allows the mirror to provide a higher plasma density than is possible in a tokamak with the same magnetic field strength, and can thus lead to both size and cost reductions. In addition, the higher density reduces the confinement time required for breakeven, but the classical mirror still falls only marginally beyond the Lawson criterion.

A second advantage of the mirror is its ease of coupling to a direct energy conversion system. This is important because direct conversion is only possible in tokamaks through the use of complicated divertors, which can represent a significant power drain on the system [1]. The mirror is thus ideally suited for burning advanced fuels, where the increased fraction of the fusion energy released in the form of charged particles can lead to much higher overall plant efficiencies. The high β helps to offset the reduced power density resulting from the smaller fusion cross sections and also lowers the cyclotron emission, which becomes significant at the higher temperatures required for advanced fuels. The mirror thus seems to be a more attractive fusion reactor concept, if a means of reducing its loss rates can be found.

Research in the mirror program has therefore focused upon the identification of an effective means of "stoppering" the ends of the mirror, so that its loss rates are more in line with those of a closed field system. Several means of accomplishing this have been suggested; however the most effective are currently thought to be the tandem mirror (TM) [2], and the field-reversed mirror (FRM) [3] concepts. In the TM a long, low density solenoid is electrostatically stopped by the potential

of two small, high density mirror plugs; while in the FRM, the ends are closed by creating a current in the plasma which reverses the vacuum mirror field along the magnetic axis. As is shown in Fig. 1, this results in a region of closed field lines surrounded by a diverting mirror field. The FRM thus combines the good confinement of closed field systems with the high β and natural diverting action of a mirror to produce an extremely attractive device. The only drawback it has is a reliance upon finite orbit effects for stability, which limits the plasma size to some small number of ion gyroradii; typically less than 10. This limitation reduces the economy of scale for the FRM; however it can be offset by combining individual cells into larger power multiple-celled FRM systems.

1.2 History

The concept of reducing the end losses in a mirror confinement scheme by reversing the magnetic field along its axis was originally proposed by Christofilos [4] and McNally [5,6]. In this "Astron" concept, a layer of relatavistic particles, whose gyro-orbits encircled the magnetic axis, provided both confinement and heating of a background plasma which was needed for space charge neutralization. The current of the relativistic particles created a region of closed field lines, localized by a weak magnetic mirror, that reduced the background losses and thus allowed it to be heated to fusion temperatures. The attractiveness of this concept caused it to be the subject of experimental and theoretical investigations at Lawrence Livermore

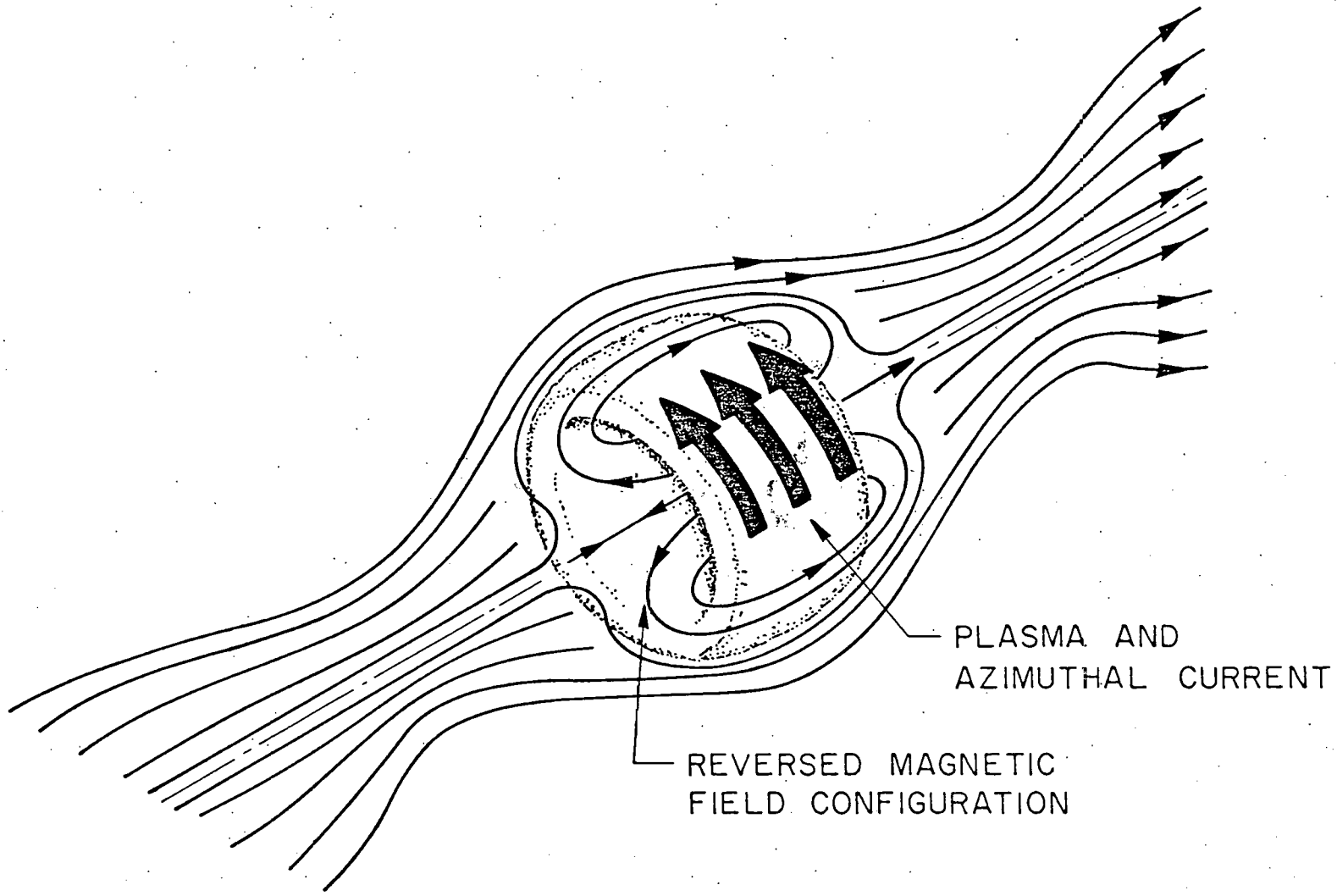

Figure 1. Typical Field-Reversed Mirror Plasma Geometry.

Laboratory (LLL) throughout the 1960's and the early 1970's [7-9]. Potential reactor designs were promising, Fig. 2; however the units were large in size (5-6GWe), and dependent upon the development of high power (600MW), relativistic ion beam sources which meant that they were not compatable with near-term technology. In addition, the experimental Astron program at LLL was was also meeting with little success. Its elongated plasma layers exhibited tearing instabilities which caused them to break up into shorter layers before full reversal was reached. The shorter layers were more stable, but they did not contain enough current to create a closed field configuration. Therefore, the Astron program at LLL was eventually abandoned.

Related experimental work continued at Cornell University, however, and the existence of stable field-reversed equilibria was finally demonstrated by Fleischman and co-workers [10]. Similar results have also been observed in an experiment at the Naval Research Laboratory (NRL) [11], and therefore, field-reversal in the Astron limit is now a well accepted phenomena. The success of these later experiments is mainly attributed to the fact that the reversal current is built up on a much faster timescale than was possible in Astron. This is due to the injection of a single, high current pulse in the NRL and Cornell experiments, as compared to the pulse stacking technique used in Astron, and the resulting fast rise time seems to allow reversal to develop before instabilities. Two more subtle differences are also felt to contribute to the improved results. The first is that the NRL and Cornell equilibria are shorter and fatter than the Astron configuration, and the second is the presence of a quadrupole barrier in the later

FSL-79-195

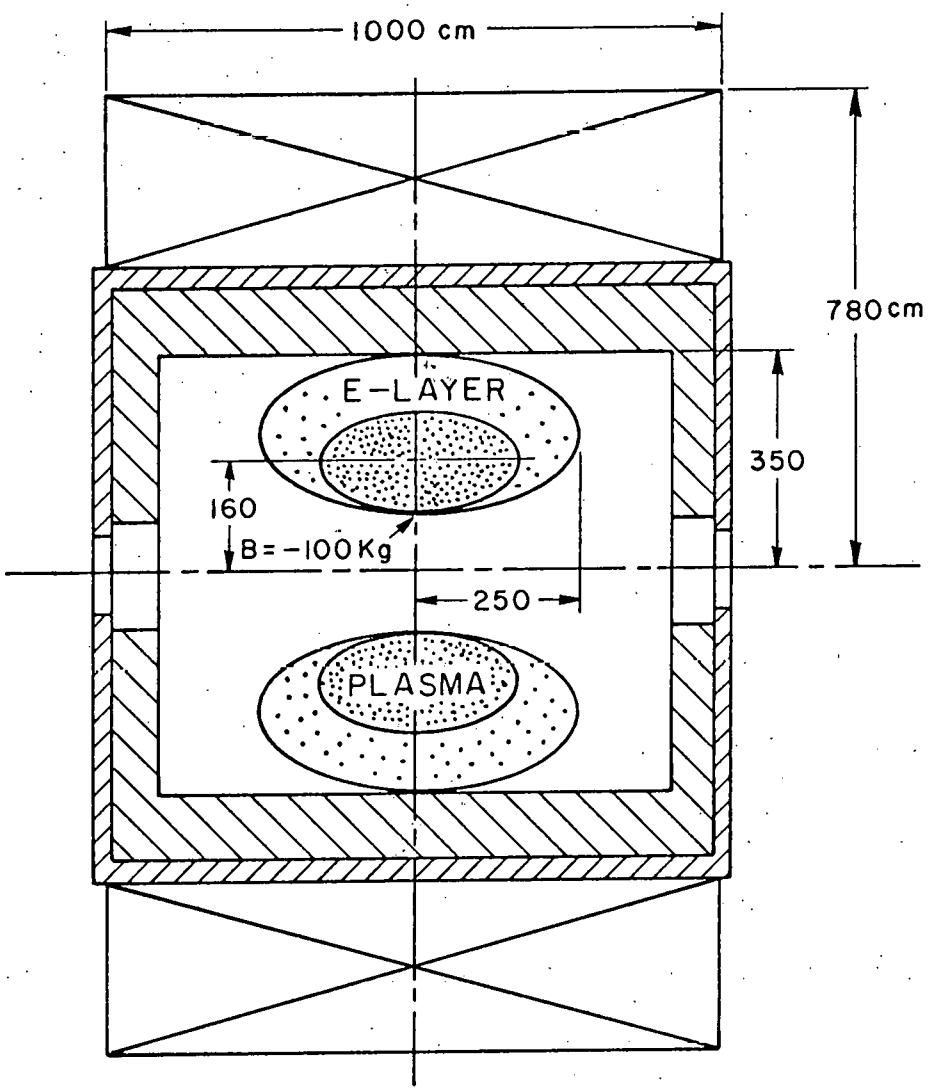

Figure 2. Cross Section of the Conceptual ASTRON Reactor. Note how the background plasma is embedded in the E-layer.

experiments. These characteristics are all thought to lead to enhanced stability in FRM goemetries, and are thus the subject of ongoing FRM stability studies, as discussed in the next section.

In these Astron-like configurations, the azimuthal (reversal) current is provided almost entirely by the axis-encircling relativistic particles. However, in the course of the Astron theoretical work, it was noted that the background particles could also carry a significant fraction of the reversal current via their diamagnetic effect [8,9]. The FRM then lies at the ultimate limit of this process, with the reversal current supplied entirely by the net drift motion of the background plasma. The quantitive distinction between an Astron geometry and an FRM is, therefore, best made on the basis of the number of ion gyroradii included in the minor radius of the plasma. If the gyroradius ρ (based on the mean plasma energy and the vacuum field) is much less than the minor radius a, the plasma would be considered an FRM. If however there is a class of high energy particles with $\rho > a$, the plasma is an Astron-like device.

Evidence of field-reversed equilibria in the FRM limit is also available. It comes from field-reversed theta pinch (FRTP) experiments at Los Alamos [12], the Kurchatov Institute [13], and from earlier work by Eberhagen and Grossman [14]. In these experiments, a reversed field geometry is obtained by superimposing a magnetic field on the initial plasma, and then starting the main theta pinch discharge with reversed direction. The resulting plasma configuration is shown in Fig. 3a. Soon after the start of the discharge, the field lines reconnect at the

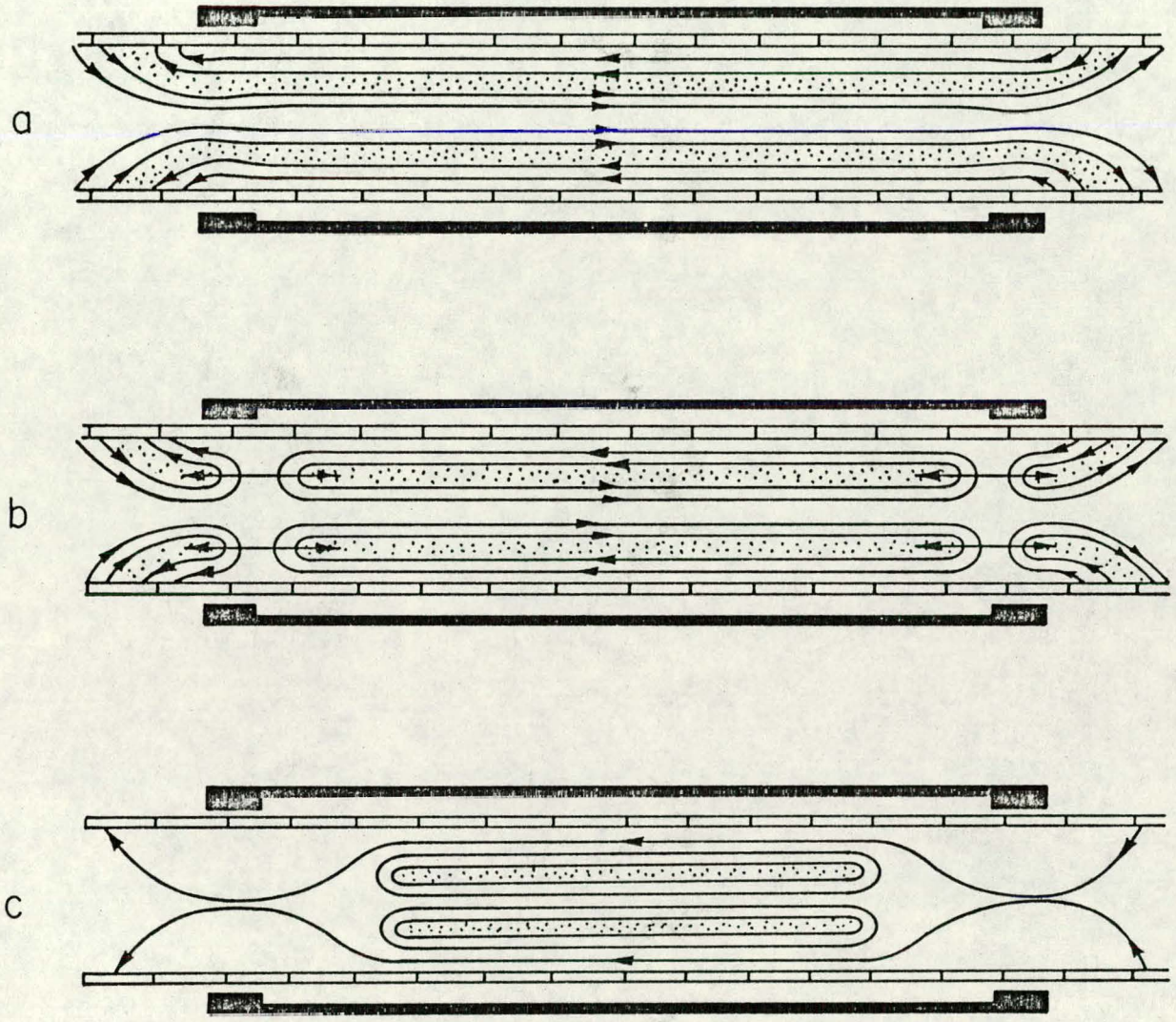

Figure 3. Illustration of FRTP Startup. In (a) the initial configuration, with trapped anti-parallel fields, is shown just after the main discharge was fired. By (b), the ends of the plasma have pinched off, and the resulting field-reversed layer is contracting towards the mid-plane. This produces the final configuration shown in (c).

ends of the chamber, and the remaining annular layer then contracts towards the mid-plane of the coil under the action of the enclosing field lines, Fig. 3b. This produces an FRM-like plasma, Fig. 3c, with a lifetime equal to a few hundred sound transit times across its major radius. FRTP experiments are thus often cited as an indication of FRM stability, because this lietime is long compared to MHD growth rates.

These encouraging results generated renewed experimental and theoretical interest in field-reversal at LLL. The original SUPERLAYER code, developed for the Astron program, was modified to simulate neutral injection [15] and was used to study possible buildup to field-reversal in mirror machines. Reversal was predicted for the 2X-IIB experiment but was never attained. Sufficient current built up to reach marginal reversal, i.e., zero field at the center of the device, but the injectors were unable to drive the plasma past this point. Instead, the plasma seemed to be dumping the injected energy into microinstabilities. This failure was discouraging; however it may only be an indication that the intermediate state between field-reversal and the normal mirror mode is unstable. It may therefore be possible to drive a mirror into a reversed state on a faster timescale than that in which microinstabilities can occur, and work is continuing at LLL on the development of a fast pulsed, ion-neutral source (IPINS), which will allow investigation of fast start-up scenarios.

1.3 Stability

The above experimental results indicate that stable field-reversed configurations may exist in both the Astron and FRM limits. However, it is clear that if typical gradient lengths become large compared to a gyroradius; the configuration is adequately described by the magnetohydrodymanic (MHD) equations and is unstable due to its inherent bad curvature. Ongoing theoretical work [16,17] has been attempting to develop a theory which predicts stability limitations in the FRM limit, but this effort has been hampered by an inadequate understanding of particular experimental characteristics which may have contributed to stability. Conclusions drawn from these studies are therefore somewhat preliminary. Thus, it is more customary to rely upon the experimental results which indicate that the FRM configuration is stable if S (defined as the ratio of the plasma radius to the average ion gyroradius) is less than 10. Here the plasma radius is taken to be some measure of typical density and magnetic field gradient lengths found in the FRM, and S is then an indication of the applicability of MHD theory.

Many of the questions regarding conceptual FRM studies center on the above stability arguments. This is because long experimental lifetimes in the FRM-limit have only been observed by the Russians [13]. The remaining FRTP experiments exhibit gross MHD stability, i.e., are resistant to m = 0 tearing modes; however they eventually are disrupted by an m = 2 rotational instability, which sets in after ~25-μs of quiescient operation. (Here m is the mode number of the instability

which is used to describe its azimuthal dependance; thus m = 0 corresponds to axisymmetric "tearing" modes, m = 1 to "kinking" modes, and m = 2 to "fluting" modes. Normally m = 2 modes are associated with disruptive plasma rotations, such as those observed in the FRTP experiments.) Linford, et al, have exerted considerable effort in an attempt at duplicating the longer Russian lifetime of ~100-μs but have, thus far, been unsuccessful. The reason for the Russian lifetime is unclear but is thought to be due to their strong multipole barrier field, which keeps the plasma away from the wall during the initial stages of its formation. Therefore, additional experiments which include a stronger barrier field are planned at Los Alamos in an effort to finally verify the Russian result.

In the Astron limit, theoretical studies have been more successful. Sudan [18] and Lovelace [19] have investigated the stability properties of ring-like equilibria for bicycle tire and elongated geometries and predicted instability in both cases, which is consistent with results from both the Astron and Cornell experimental programs. More recently, Finn [20] has addressed the stability of the short, fat rings which are observed to persist experimentally and identified several new classes of equilibria. Therefore, the gross MHD stability of field-reversed equilibria seems to be accepted; however Morse [17] postulates that slow growth-rate MHD modes are still possible. He suggests that these modes will saturate in some form of enhanced transport which dissipates the free energy being released by the instability. This seems to be consistant with results from the FRTP and Cornell experiments because the "driving force," in both cases, is thought to be the thermal spread

in the mean azimuthal velocity. The thermal spread is much greater in the FRTP and thus a shorter lifetime is expected, which agrees with the experiment. Several important effects are, however, not included in Morse's analysis. These include quadrupole fields, plasma elongation, and radial electric fields, all of which could stabilize the the FRM against the m = 2, low growth-rate modes he predicts.

1.4 Other FRM Reactor Studies

In order to determine the potential of the FRM as a fusion reactor, a preliminary design study was begun at LLL for a D-T fueled system [21]. Their plasma model was based on the similarity between the FRM magnetic geometry and a tokamak. This led to the assumption of a diffuse (cubic or parabolic) density profile together with a uniform plasma temperature, which allowed the steady-state, two-fluid (ion and electron) particle and energy balance equations to be reduced to zero-dimensional form. Pressure balance was satisfied by choosing a value for β (normally 1.5), and losses were then calculated in accordance with a variety of transport rates, with refueling and heating being provided by neutral beam injection. This study indicated that the FRM was an exciting reactor concept; consequently a more detailed investigation was undertaken. It focused on improving the physics calculations (using the same basic model) and developing a more complete engineering evaluation. Size and cost estimates were made over a wide range of physics parameters, and an in depth "reference design" was completed. A detailed discussion of this work is presented in Ref. 22;

however a brief summary of the results is presented here. The final design consisted of 11 FRM cells stacked together along the axis of a long superconducting solenoid. Each cell produced 20MW of fusion power and required the injection of 3.6MW of 200-keV D and T. The reactor had a net electric output of 76MWe and cost $1200/KWe.

At the same time, a related FRM concept was also being investigated at LLL. It was based on the relativistic-ring work going on at Cornell and was called the moving ring field-reversed mirror (MRFRM). In the MRFRM, relativistic proton layers are continually being formed and set in motion down a long solenoidal guide field. As the rings move, they are compression-heated until they reach ignition, at which time they enter a reaction chamber. The fusing plasma is refueled via pellet injection as it moves through the reaction chamber, and the burn continues until it is quenched by ash buildup. The plasma is then exhausted into an expansion region, where its energy is extracted through direct conversion. The key issues are thus the burn time and the net energy gain per ring; therefore a Fokker-Planck model was developed in this case so that the dynamics of the burn could be accurately investigated. A detailed description of the MRFRM work is given in Ref. 23.

1.5 This Work

The encouraging results reported by LLL in their preliminary reactor design study [21] generated interest in the FRM as an advanced-fuel

reactor concept at Illinois. This formed the impetus for the work presented here. It was desired to modify the LLL study to include a more "self-consistent" plasma model, and to provide an accurate calculation of the effect of fusion products (fps) on the FRM plasma. The first objective was attained through the use of the Hill's spherical vortex description of the FRM plasma [24]. This simple analytical model provides a convenient base for developing a series of survey-type calculations and is also comparable to the model used by Livermore (which is based on results obtained from the plasma simulation code SUPERLAYER), as shown in Fig. 4. "Self-consistency" is provided by calculating a background pressure profile from the Hill's vortex field structure and using this to reduce the steady-state plasma particle and energy balances to averaged zero-dimensional form.

The second objective was attained through the development of a Monte Carlo computer model of fp behavior in FRM plasmas (MCFRM) [25]. It couples the Hill's vortex representation of field-reversal with a Monte Carlo treatment of Coulomb scattering and thus provides a complete picture of fp thermalization; even at lower energies where pitch-angle scattering becomes important. A related technique has previously been used in the case of neutral-beam injection into tokamak plasmas [26]; however this is the first time such methods have been applied to the problem of fp behavior in FRMs. The code has allowed fp heating and associated ash buildup (i.e., thermalized fusion products that accumulate in the plasma, diluting the fusing species and, subsequently, reducing the fusion power density) in the closed field region of an FRM plasma to be evaluated and has shown that fps have a significant effect

FSL-79-113

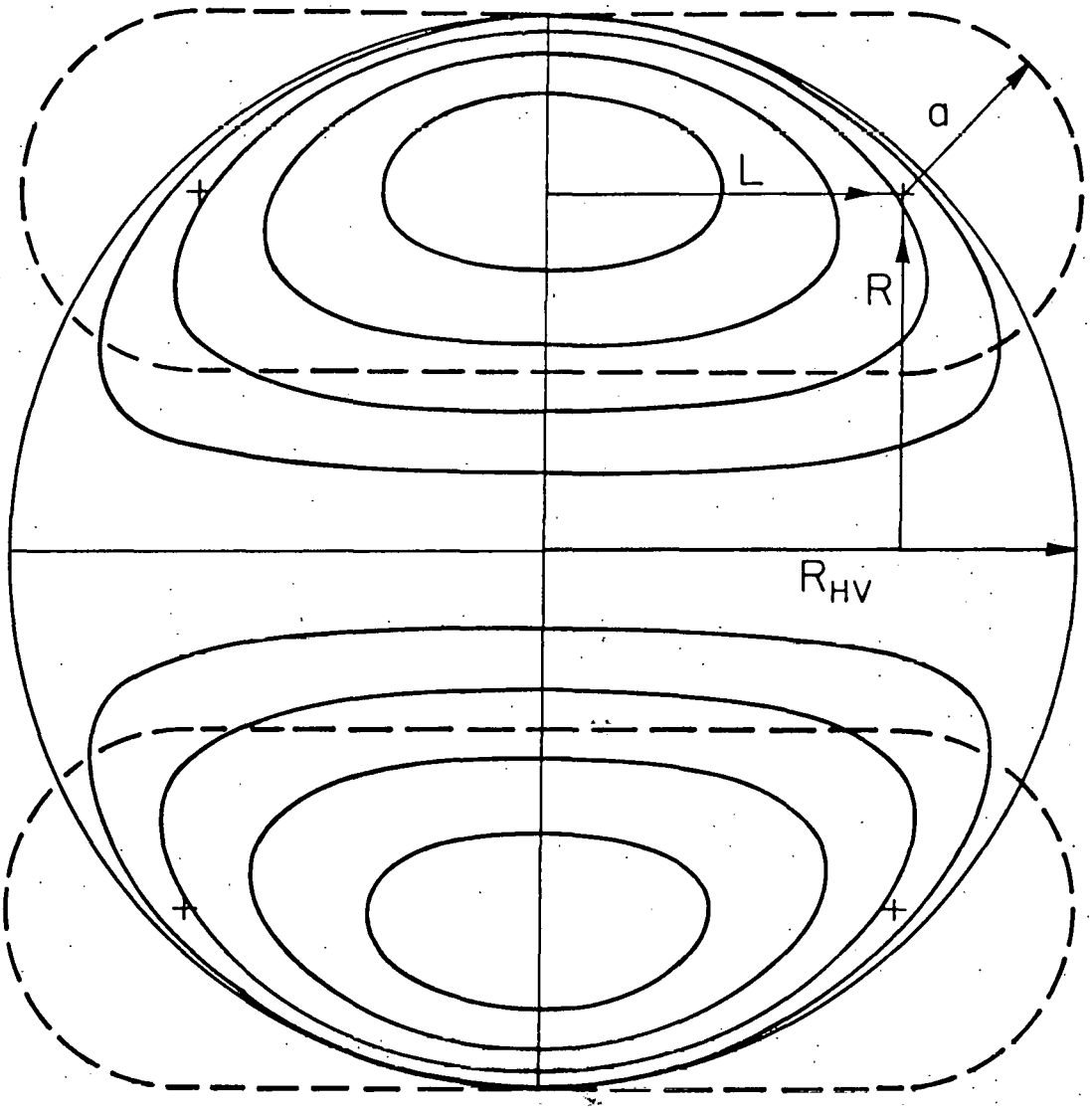

Figure 4. Comparison Between LLL (dashed) and Hill's Vortex (solid) FRM Plasma Geometries. Note that the LLL design, which has an elongation of 3/1 is nearly equivalent to a spherical vortex plasma.

on the steady-state particle and energy balances. (This latter result was not expected due to the small size of the plasma--radius equal only a few ion gyroradii.) The code has also formed the basis for several ongoing studies involving the calculation of fp distribution functions in order to determine if fps affect the plasma equilibrium by driving microinstablities or by altering the reversal current.

The remainder of this work describes the details of these two computer models and is organized in the following manner. Chapter 2 gives an introduction into the Hill's vortex analogy and describes the preliminary analytical work that went into the model development. Chapter 3 describes the Monte Carlo particle code MCFRM, along with several test cases which were run in order to establish the validity of the model. Chapter 4 covers the averaged, global model, FRMOD, and the means of coupling the two codes together in order to obtain a more consistent result. Chapter 5 contains a summary of the results and their implications regarding the SAFFIRE reactor design, and Chapter 6 makes some concluding remarks and recommendations for future work. Finally, since the codes are generally applicable to other problems concerning the overall FRM system, two appendices are included which are intended to serve as guides for individuals wishing to utilize the codes.

CHAPTER 2

THE HILL'S VORTEX MODEL

2.1 The Field Structure

As originally pointed out by Morse [27] and implemented by Wang and Miley [28], the steady-state FRM is expected to assume a configuration much like the Hill's spherical vortex. This simple analytical model was originally proposed by M.J. Hill in 1894 to describe vortex formation in fluid flow [24]; however it is completely analogous to a spherical field equilibrium, as was later noted by Shafranov [29]. The original formulation was only for the spherical case; but because many of the experimentally produced field-reversed plasmas are elongated, the model has been modified slightly for this application to include a factor κ which stretches the equilibrium in the axial direction. The elongation factor is included self-consistently throughout the model by first "stretching" the magnetic flux function ψ, which consequently takes on the following form:

$$\psi(r,z) = \begin{cases} -(3/4)B_o R_{HV}^2 \, r^2(1-R^2) & R \leq 1 \quad (1a) \\ (1/2)\, B_o R_{HV}^2 \, r^2(1-R^{-3}) & R > 1. \quad (1b) \end{cases}$$

Here $R = (r^2+z^2/\kappa^2)^{1/2}$; $\kappa = z_m/R_{HV}$ is the elongation factor; r and z are dimensionless cylindrical coordinates normalized to the radius of the seperatrix, R_{HV}; and B_o is the vacuum magnetic field strength. The flux is then negative for $R < 1$ (due to the reversed magnetic field), goes through zero at $R = 1$ (the seperatrix), and asymptotically approaches the solenoidal form of $B_o R_{HV}^2 r^2/2$ for $R > 1$.

The magnetic field corresponding to this flux is then determined from the relation $\vec{B} = \vec{\nabla}\psi \times \hat{\theta}/rR_{HV}$ and is therefore:

$$\vec{B}(r,z) = \begin{cases} -3B_o/2[rz/\kappa^2)\hat{r} + (1-R^2-\iota^2)\hat{z}] & R \leq 1 \quad (2a) \\ -3B_o/2[(rz/\kappa^2R^5)\hat{r} + (2/3-2/3R^3+r^2/R^5)\hat{z}] & R > 1. \quad (2b) \end{cases}$$

This elongated field configuration, shown in Fig. 5 for $\kappa = 2.5$, has the following characteristics:

1. As expected, it is reversed along the axis of the mirror, with a field strength of 3/2 the vacuum value at $z = 0$, and with field nulls at $z = \kappa$.

2. There is another ring-shaped field null, (that corresponds to the minimum in the magnetic flux function, and consequently to the maximum in the plasma pressure) embedded in the closed field region at $z = 0$, with a radius of $1/\sqrt{2}$.

3. There is a strong field gradient in the $z = 0$ plane, moving outward from this null, that causes the field strength to also reach 3/2 its vacuum value at the closed field boundary, $R = 1$.

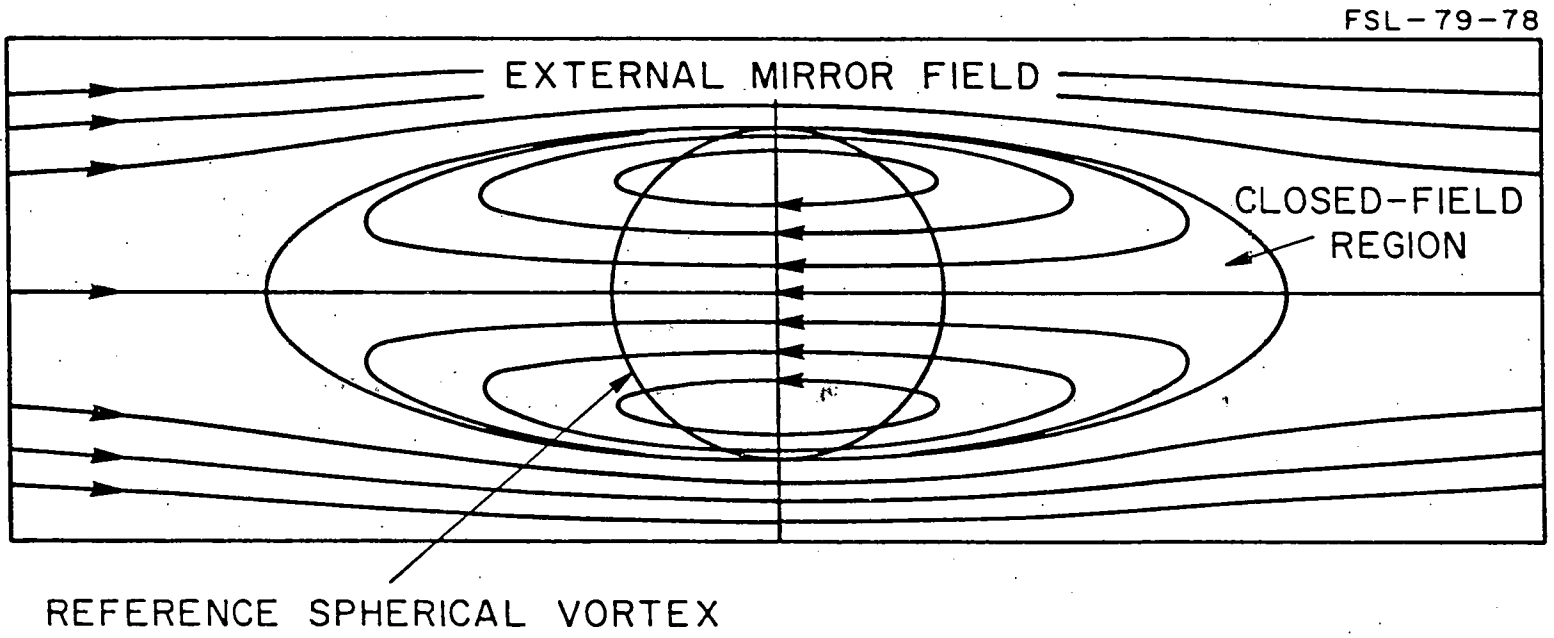

Figure 5. Elongated Hill's Vortex Representation of the FRM Geometry. For this case the elongation factor κ is 2.5.

4. The field outside this boundary, $R > 1$, approaches a straight solenoidal structure as $1/R^3$.

The current density required to maintain this field configuration can be calculated using Ampere's law, viz. $\vec{j} = (c/4\pi)\,\vec{\nabla}\times\vec{B}$. This results in:

$$j(r,z) = \begin{cases} \dfrac{-3cB_o}{8\pi R_{HV}}\,(4+\kappa^{-2})\,r\hat{\theta} & R \leq 1 \qquad (3a) \\ \dfrac{3cB_o}{8\pi R_{HV}}\,(1-\kappa^{-2})\,r\,(r^2-4z^2/\kappa^2)/R^7\hat{\theta} & R > 1, \qquad (3b) \end{cases}$$

The complicated magnetic configuration is thus produced by a relatively simple current density, which is linearly increasing with r inside the seperatrix and falling off as R^4 outside it (the seperatrix is at $R = 1$). (For the spherical case, $\kappa = 1$, no current is required outside the seperatrix.) This current density has been shown in Fig. 6 at several axial positions, for the $\kappa = 2.5$ case. These illustrate that the elongated Hill's vortex analogy begins to break down near the seperatrix due to the current (or equivalently a plasma pressure gradient) that is required on the open field lines. The vortex configuration is, therefore, not completely consistent, but (based on the SUPERLAYER comparison discussed in the next paragraph) it has been retained because it provides a realistic (and simple) picture of the complicated FRM field structure. If a completely consistent, analytic description of an elongated equilibrium is desired (i.e., one where no pressure gradient is required on the open field lines), it can be found in Ref. 30.

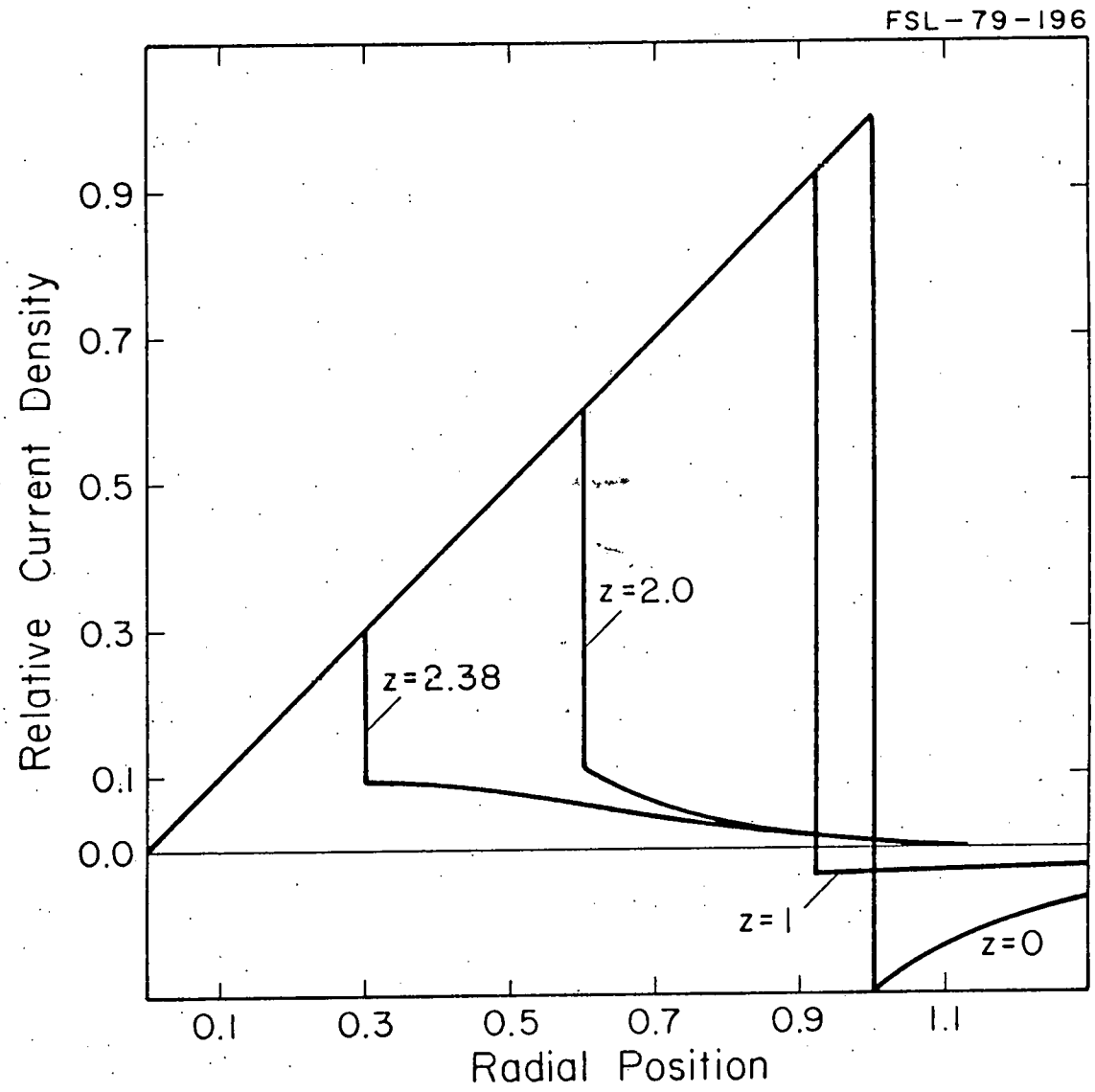

Figure 6. Plasma Current Density Profiles Required to Maintain the Elongated Hill's Vortex Structure for $\kappa = 2.5$.

The main justification for the use of the elongated Hill's vortex model thus comes from its similarity to actual FRM equilibria predicted by the plasma simulation code SUPERLAYER [15]. This two-dimensional particle code solves for the self-magnetic field generated by the ions, and the resulting ion orbits in this field. (Presently, the code ignores the effects of local space charge buildup, electron currents and electrostatic fields, all questionable assumptions, but it has accurately predicted both the failure of Astron and the success of the Cornell experiments; therefore it is thought to provide a reasonable picture of FRM physics.) A self-consistent magnetic configuration is then obtained by setting up a fixed spatial grid structure and solving for the single-component vector potential A_θ. This allows the plasma equilibrium to be evolved in time until reversal is fully developed thus providing a valuable check on the Hill's vortex formulation.

A typical SUPERLAYER field plot is therefore shown in Fig. 7. The vortex field model is found to compare quite favoribly with the SUPERLAYER field structure even though it is a fluid equilibrium and is thus not strictly consistent with the large orbits found in the FRM. This visual argument together with the simple analytical nature of the vortex field model have led to its application in the present study. It should be pointed out, however, that the techniques developed here are completely general. They are not dependent upon the choice of the Hill's vortex representation of the FRM; consequently other descriptions of the field-reversed equilibrium could be substituted for future work if desired.

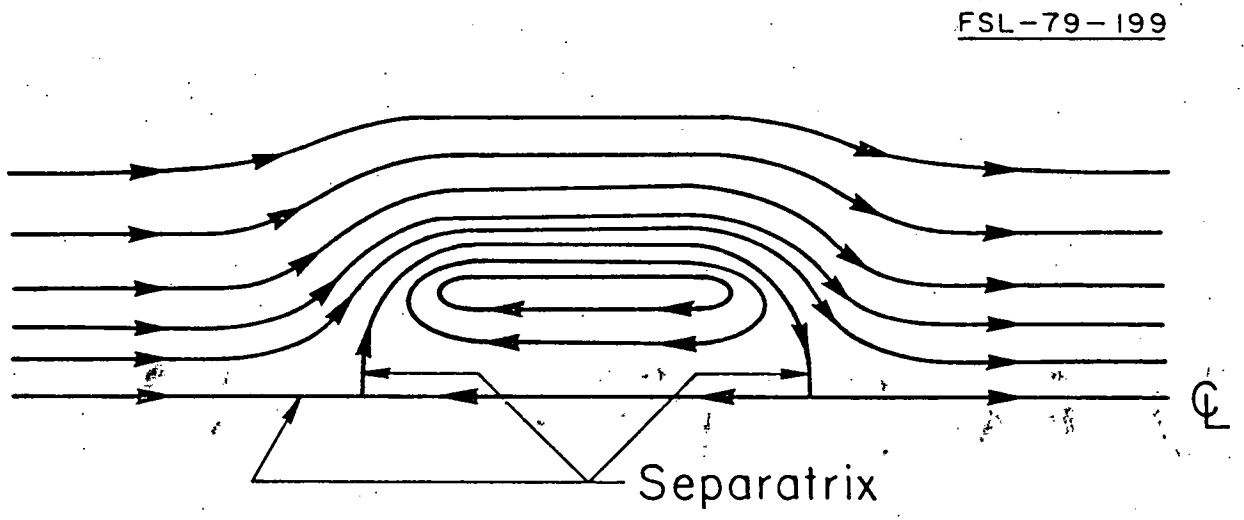

Figure 7. Typical Field-Reversed Equilibrium Calculated by the Plasma Simulation Code SUPERLAYER.

2.2 Particle Motion and the Effective Potential

Because the FRM geometry is axially symmetric, it can be represented by a single component vector potential $\vec{A} = A_\theta(r,z)\hat{\theta}$, where $A_\theta = \psi/R_{HV}r$. Particle motion in this geometry is then described simply by their Lagrangian which is:

$$L = \frac{m}{2}(\dot{r}^2 + r^2\dot{\theta}^2 + \dot{z}^2) + \frac{q}{c} r\dot{\theta}A_\theta \quad . \tag{4}$$

Here q and m are the particles charge and mass respectively; r, θ and z are now dimensional cylindrical coordinates; c is the speed of light; and the dot has been used to denote the derivative with respect to time. The equations of motion can then be shown to be:

$$m\ddot{r} = P_\theta^2/rm - (q^2/2m)\frac{\partial}{\partial r}(A_\theta^2) + (qP_\theta/m)\frac{\partial}{\partial r}(A_\theta/r) \tag{5}$$

$$m\ddot{z} = -(q^2/2m)\frac{\partial}{\partial z}(A_\theta^2) + (qP_\theta/m)\frac{\partial}{\partial z}(A_\theta/r) \tag{6}$$

$$P_\theta = mrv_\theta + \frac{q}{c} rA_\theta \quad , \tag{7}$$

where P_θ is the canonical angular momentum, which (if there is no Coulomb drag or scattering) is a constant of the motion. The introduction of P_θ thus reduces the complicated three-dimensional particle motion to a simpler two-dimensional projection in the r-z plane. Unfortunately, for most cases of interest, P_θ is not a true invariant due to Coulomb interactions; however for high energy particles, such as fusion products, P_θ varies slowly because drag effects are dominate. Therefore, the above equations give a good

approximation to the actual particle motion except at lower energies where pitch-angle scattering becomes important.

It is useful now to notice that these equations describe particle motion in the r-z plane, within an effective scalar potential defined by:

$$V = \frac{m}{2} v_\theta^2 = \frac{1}{2m}\left[\frac{P_\theta - q\psi/c}{r}\right]^2 \quad . \tag{8}$$

The energy of the particles can then be written in terms of this potential as:

$$E = \frac{m}{2}(v_r^2 + v_z^2) + V \quad . \tag{9}$$

This shows that particles can be absolutely confined in the FRM, i.e., no longer have a conventional mirror "loss cone," if the potential is such that $E < V$ within some closed region of configuration space. The boundary of this region is then determined by setting $E = V$, and is thus dependent upon the magnetic flux function, ψ, and the particle's canonical angular momentum, P_θ. Particles are confined within this "energy surface" because, from Eq. 9, their energy becomes entirely in the theta direction as they approach it, which prevents them from going beyond the boundary it represents. The convenience of this formulation was originally noted by Northrop, et al, [31,32] in discussing the problem of non-adiabaticity of particle orbits in a mirror field; however it is also well suited for this application, as the next few sections will show.

From the Hill's vortex expression for the magnetic flux, Eq. 1, the effective potential can be written as:

$$V = \begin{cases} \frac{1}{2r^2}\left[P_\theta + \frac{3}{4}r^2(1-R^2)\right]^2 & R \leq 1 \qquad (10a) \\ \frac{1}{2r^2}\left[P_\theta - \frac{1}{2}r^2(1-R^{-3})\right]^2 & R > 1 \quad . \qquad (10b) \end{cases}$$

In this dimensionless form R_{HV}, B_o, $B_o R_{HV}^2$, $qB_o R_{HV}^2/c$, and $(1/m)(qB_o R_{HV}^2/c)^2$ have been chosen as units for length, magnetic field, magnetic flux, canonical angular momentum, and energy respectively. Thus, a 3.5-MeV alpha particle in a 20-cm, 6.0-T spherical vortex would have a dimensionless energy of 0.0252, while a 200-keV injected deuteron's energy would be 0.0029. (These units will be used throughout the remainder of this work, since they lend themselves quite naturally to the problem.) The implications of this effective potential will now be discussed, especially as they pertain to fusion products (fps) in the FRM.

2.3 Absolute Confinement Theory

From simple energy arguments, it was shown that particles could be absolutely confined in the FRM geometry if their energy, E, was less than the effective potential, V, in some closed region of space. The specific condition for absolute confinement can then be established by examining the general form of the effective potential, Eq. 8. Since ψ is known to approach the solenoidal form of $B_o R_{HV}^2 r^2/2$ for large R, a potential barrier will always exist in the radial direction, and the

height of this barrier is given by the value of the potential at the wall, viz.

$$\lim_{r \to r_w} V = \frac{q^2 B_o^2 R_{HV}^2}{8mc} r_w^2 \quad . \tag{11}$$

Absolute confinement is then possible if there is also a potential barrier in the axial direction. Because ψ is positive everywhere outside the seperatrix, Eq. 8 shows that an axial barrier exists only if $P_\theta < 0$. (This is true for a large fraction of the particles in the FRM due to the reversed magnetic field which leads to negative values of ψ that allow $P_\theta < 0$, from Eq. 7.) To determine if this barrier is high enough to confine the particle, the "critical" value of V must be evaluated. This value corresponds to the absolute minimum in the potential and occurs at a radius, r_c, which is found from:

$$\left.\frac{\partial V}{\partial r}\right|_{r_c} = 0 \quad . \tag{12}$$

The asymptotic form of ψ can then be used to find that:

$$r_c^2 = - (2c/q\ B_o R_{HV}^2)\ P_\theta \quad . \tag{13}$$

Therefore, the critical value of the potential is found to be $-(qB_o/mc)P_\theta$, and the conditions for absolute confinement of a particle are thus:

$$P_\theta < 0 \tag{14}$$

$$E < - (qB_o/mc)\ P_\theta \quad . \tag{15a}$$

It is also possible to determine a condition for confinement completely within the closed field region. The boundary of this region is defined by $\psi = 0$, and the minimum value of V along this boundary is found to occur at $r = 1$. The critical potential for this case is then found to be $P_\theta/2mR_{HV}^2$, again from Eq. 8. Thus, the condition for closed-field confinement is:

$$E < P_\theta^2/2m\, R_{HV}^2 \quad , \tag{16a}$$

where the side condition on P_θ, Eq. 14, must still be satisfied. At first glance, this criterion does not appear to be more restrictive than that for absolute confinement; consequently it is instructive to look at the dimensionless forms of the confinement criteria, found by writing the equations in terms of the previously defined units for P_θ and energy, namely:

$$E < - P_\theta \tag{15b}$$

$$E < P_\theta^2/2 \tag{16b}$$

with the side condition $P_\theta < 0$ still in effect. These show, clearly, that the closed-field confinement criterion is more restrictive, since $|P_\theta| < 1$ for all particles in typical FRM systems.

For the specific case of Hill's spherical vortex, the analytic form of the effective potential, Eq. 10, allows a more detailed look at its confinement properties. As was mentioned before, the potential well is always bounded in the radial direction, and this is illustrated by Fig. 8. Here, the potential is shown as a function of r at several

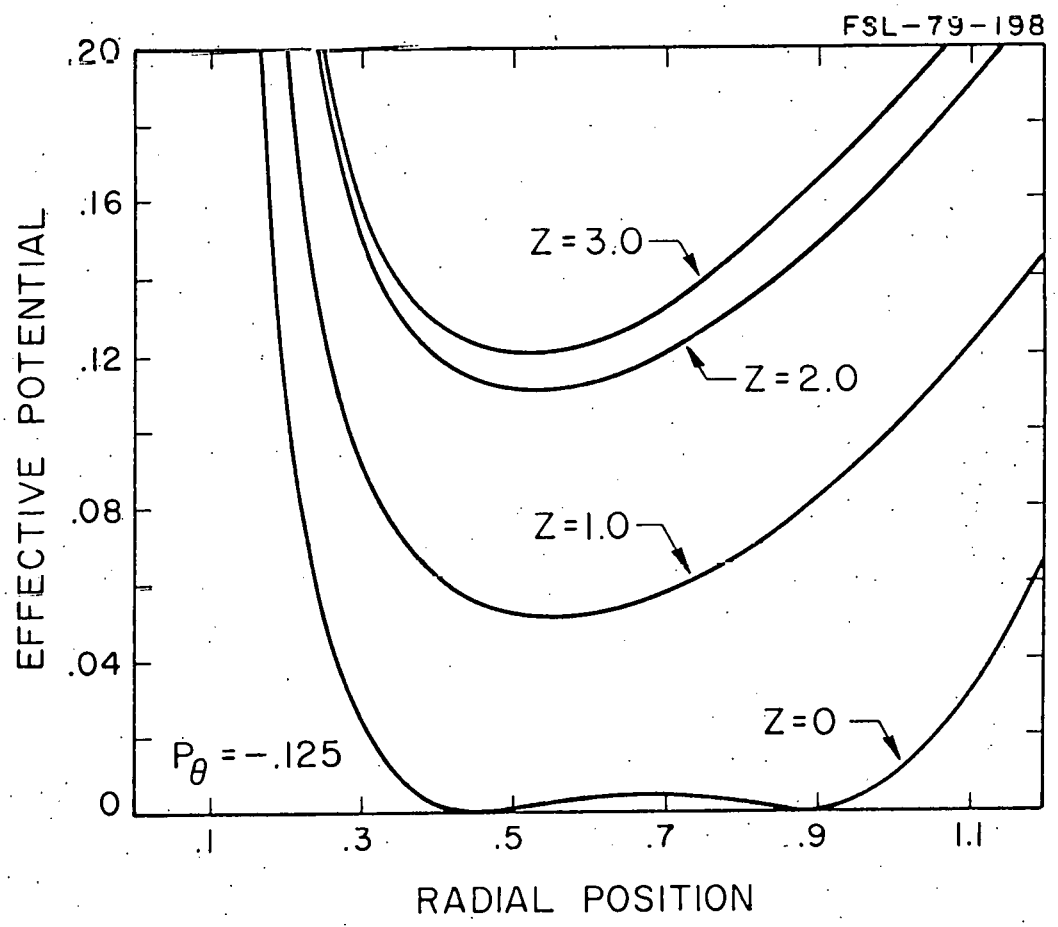

Figure 8. Radial Potential Well at Four Axial Positions for a $\kappa = 1$ Plasma. Note the central "bump" in the well at Z = 0 which confines low energy particles to flux surfaces.

axial postions for $P_\theta = -0.125$ (a representative value for the FRM). A particularly interesting aspect of this figure is the shape of the well inside the seperatrix (the z = 0 curve). This shows that particles will tend to be confined to flux surfaces in the closed field region if their energy is small compared to the central hump in the potential. Most of the background particles in the FRM fall into this category, and they can then be approximately treated by diffusion theory. However, particles with large energies no longer see the central hump, and their motion thus encompasses many flux surfaces. This large orbit type of behavior is characteristic of fps and will be discussed in more detail in the next chapter.

The critical value of the potential, which is used to determine if the particles are axially confined, was defined previously as the absolute minimum in the potential barrier. The analytic form of V, Eq. 10, then allows the asymptotic approach to this critical value of the potential to be examined as a function of z. This is done by first evaluating the radius corresponding to the local minimum, r_c, from the relation:

$$\left.\frac{\partial V}{\partial r}\right|_{r_c} = P_\theta + \frac{r_c^2}{2}\left[1-(r_c^2 + z^2/\kappa^2)^{-3/2}\right] + \frac{3r_c^4}{2}(r_c^2+z^2/\kappa^2)^{-5/2} = 0, \quad (17)$$

and then using this value together with the associated axial position to evaluate the potential from Eq. 10b. The result is shown in Fig. 9 for several values of P_θ in a spherical ($\kappa = 1$) plasma. This figure is significant because it illustrates that the critical potential has attained over 95% of its asymptotic value of $-P_\theta$, at z = 2.0. Thus, the absolute confinement criterion, Eq. 15, is valid as long as the system

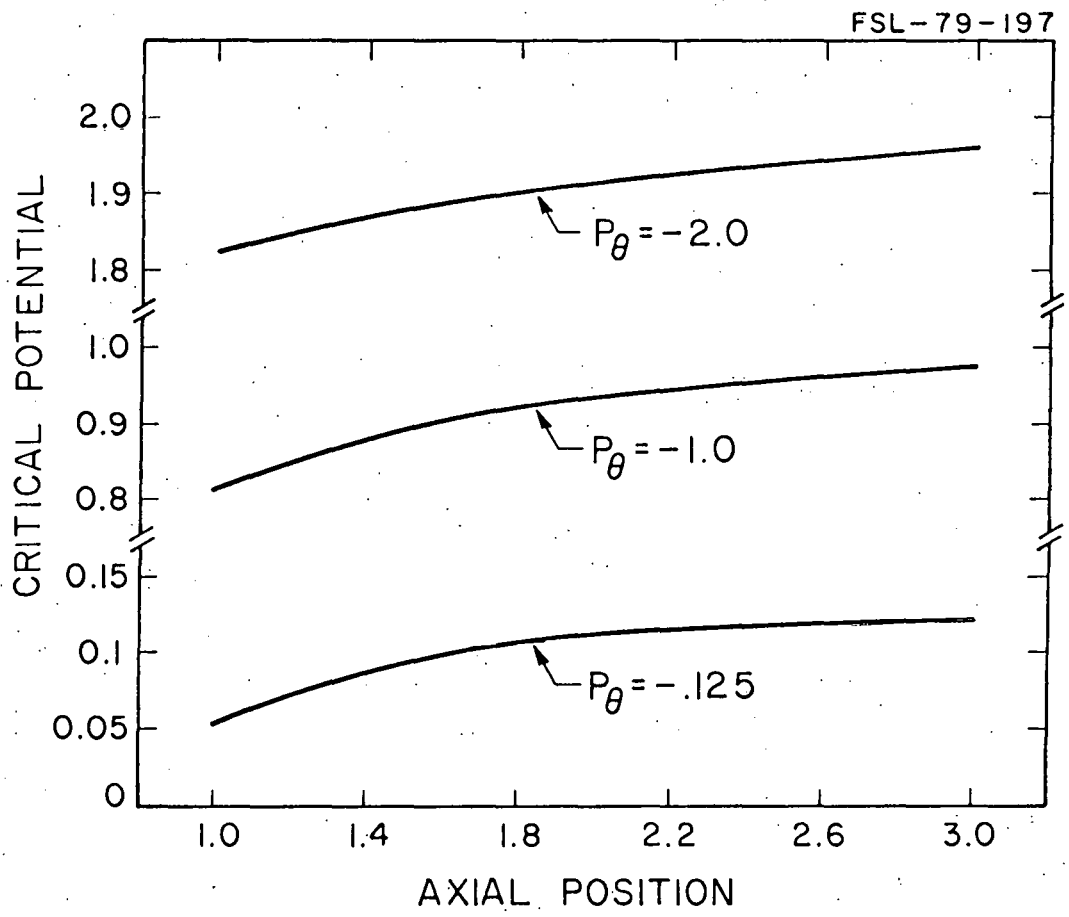

Figure 9. Minimum or "Critical" Potential as a Function of Axial Position. Note how quickly the minimum approaches its asymptotic value of $-P_\theta$.

is approximately twice the length of the plasma. In shorter systems, the critical value of the potential for absolute confinement is calculated by using Eq. 17 to evaluate r_c at the axial boundary of the system and then substituting these values back into Eq. 10b. This will give a potential that is smaller than $-P_\theta$, as shown by Fig. 9.

2.4 Energy Surfaces

A final valuable product of the analytic form of the potential is its use in evaluating the energy surfaces for typical particles in the FRM. As previously mentioned, these surfaces are determined by setting the particles energy, E, equal to the potential, V. Then, assuming the particle's P_θ is known, a locus of r,z values defining the energy surface can be calculated using Eq. 10. For low energy particles this locus is approximately a flux surface; however for higher energy particles, such as fps, it is quite different. Figs. 10-12 illustrate this by showing several energy surfaces and trajectories for a 3.5-MeV alpha particle in a typical FRM plasma. These point out dramatically the effect of P_θ on the energy surface which changes from an open-ended structure (Fig. 10) for $P_\theta = -0.02$, to a large D-shaped region (Fig. 11) for $P_\theta = -0.050$, to a smaller, elliptical region (Fig. 12) when $P_\theta = -0.22$.

These figures also illustrate the confinement theory because the dimensionless energy of this alpha is 0.022. Thus, as expected from the dimensionless form of the confinement criterion, when $E > -P_\theta$, the

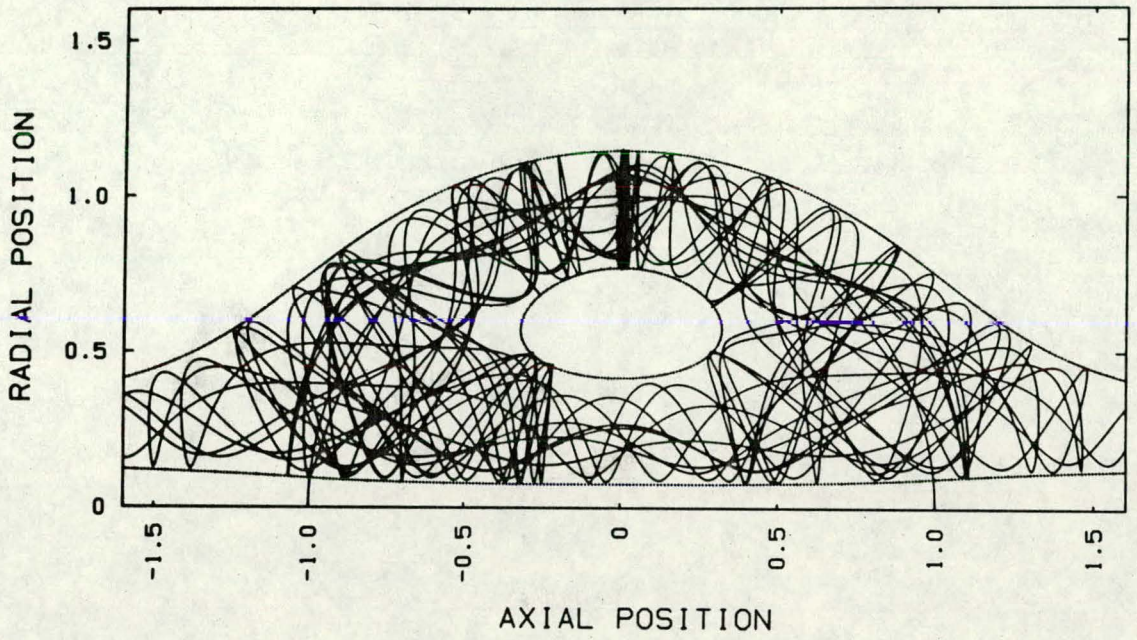

Figure 10. Energy Surface and Trajectory of an Unconfined ($E > -P_\theta$, 3.5-MeV Alpha Particle in a 21.5 cm, 60 kG FRM. This alpha's dimensionless energy is 0.022 and it has $P_\theta = -0.02$.

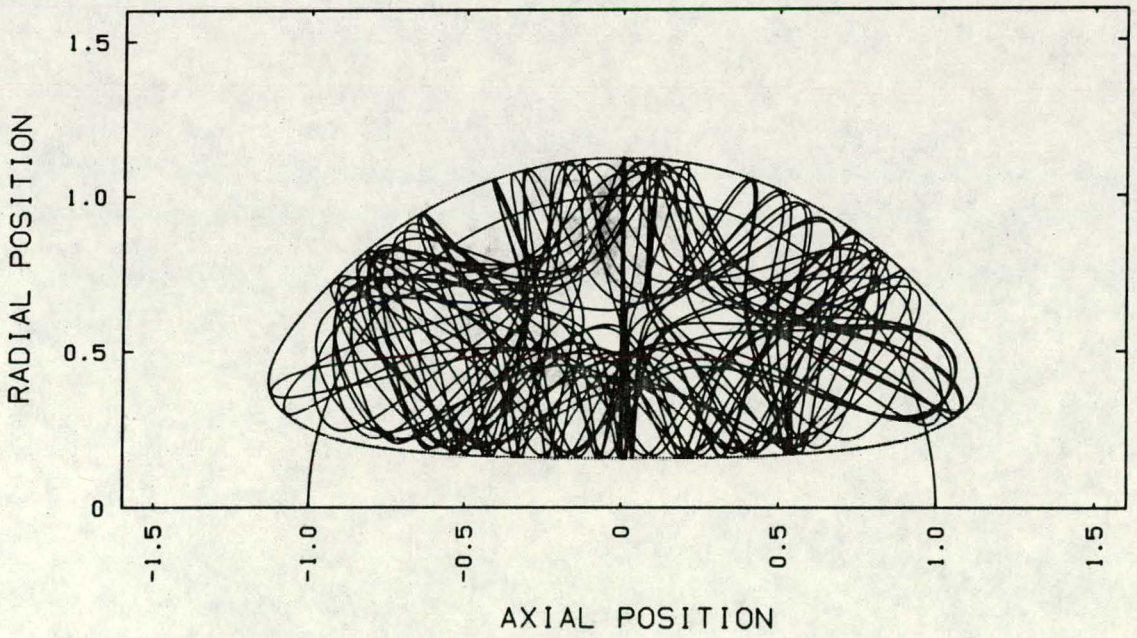

Figure 11. Energy Surface and Trajectory of a Marginally Confined ($E < -P_\theta < \sqrt{2E}$), 3.5-MeV Alpha Particle in a 21.5 cm, 60 kG FRM. This alpha's dimensionless energy is 0.022 and it has $P_\theta = -0.05$.

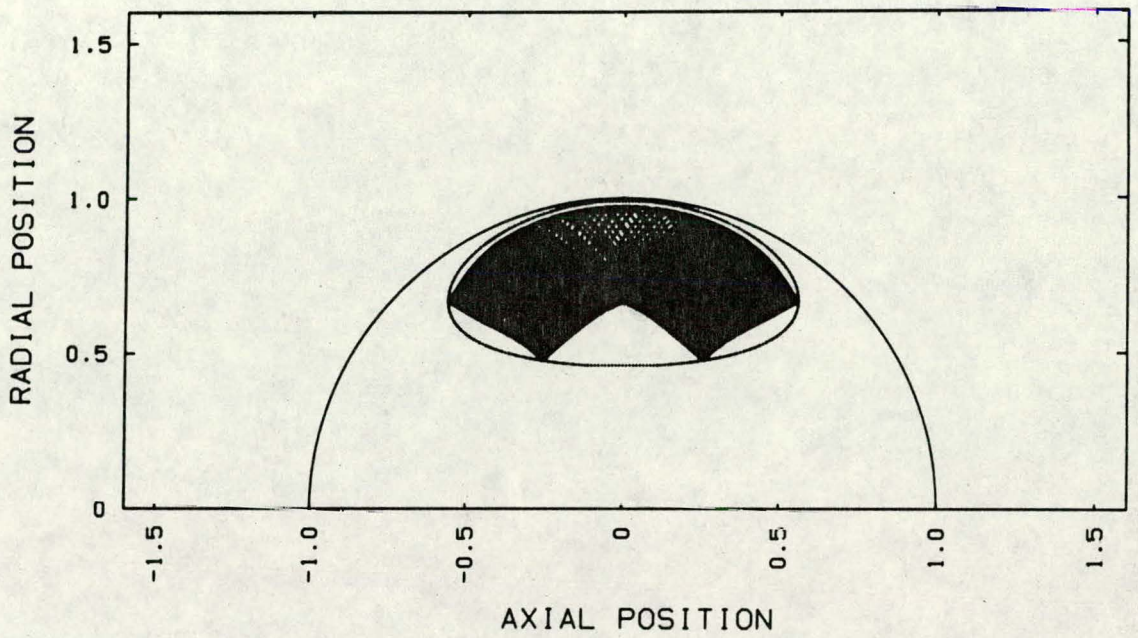

Figure 12. Energy Surface and Trajectory of a Closed-Field Confined ($\sqrt{2E} < -P_\theta$), 3.5-MeV Alpha Particle in a 21.5 cm, 60 kG FRM. This alpha's dimensionless energy is 0.022 and it has $P_\theta = -0.22$.

energy surface is open-ended and the alpha escapes. However, for the two cases where $E < -P_\theta$ the energy surfaces are closed and the alphas are confined. In addition, for Fig. 12 where $E < P_\theta^2/2$ the alpna's energy surface is completely within the closed field boundary. Therefore, coupling the effective potential with the Hill's vortex model has made it possible to determine where in configuration space an fp may reside, without solving for its detailed trajectory. This information may make it possible to evaluate fp energy deposition in the FRM without resorting to the time-consuming Monte Carlo procedure developed here, and future work will focus on this possibility.

2.5 Applications to Fusion Product Energy and Particle Deposition

The confinement theory of section 2.3 makes it possible to put absolute limits on the closed field fp energy and particle deposition. These limits are not only valuable when assessing the accuracy of the Monte Carlo calculation but are also particularly useful in identifying whether such a detailed analysis is needed. The upper limit corresponds to the optimistic assumption that all of the absolutely confined fps deposit their energy in the closed field region; while the lower limit corresponds to the pessimistic assumption that only fps which are completely confined within the closed field region deposit energy there. (FPS not absolutely confined are thought to be lost on a timescale much shorter than their slowing down time and thus to deposit virtually no energy in the plasma.) The actual fractional fp energy and particle deposition will lie somewhere between these two limiting cases and will

depend on the slowing down time in the cold, open field plasma relative to that in the hot, closed field region.

The limiting values are established by sampling a large number of particles, at successive values of the dimensionless energy variable $mc^2E/(qB_oR_{HV})^2$, chosen to represent the fusion birth distribution. The absolute and closed-field confinement criteria (Eqs. 14,15) are applied to these particles, and the number falling into each category is tabulated. The fractional confinement is then obtained by dividing by the number sampled, and the error in the fractions is thus statistically proportional to $\sqrt{1/N_c}$ where N_c is the number of particles in a particular category. Studies have shown that with ~100,000 particles, estimates of the confinement fractions are obtained which are accurate to within 1%. Therefore, this number of particles has been used to evaluate the curves presented in Fig. 13, where the absolute and closed-field confinement fractions are plotted versus the dimensionless birth energy of the fps.

These curves are extremely useful because they are completely general. That is, they specify the ablolute and closed-field confinement fractions of any charged fp in any FRM plasma. This is made possible by expressing the confinement fractions as functions of the dimensionless fp birth energy, $mc^2E/(qB_oR_{HV})^2$. The vortex radius (R_{HV}) and the vacuum magnetic field (B_o) thus characterize the plasma, in the dimensionless energy unit, while the mass, charge, and birth energy (m, q, and E_o) identify the type of fp. For example, in a 25 cm, 60 kG FRM plasma, the 3.52-MeV, D-T alphas (whose dimensionless birth energy in

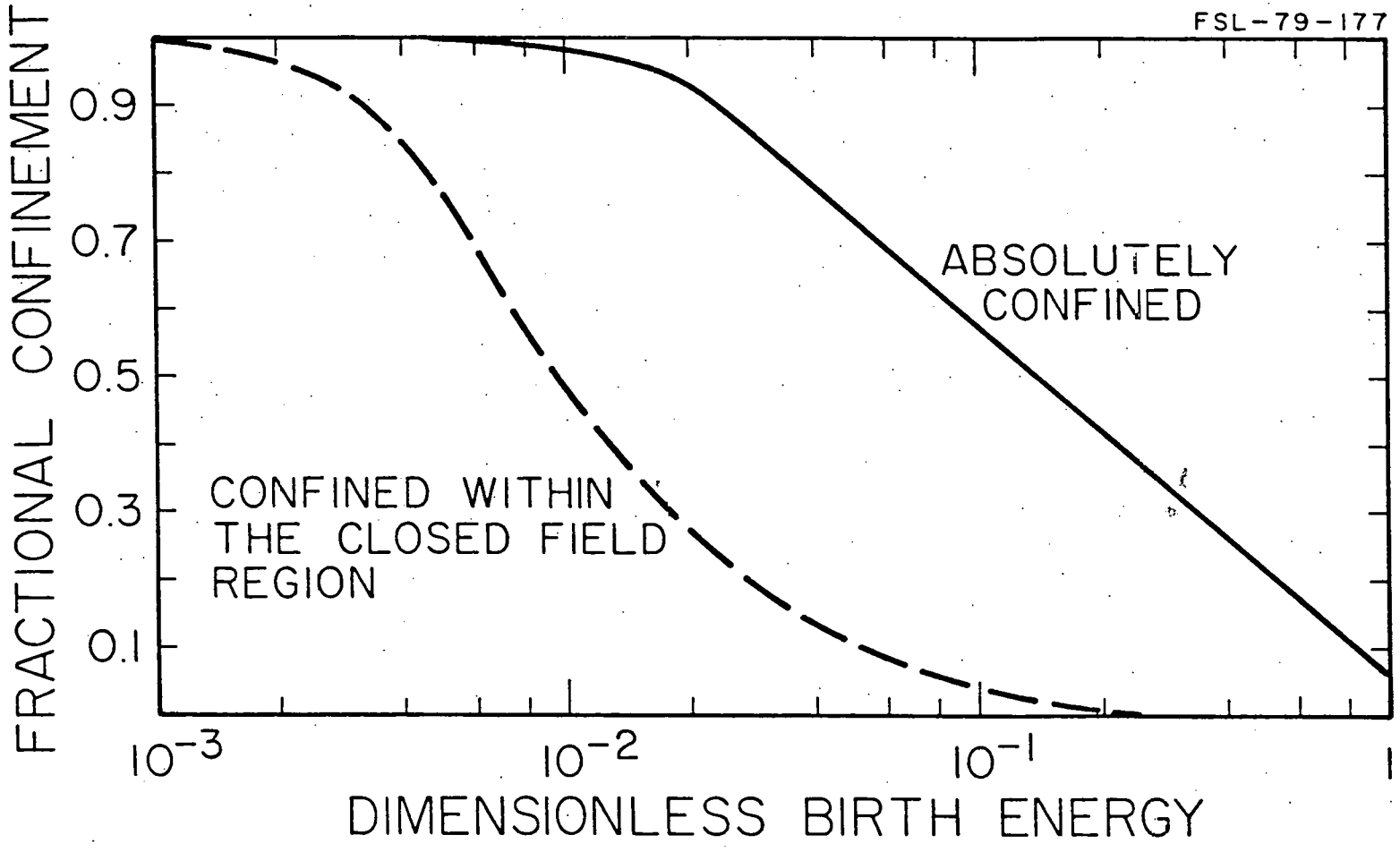

Figure 13. Confinement Limits for fps in the FRM as a Function of Their Dimensionless Birth Energy, $mc^2E_o/(qB_oR_{HV})^2$. The upper "absolutely confined" curve corresponds to the fraction of fps that have $E < -P_\theta$, while the lower curve corresponds to those that, furthermore, have $\sqrt{2E} < -P_\theta$.

this plasma is 0.016) have 95% absolute and 33% closed-field confinement fractions, while the 14.7-MeV, D-^{3}He protons (whose dimensionless birth energy is 0.068) have only 66% absolute confinement and 7% closed-field confinement. Fig. 13 thus summarizes the general limits on fp confinement in the FRM and, in addition, has allowed the results of the Monte Carlo heating studies to be represented in an extremely compact form that is discussed in Section 4.4.

The implications of the fp confinement limits shown in Fig. 13 were very exciting; especially in light of earlier, encouraging FRM reactor studies [22,23], which had assumed that there was virtually no fp heating in the FRM plasma due to its small size (radius equal only a few fp gyroradii). For the first time, the possibility of a significant heating contribution from fps had been identified due to the large fraction of them that were found to be absolutely confined. (Even for the case of the 14.7-MeV, D-^{3}He protons, over 40% absolute confinement is found in typical FRM plasmas.) The majority of these fps, however, are only marginally confined (i.e., they sample both the open and the closed field plasma); consequently an evaluation of their actual closed field energy (and associated particle) deposition requires a more detailed analysis. This was provided through the development of the Monte Carlo particle code (MCFRM) that will now be discussed.

CHAPTER 3

THE MONTE CARLO CODE - MCFRM

3.1 Introduction

As was mentioned in the previous chapter, the FRM plasma is characterised by its small size, and large field and density gradients. These properties together with the additional complexity resulting from the two distinct regions of plasma have led to the development of a detailed particle code (MCFRM) to evaluate fp behavior in the FRM. This code couples the Hill's vortex representation of the FRM equilibrium with a Monte Carlo treatment of Coulomb scattering and thus provides a complete picture of fps from birth through their thermal diffusion. The code is therefore able to calculate both energy and particle deposition in the closed field region, and consequently address the ash buildup question that accompanies the enhanced fp confinement in the FRM plasma. This is particularly important since the FRM holds the promise of true steady-state operation due to its small size, which enables the majority

of the charged fps to be "scraped off" by the cold, flowing plasma on the open field lines. The optimum design then involves a trade off between the positive contribution of fp heating, and the reduction in power density resulting from ash buildup.

The Monte Carlo solution technique also allows a large amount of additional information regarding the fps to be extracted because the time that the test particles spend in a particular region of phase space, i.e., between two energies or within a physical boundary, is proportional to the steady-state number of particles in that region. This assertion is verified by recognizing that the Monte Carlo code is solving for the Green's function of the time dependant Boltzmann equation, $G(\vec{r},\vec{v},t\ t')$, weighted by the fp source density, $S(\vec{r})$. Then, in accordance with the theory of the Green's function, the steady-state distribution of fps, $f(\vec{r},\vec{v})$, is found by taking the time integral of this result and is given by:

$$f(\vec{r},\vec{v}) = \int_{-\infty}^{\infty} S(\vec{r})\ G\ (\vec{r},\vec{v},t|t')\ dt' \quad . \tag{18a}$$

Because the source is independent of time, the primed and unprimed variables can be interchanged in the Green's function to give:

$$f(\vec{r},\vec{v}) = \int_{0}^{\tau} S(\vec{r})\ G\ (\vec{r},\vec{v},t'|0)\ dt' \quad . \tag{18b}$$

Here τ is the maximum time that any fp spends in the system (which in practice is set equal to the longest particle history in the code), and the offset t (which is now arbitrary) is set to zero.

If the above equation is integrated over phase space and split up into a discrete group structure, as is done in the code, the following expression for the steady-state number of fps in the g-th region is obtained:

$$n_g = \int_{\Delta v} d^3r \int_{\Delta v} d^3v\, f(\vec{r},\vec{v}) = \int_{\Delta v} d^3r\, S(r) \int_{\Delta v} d^3v \int_o^\tau G(\vec{r},\vec{v},t'|0)\, dt' \quad . \quad (19)$$

Then expressing the time integral as a summation and taking the group integrals inside the sum, results in the form of the group density constructed by the code, viz.

$$n_g = S_o \sum_{t=1}^{T} \Delta t \sum_{i=1}^{N} \delta_{i,g,t} \Big| N \quad . \quad (20)$$

Here S_o is the peak fusion source density, $n_o^2 \langle \sigma v \rangle$, Δt is the timestep (which is a constant in the code), T is the total number of timesteps required for the MCFRM calculation, N is the total number of test particles, and $\delta_{i,g,t}$ is defined such that:

$$\delta_{i,g,t} = \begin{cases} 1 & \text{If the i-th particle is within the g-th group boundary at time t.} \\ 0 & \text{Otherwise.} \end{cases}$$

Therefore, the steady-state group density is indeed proportional to the time that the test particles spend within that group boundary, and this fact has been used in the present study to investigate superthermal fp energy distributions, fp induced currents, and several other properties of the steady-state distribution of fps in the FRM.

Finally, section 3.6 discusses a number of test problems run using the MCFRM code. The simple nature of these cases made it possible to

develop alternate solutions using other (usually analytic) techniques, and these solutions were subsequently compared to the corresponding MCFRM calculations in order to provide a check on the code. These comparisons not only demonstrate the accuracy of the Monte Carlo method in the present application (thus providing justification for the MCFRM results in the more complicated FRM studies) but also provide a means of estimating the number of particle histories required to obtain good statistics in the actual FRM cases.

3.2 The Particle Pusher

Because typical fp trajectories encompass tremendous field gradients in the FRM plasma, a conventional guiding center approximation is not possible. Instead, the particle equations of motion must be solved in detail. Unfortunately, the two-dimensional form of the motion equations given previously, Eqs. 5-7, is not particluarly convenient for numerical integration due to the presence of a singularity along the axis ($r = 0$). This singularity is due to the centrifugical force term which must be included since the coordinate frame is non-inertal. The problem can thus be avoided (at the cost of increasing the dimensionality of the problem back to three) by instead writing the motion equations in an inertial reference frame. This form is more attractive for the present application because it leads to a particle particle push that is easier to implement. In addition, the canonical angular momentum, P_θ, is no longer completely invariant in the real problem due to the presence of Coulomb interactions. The two-dimensional form of the motion equations

is therefore only approximately valid at high energies and completely breaks down at lower energies where scattering becomes important. The formulation used in the code is then:

$$\frac{dx_i}{dt} = v_i \tag{21a}$$

$$\frac{dv_i}{dt} = \frac{q}{mc}\,(v_j B_k - v_k B_j), \tag{21b}$$

where the magnetic field components are calculated in accordance with the Hill's vortex model, Eq. 2, and electric field effects have been neglected. This latter assumption is used because fp energies are generally expected to be much larger than any plasma potentials which may develop, and fp motion should therefore be unaffected by the fields that are produced.

These equations are then integrated using a modified leapfrog algorithm [33], and thus take on the following finite difference form in the code:

$$x_i^{n+1} = x_i^{n} + v_i^{n+1/2} \tag{22a}$$

$$v_i^{n+3/2} = v_i^{n+1/2} + (v_j^{n+3/2} + v_j^{n+1/2})B_k^{n+1}/2 - (v_k^{n+3/2} + v_k^{n+1/2})B_j^{n+1}/2. \tag{22b}$$

Here the position coordinates, x_i, the velocity components, v_i, and the magnetic field components, B_i, are all dimensionless values, and time has been scaled such tnat the timestep is unity. Thus, the x's are in units of the Hill's vortex radius, R_{HV}; the v's have units of $R_{HV}N_{DT}\omega_o/2\pi$ where $2\pi/\omega_o$ is the cyclotron period of tne test particle in

the vacuum field and N_{DT} is the number of timesteps per cyclotron period; and the B's are in units of $B_o N_{DT}/2\pi$ where B_o is the vacuum magnetic field strength. This form of the motion equations is chosen because it involves fewer, and simpler, numerical operations due to the elimination of an explicit dependence on the timestep.

It should be noted here that background electric field effects have been neglected in the present study because any plasma potentials which may develop are limited to a few electron temperatures in magnitude. Consequently, the influence which the associated electric fields have on the fp motion is small due to their large energies. Future work will, however, consider electric fields in order to determine the influence which they have on fp motion at lower energies, where electric field effects could lead to slightly higher ash buildup fractions than those found here. For general completeness, then, the electric field term will need to be added to the right hand side of Eq. 22b, evaluated on integer timestep intervals, and expressed in units of $(mR_{HV}/q)(N_{DT}\omega_o/2\pi)^2$ where q and m are respectively the charge and mass of the test particles.

The algorithm draws its name from the fact that the position and velocity coordinates of the particles are a half timestep apart, as indicated by the superscripts. Thus, they are continually "leapfroging" each other in time which helps to reduce the accumulation of round off error. Additional accuracy is obtained through the use of a "time averaged" value of $\vec{v}$ in the evaluation of the $\vec{v} \times \vec{B}$ force, and the net result is a particle push that conserves energy exactly, within the

limits of machine round off. The "push" is then implemented by eliminating the $v^{n+3/2}$ terms from the right hand side of Eq. 22b and using the position coordinates x^{n+1} to calculate the magnetic field as given by the Hill's vortex model, Eq. 2. The effects of Coulomb drag and scattering are not included directly in the motion integration but are instead added in later using a separate calculation. The "scatter" is therefore applied to the velocity vector after the "push" has been completed, as is discussed in the next section.

3.3 Treatment of Coulomb Interactions

3.3.1 The Theoretical Model

A simple drag model, such as Sivukhin's [34], is adequate to determine fp energy deposition in the closed field region of the FRM; however the desire to answer questions concerning ash buildup and removal necessitate a full Coulomb scattering treatment. Spitzer [35] has developed such a model for test particles slowing down in a uniform background of Maxwellian field particles, and it is applicable to the FRM case because the elimination of the "loss cone" allows the FRM plasma to assume a Maxwellian velocity distribution. The fp thermalization process is then described by the Spitzer coefficient for drag:

$$\left\langle \frac{dv_{\parallel}}{dt} \right\rangle = - \frac{A_D}{v_f^2} \left(1 + \frac{m}{m_f}\right) G \left(\frac{v}{v_f}\right) \quad , \tag{23}$$

and the associated coefficients for velocity diffusion (VD) and pitch-angle scattering (PAS):

$$\left\langle \frac{dv_{\parallel}^2}{dt} \right\rangle = \frac{A_D}{v} G \left(\frac{v}{v_f}\right) \tag{24}$$

$$\left\langle \frac{dv_{\perp}^2}{dt} \right\rangle = \frac{A_D}{v} \left[\Phi \left(\frac{v}{v_f}\right) - G\left(\frac{v}{v_f}\right) \right] \quad . \tag{25}$$

Here $A_D = 8\pi e^4 n_f Z_f^2 Z^2 \ln\Lambda / m^2$

$v_f^2 = 2kT/m_f$

$\Phi(x) = \mathrm{erf}(x)$

$G(x) = (\Phi(x) - (2/\sqrt{\pi}) x \exp(-x^2))/2x^2$,

while n_f is the field particle density; $\ln\Lambda$ is the appropriate Coulomb logarithm for test-field particle interactions; and $v_{(f)}$, $m_{(f)}$, and $Z_{(f)}$ are the test (and field) particle velocities, masses and charges. In this model, the angle brackets are used to denote a statistical average over a large number of Coulomb interactions. Therefore, the drag term corresponds to the mean change in the magnitude of the velocity per unit time, and the VD and PAS coefficients represent the variance of the Gaussian distributed deviation about this mean in the parallel and perpendicular directions.

In the Spitzer formulation, the PAS term refers to an accumulation of small angle Coulomb scattering interactions. This should be the primary slowing down and scattering mechanism for most fps, and the present analysis should therefore lead to a good "first order" estimate of the superthermal fp slowing down distributions (cf. Section 5.4).

However, in the case of the 14.7-MeV, D-^{3}He protons, there is a significant probability of large angle, nuclear elastic scattering (NES) during slow down. This second order effect has been neglected in the present study; but, due to the influence which NES will have on the slowing down distribution of high energy fps in the FRM (and the subsequent effect which this may have on the plasma's resistance to microinstabilities), ongoing work is focusing on including NES in the MCFRM code.

3.3.2 The Background Plasma

The field particles in these equations are assumed to be described by the Hill's vortex equilibrium which gives the "self-consistent" plasma density as:

$$n(r,z) = \begin{cases} n_o r^2(1-R^2) + n_c & R \leq 1 \quad (26a) \\ n_c & R > 1 \quad . \quad (26b) \end{cases}$$

In this form, a uniform plasma temperature has been assumed due to the large ion orbits, which are thought to give rise to good cross-field conductivity in the closed field region. The ion and electron fluids are, however, treated separately; therefore the resulting description of the plasma temperature is:

$$T = \begin{cases} T_i, T_e & R \leq 1 \quad (27a) \\ T_c & R > 1 \quad . \quad (27b) \end{cases}$$

Here T_i,T_e are respectively the ion and electron temperatures in the hot, closed field region, and T_c is the temperature of the cold, flowing plasma on the open field lines. Self-consistent values for the background parameters are then chosen based on results obtained from a zero-dimensional, steady-state plasma model (described in Chapter 4) that incorporates appropriate energy and particle balances.

The fps are treated as test particles in this background plasma; therefore the effect of their energy deposition (and associated buildup as ash) on the closed field region is included via an iterative process. This process involves using the 0-D code to evaluate initial background parameters, based on a preliminary estimate of fp heating and ash buildup, and performing a MCFRM calculation to find the actual fp energy and particle deposition in this background plasma. The resulting information then serves as a new estimate of fp heating and ash buildup in the 0-D code to repeat the process, if necessary, until convergence is obtained. The computer time required for MCFRM calculations makes this iterative process quite unattractive for general parametric studies; consequently effort has recently focused on converging selected cases and using these resluts to develop a means of estimating the actual fp energy and particle deposition over a wide range of parameters. This work (summarized in section 4.4) has eliminated the need for running MCFRM in individual cases and has greatly reduced the computation time required for parametric studies.

3.3.3 The Scattering Algorithm

The scattering geometry associated with the Spitzer model is defined relative to the instantaneous velocity vector of the test particle and is shown in Fig. 14. Here the inertial reference frame of the particle pusher is denoted by the x-y-z coordinate system, and the local u-v-w coordinates are defined such that the velocity vector is aligned with the $\hat{w}$ direction. Thus, the two reference frames are related through a standard coordinate rotation, namely

$$\begin{bmatrix} \hat{x} \\ \hat{y} \\ \hat{z} \end{bmatrix} = \begin{bmatrix} \cos\alpha\cos\beta & -\sin\beta & \sin\alpha\cos\beta \\ \cos\alpha\sin\beta & \cos\beta & \sin\alpha\sin\beta \\ -\sin\alpha & 0 & \cos\alpha \end{bmatrix} \begin{bmatrix} \hat{u} \\ \hat{v} \\ \hat{w} \end{bmatrix} , \tag{28}$$

where
$$\cos\alpha = v_z/v$$
$$\sin\alpha = \sqrt{1 - (v_z/v)^2}$$
$$\cos\beta = v_x/v\sin\alpha$$
$$\sin\beta = v_y/v\sin\alpha ,$$

and v_x, v_y and v_z are the velocity components of the particle at the completion of the "push." (All possible rotations are encompassed because these velocity components are signed quantities.) The "scattered" velocity vector is then calculated by using the Spitzer coefficients for drag and VD (Eqs. 24,25) to evaluate the change in the parallel direction, Δv_w; the PAS coefficient (Eq. 26) to find the changes in the perpendicular directions, Δv_u and Δv_v; and rotating the resulting "local" vector back into the inertial frame using Eq. 28. The inertial components of this "scattered" velocity vector are thus found

FSL-79-225

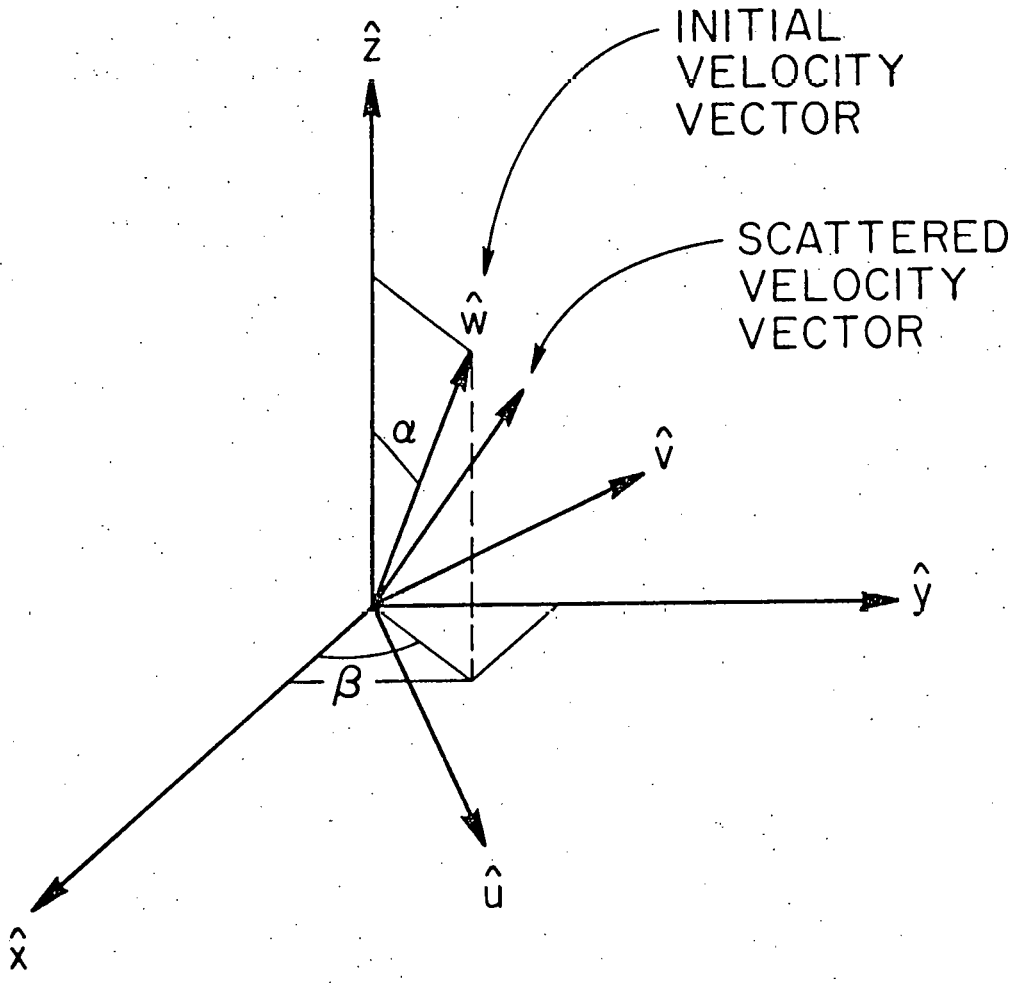

Figure 14. Scattering Geometry Used in MCFRM. The x-y-z coordinates are the fixed reference frame, while u-v-w are local coordinates, aligned such that the $\hat{w}$ direction corresponds to the initial particle velocity vector; α and β are thus the coordinate rotation angles used to translate the change in the local velocity components back into the reference frame.

to be:

$$v_{xs} = \left[\frac{\Delta v_u (v_x v_z / v) - \Delta v_v v_y}{v \sin\alpha}\right] + v_x \left[1 + \frac{\Delta v_w}{v}\right] \tag{29a}$$

$$v_{ys} = \left[\frac{\Delta v_u (v_y v_z / v) - \Delta u_v u_x}{v \sin\alpha}\right] + v_y \left[1 + \frac{\Delta v_w}{v}\right] \tag{29b}$$

$$v_{zs} = -\Delta v_u \sin\alpha + v_z \left[1 + \frac{\Delta v_w}{v}\right] , \tag{29c}$$

where Δv_u, Δv_v and Δv_w are random changes, in the local velocity frame, that describe the cumulative effect of Coulomb interactions during the timestep.

Because scattering is dominated by small angle events, these random changes are selected by sampling from triangular (as opposed to the actual Gaussian) probability distribution functions in the code. This approximation is quite reasonable, as shown in Fig. 15, if the triangular distributions are made to have the same standard deviation as their Gaussian counterparts. It is also more efficient because sampling from a triangular distribution requires the generation of only two random numbers, as opposed to the twelve that are commonly used to sample from a "Gaussian." The change in the local velocity components during a timestep is then given by:

$$\Delta v_u = \left[3 \left\langle \frac{dv_i^2}{dt} \right\rangle \Delta t\right]^{1/2} (\rho_1 - \rho_2) \tag{30a}$$

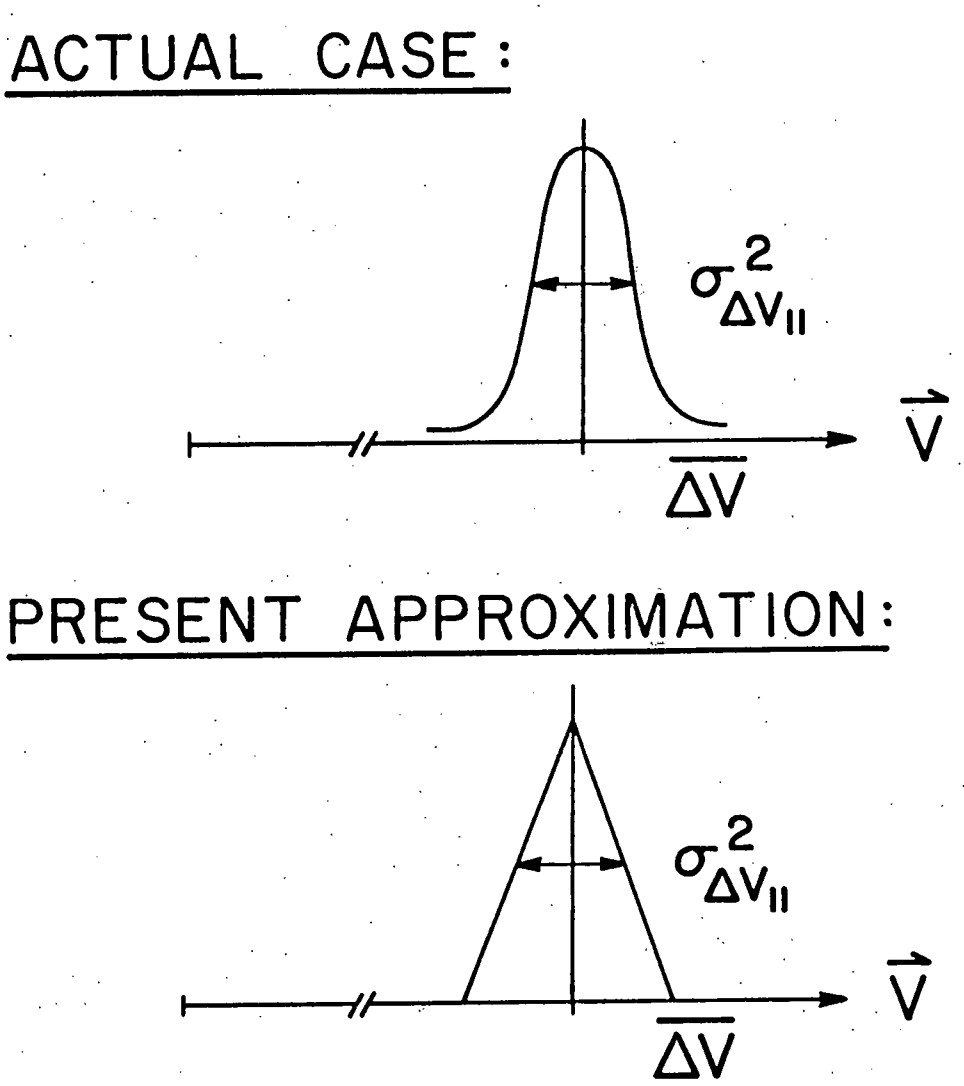

Figure 15. Illustration of the Actual Scattering Probability Distribution Compared to the Triangular Approximation Used in MCFRM. Good agreement is obtained by normalizing the triangular distribution such that it has the same standard deviation as its Gaussian counterpart.

$$\Delta v_v = \left[3\left\langle \frac{dv_\perp^2}{dt}\right\rangle \Delta t\right]^{1/2} (\rho_3-\rho_4) \tag{30b}$$

$$\Delta v_w = \left[6\left\langle \frac{dv_{\shortparallel}^2}{dt}\right\rangle \Delta t\right]^{1/2} (\rho_5-\rho_6) + \left\langle \frac{dv_{\shortparallel}}{dt}\right\rangle \Delta t \quad . \tag{30c}$$

Here ρ_1-ρ_6 are the random numbers used to construct the triangular scattering probability distributions, Δt is the timestep, and the factors of three and six are needed to correctly normalize the scattering probabilities. In this form, the statistical properties of the Monte Carlo process have been used to "decouple" the change in the perpendicular components, Δv_u and Δv_v, thus eliminating the need for evaluating trigonometric functions. This also improves the efficiency of the algorithm; however energy is now only conserved statistically, requiring that there be a large number of PAS calculations per particle history, and not exactly as it would be if Δv_u and Δv_v were not decoupled.

A final facet of the scattering algorithm arises due to the fact that characteristic fp motion requires the particle pusher to use a timestep on the order of a gyro-period, which is typically, nearly eight orders of magnitude less than fp slowing down times in the FRM. Consequently, in order to reduce the computation time to a tractable amount, the background densities are artifically enhanced by a factor of $\sim 10^5$ in the code. (This factor is not included when calculating the Coulomb logarithms, $\ln\Lambda$, and is thus a linear term in the equations.) While this seems to be a rather severe modification, it has little effect on the results for two reasons. The first is that the slowing

down time is still long compared to a timestep, which means that the Spitzer model is still valid, and the second is that fps tend to orbit in well-defined regions of configuration space (the energy surfaces discussed in Chapter 2) over long time intervals. Therefore, as long as fps are able to traverse a representative portion of this region during slow-down, the calculation should provide an accurate model of the actual situation.

3.4 Particle Initialization and Termination

Because an overall picture of the fp energy and ash despsition in the FRM is desired, a starting grid is set up which chooses particles from all regions of phase space in the most efficient way possible. This is accomplished by forcing each MCFRM particle to have the same weight, i.e., represent the same number of fps. In configuration space the fp birth distribution is proportional to $n^2\langle\sigma v\rangle d^3r$. Therefore, from the Hill's vortex description of the background plasma (Eq. 26,27) and the equal weighting requirement, a spatial grid is chosen such that:

$$\int_{R_{i-1}}^{R_i} R^2 dR \int_{\xi_{i-1}}^{\xi_i} d\xi\ R^4(1-R^2)^2(1-\xi^2)^2 = \text{const} = \left[\frac{8}{693N_R}\right]\left[\frac{16}{15N_\xi}\right] . \quad (31)$$

Here R is again the spherical radius; $\xi = z/\kappa R$; N_R is the number of radial grid divisions, R_i; and N_ξ is the number of grid divisions in the cosine of the spatial polar angle, ξ_i, at each radial increment. The spherical coordinate system has been chosen because it leads to independent integrations over the two spatial coordinates, R and ξ.

This allows separate relations governing the radial and angular grid spacing to be developed, and in simplified form they are:

$$63\ R_i^{11} - 154R_i^9 + 99R_i^7 - [8(i-1) + 4]/N_R = 0 \qquad i = 1, N_R \qquad (32a)$$

$$3\xi_i^5 - 10\xi_i^3 + 15\xi_i - [16(i-1) + 8]/N_\xi = -8 \qquad i = 1, N_\xi \quad . \qquad (32b)$$

A typical grid structure for $N_R = N_\xi = 5$ is then shown in Fig. 16 to illustrate the use of these formulas; notice that the grid points are indeed concentrated in regions where the weighting factor n^2d^3r is greatest thus representing the actual fusion birth distribution.

The fps are born isotropically in velocity space; therefore the equal weighting requirement means that each MCFRM particle must represent an equal element of solid angle. This leads to a grid chosen such that:

$$\int_{\mu_{i-1}}^{\mu_i} d\mu \int_{\phi_{i-1}}^{\phi_i} d\phi = \text{const} = \left[\frac{2}{N_\mu} \quad \frac{2\pi}{N_\phi}\right] \qquad (33)$$

Here N_μ is the number of grid divisions in the cosine of the velocity space polar angle, μ_i; and N_ϕ is the number of azimuthal starting angles, ϕ_i, at each polar increment. The above integrations over μ and ϕ can again be separated to give the following relations governing the selection of fp direction vectors at each initial spatial position:

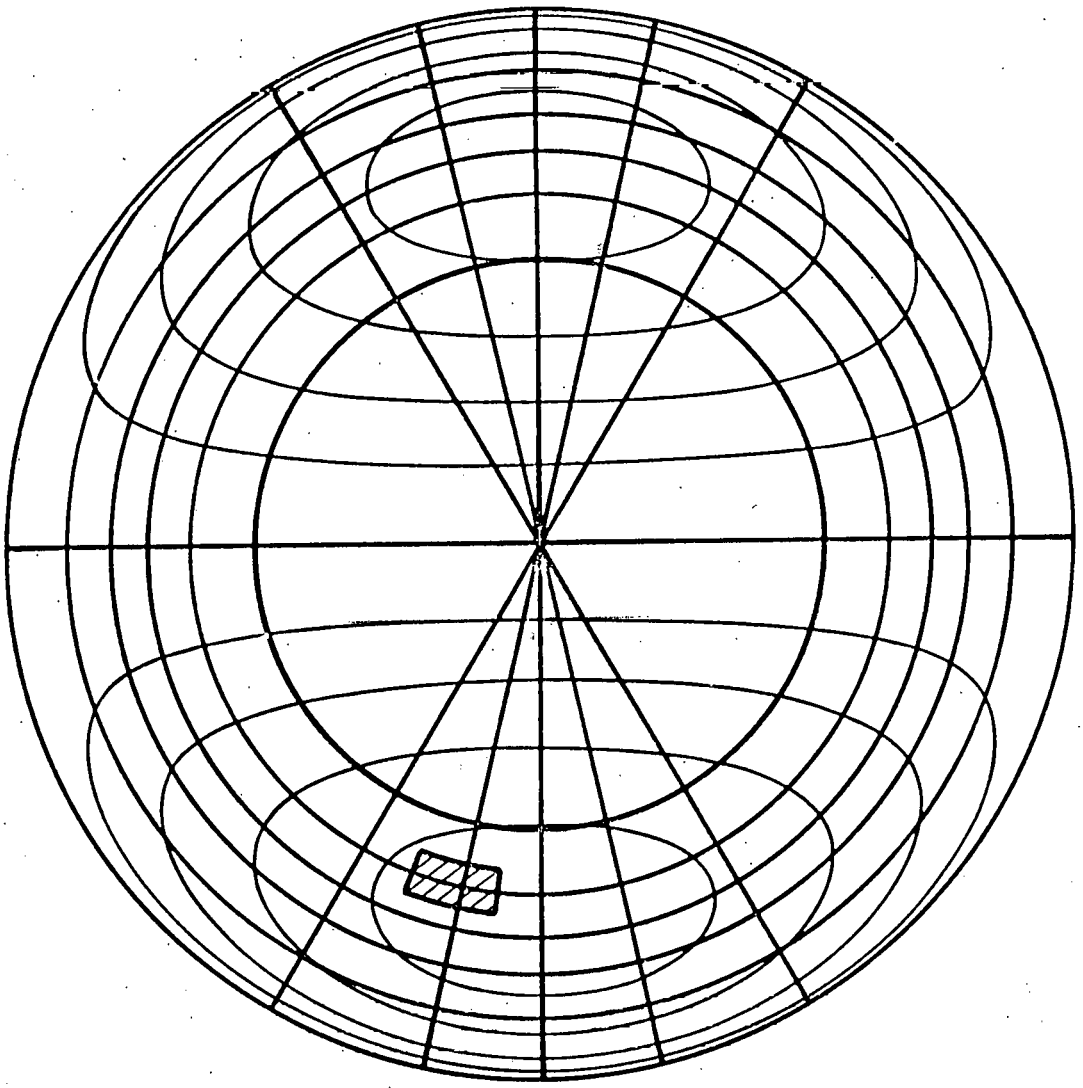

Figure 16. Initial Spatial Grid for $N_R = 5$, $N_\xi = 5$. Particles started at the grid crossing point represent all those in the volume element shown.

$$\mu_i - [2(i-1)+1]/N_\mu = -1 \qquad i = 1, N_\mu \tag{34a}$$

$$\phi_i - [2\pi(i-1)+\pi]/N_\phi = 0 \qquad i = 1, N_\phi \ . \tag{34b}$$

This initialization procedure thus ensures that all regions of phase space are represented equally, and the particle histories are then calculated in parallel. Histories are terminated when particles hit the wall, are carried out the mirror throat, or slow down to an energy less than three times the background ion temperature. Below this energy, which typically corresponds to ~300-keV, the fps are either designated as contributing to the ash buildup in the closed field region, or as a component of the open field plasma which is subsequently diverted out the mirrors.

3.5 The Ash Buildup Calculation

3.5.1 Thermalized Fusion Products

The decision to assign fps to the ash buildup fraction is made on the basis of their canonical angular momentum, P_θ, at the time they are terminated. Since their energy is known to be equal to the cutoff value, E_c, it is possible to test them using the confinement criteria, Eqs. 15,16. Then fps that are only mirror confined (i.e., have $P_\theta > -E_c$) are assigned to the open field component, and fps that are closed-field confined (i.e., have $P_\theta < -\sqrt{2E_c}$) are assigned to the ash buildup. This accounts for most of the fps (as shown in Fig. 17 for a

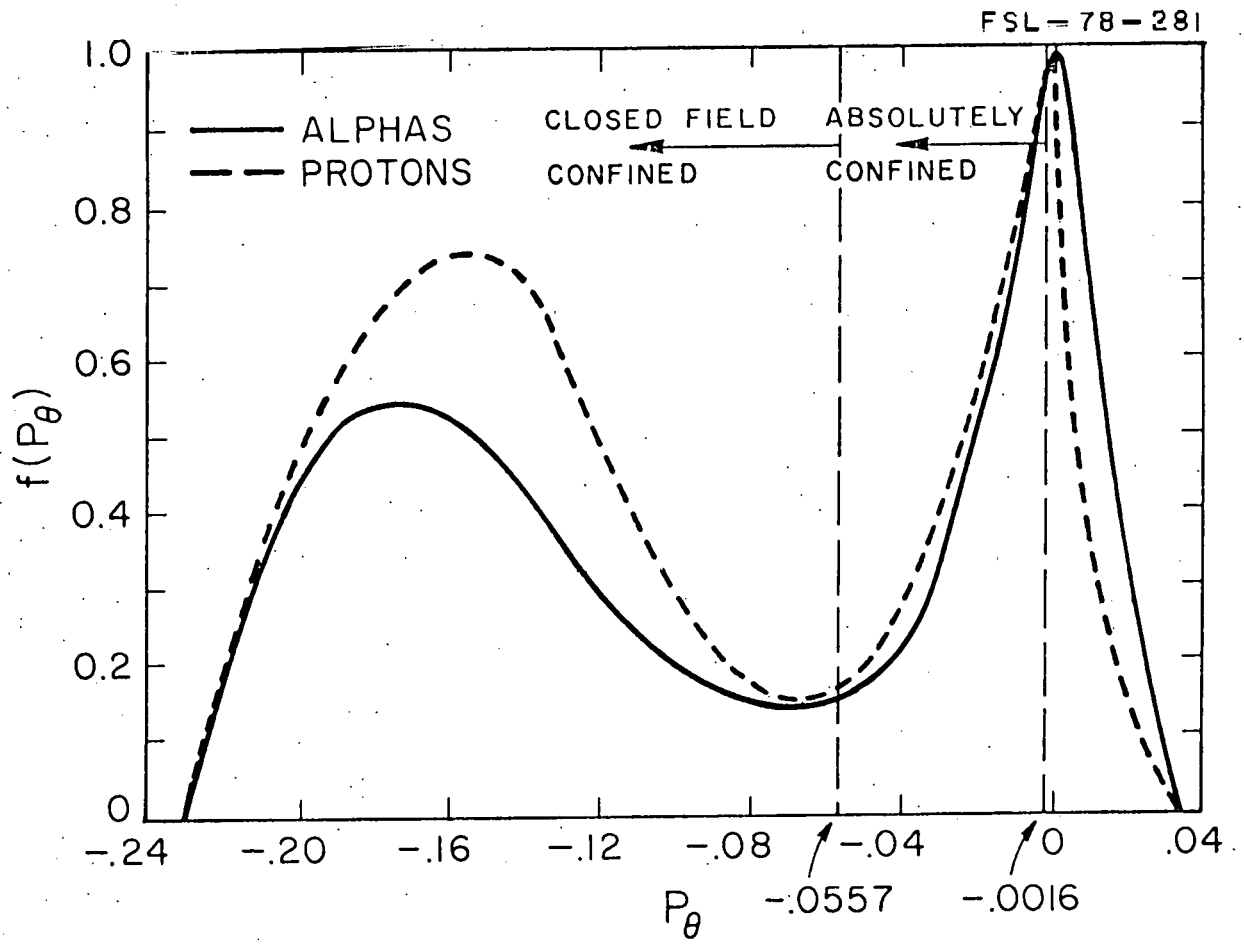

Figure 17. Distribution of Thermal ash per Unit P_θ vs. P_θ. This distribution is accumulated as the fp slow down and reach the $3T_i$ cutoff. Note the large fraction which are absolutely confined but not closed-field confined.

typical case); however a significant fraction fall between these two limiting values (i.e., have $-\sqrt{2E_c} < P_\theta < -E_c$) and are therefore contributing to the density in both the open and the closed field regions.

In order to determine whether these fps make a significant contribution to the ash buildup, it is useful to consider the energy surfaces shown in Fig. 18. They correspond to the regions of configuration space accessable to a 300-keV alpha (in a typical 23.6cm radius, 60kG vacuum field FRM plasma) having $P_\theta = -\sqrt{2E_c}$ (the limit of closed-field confinement), Fig. 18a, and $P_\theta = -E_c$ (the limit of absolute confinement), Fig. 18b. The most important feature of these figures is that fps with $-\sqrt{2E_c} < P_\theta < -E_c$ are found to be restricted from most of the closed field region and thus do very little to reduce the fusion power. (In fact, nearly 80% of the total fusion power is produced in the cross-hatched region of Fig. 18a which is off limits to fps with P_θ in the above range.) Furthermore, these fps are able to cross over the closed-field boundary and interact with the open field plasma (as shown by Fig. 18b). This causes them to be lost on a much shorter timescale than their closed-field confined counterparts which also reduces their effect on the fusion power. For these reasons fps with $-\sqrt{2E_c} < P_\theta < -E_c$ are neglected when calculating the ash buildup fraction, and, as a result, the ash buildup consists only of fps with $P_\theta < -\sqrt{2E_c}$ (i.e., those that are confined completely within the closed field region at the cutoff energy).

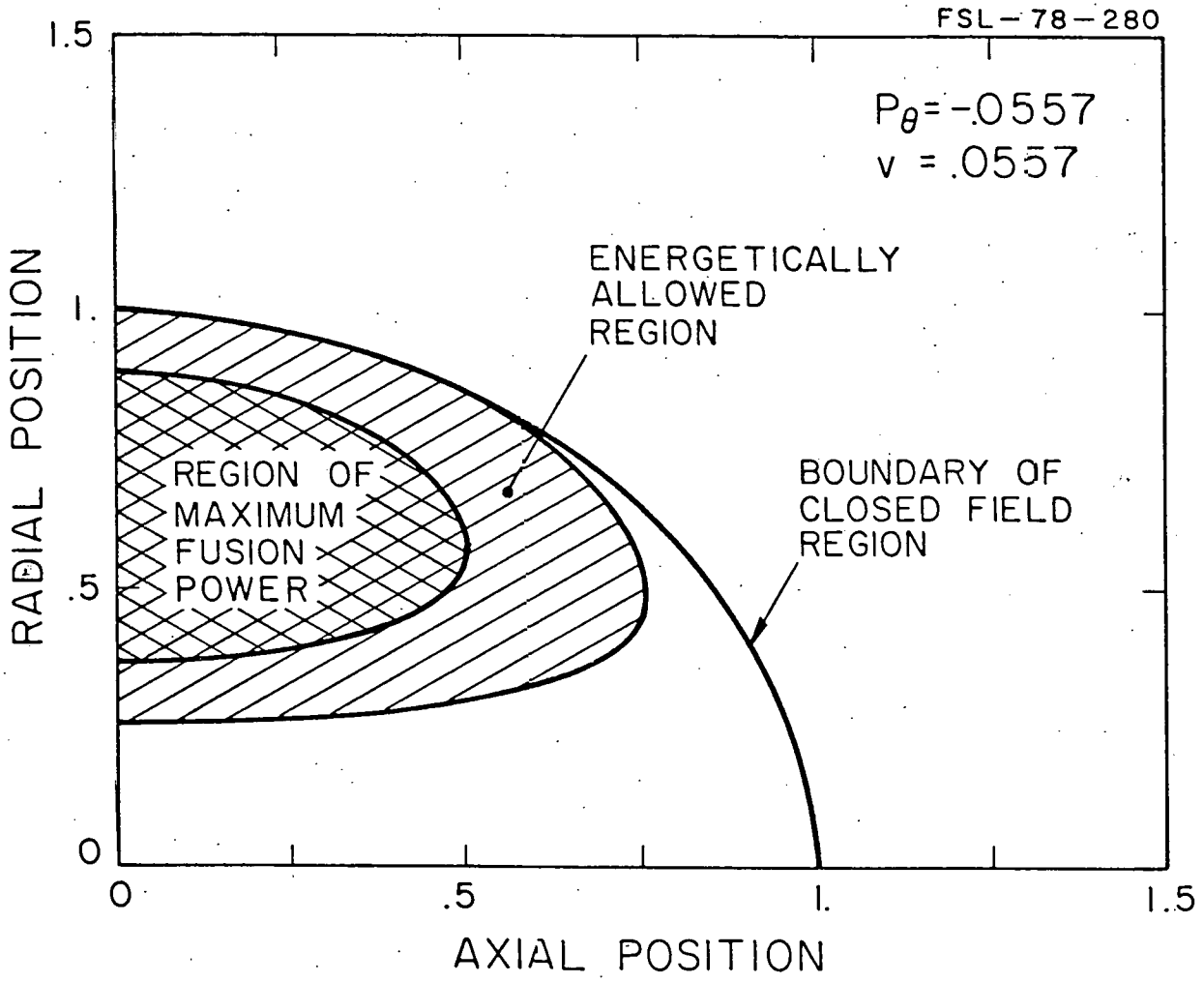

Figure 18a. Energetically Allowed Region for the Maximum P_θ Which is Closed-Field Confined. Nearly 80% of the total fusion power comes from within its inner boundary. Positions are in units of R_{HV}.

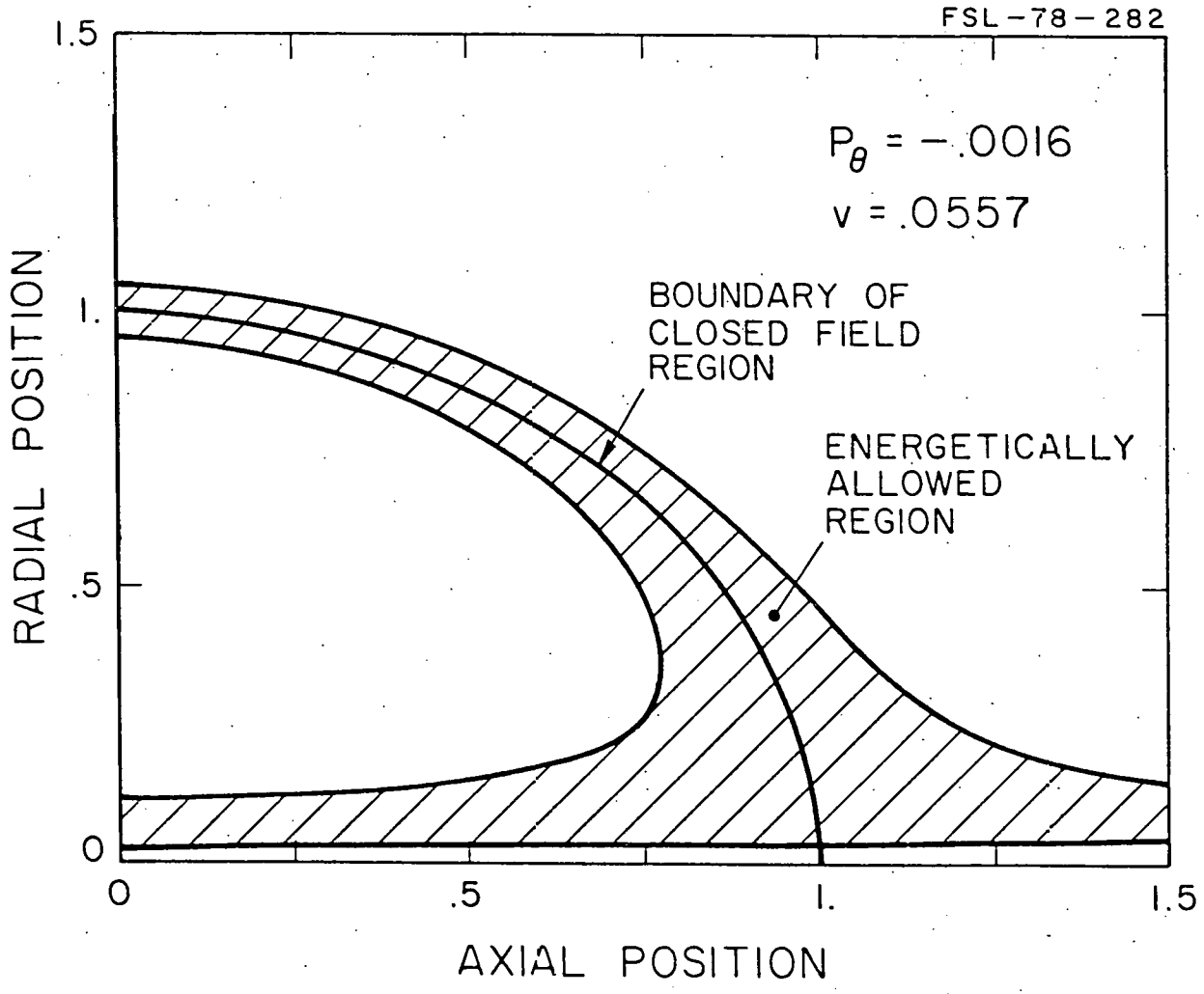

Figure 18b. Energetically Allowed Region for the Maximum P_θ Which is Absolutely Confined. Even though these fps are still confined they sample only a small portion of the closed-field region. Positions are again in units of R_{HV}.

3.5.2 Superthermal Fusion Products

The previous discussion dealt with the method of calculating the thermal ash buildup; however an additional reduction in the fusion power occurs due to the presence of superthermal fps in the closed field region. Although the steady-state density of these particles is small compared to that of the thermal ash (because the slowing down time is short compared to the confinement time), their pressure contribution may be significant due to their high energies. The effect of superthermal fps on the steady-state pressure balance is therefore included in the 0-D calculation by using MCFRM to evaluate an average slowing down time, τ_s (which is used to find the density of superthermal fps), and a representative superthermal energy, E_s, for each charged fp resulting from the common fusion reactions.

The appropriate means of calculating τ_s and E_s are determined by beginning with the actual expression for the superthermal pressure contribution, namely

$$P_{fp}(\vec{r}) = \int_{E_c}^{E_o} E\, f(\vec{r},E)dE. \tag{35a}$$

Here $f(\vec{r},E)$ is the steady-state, slowing down distribution of a given type of fps in the FRM; E_o is their birth energy; and E_c is the cutoff energy. The steady-state distribution is, however, equivalent to the time integral of the fusion source weighted Green's function (cf. Section 3.1); therefore the above equation can also be written as:

$$P_{fp}(\vec{r}) = S(\vec{r}) \int_{E_c}^{E_o} EdE \int_{o}^{\tau} G(\vec{r},E,t'/0)dt' \quad . \tag{35b}$$

Thus by interchanging the order of integration, averaging over the plasma volume, and writing the integrals in the discrete representation of the code; the superthermal pressure is finally found to be:

$$\overline{P}_{fp} = S_A \sum_{t=1}^{T} \Delta t \sum_{i=1}^{N} E_{i,t}\, \delta_{i,t}/N \quad . \tag{36}$$

In this form S_A is the volume averaged fusion source density, $\overline{n^2}\langle\sigma v\rangle$; T is the number of timesteps required to complete the Monte Carlo calculation, N is the total number of test particles, $E_{i,t}$ is the energy of the i-th particle at the t-th timestep, and $\delta_{i,t}$ is defined such that:

$$\delta_{i,t} = \begin{cases} 1 & \text{If the i-th history has } \underline{\text{not}} \text{ been terminated at the t-th timestep.} \\ 0 & \text{Otherwise.} \end{cases}$$

Consequently, the correct superthermal pressure is obtained if the average slowing down time is defined to be:

$$\tau_s = \sum_{t=1}^{T} \Delta t \sum_{i=1}^{N} \delta_{i,t}/N \quad , \tag{37}$$

and the representative superthermal energy is designated as:

$$E_s = \sum_{t=1}^{T} \Delta t \sum_{i=1}^{N} E_{i,t}\, \delta_{i,t} / N \tau_s \quad . \tag{38}$$

The total pressure from superthermal fps is then included in the 0-D code by calculating individual contributions from each type of fp based upon their respective values of τ_s, E_s, and S_A; and including each of these components in the pressure balance.

3.6 Discussion of Test Cases

As mentioned in the introduction to this chapter, the validity of the Monte Carlo model was verified by comparing its solutions for a number of simplified test problems to alternate solutions developed using other methods. This section discusses four of these comparisons that were particularly valuable in assessing the accuracy of the model. The first is for a much simplified problem which has an analytical solution. It invloves turning off the energy exchange during scattering and watching an initially monoenergetic, unidirectional burst of test particles relax towards isotropy in an infinite background plasma, where the background is composed of the same particles with a Maxwellian distribution. The analytic solution for this case was developed by Trubnikov [36] and is given in terms of the average perpendicular energy component of the test particles as a function of time. If all the test particle energy is initially in the parallel direction, the expression for their perpendicular energy component is then given by:

$$\left\langle E_{\perp} \right\rangle = \frac{2}{3} E_o \left[1-\exp(-3t/2\tau_{90^\circ})\right] \quad . \tag{39a}$$

Here τ_{90° is the 90° scattering time, which is:

$$\tau_{90^\circ} = \frac{\sqrt{m}\ kT^{3/2}}{\sqrt{2}\pi\ ne^4\ \ell n\Lambda} \left[\mathrm{erf}(1) + \frac{2}{\sqrt{\pi}}\ \exp(-1)\right]^{-1}, \tag{39b}$$

and E_o is the total energy. The comparison for this case is shown in Fig. 19, where the time dependant energy components calculated by MCFRM (for 500 deuterons in a 80-keV, 5×10^{19} cm^{-3} deuterium background) are plotted against the analytical expression. The MCFRM calculation is in excellent agreement. It not only appraoches the correct asymptotic values, of $E_{\perp} = 2E_o/3$ and $E_{\parallel} = E_o/3$, but also reproduces the correct analytical time constant τ_{90°.

The second test case involves a direct comparison with a well-tested Fokker-Planck code FOKN [37]. Since FOKN, like other available Fokker-Planck codes, cannot be applied to the full 3-D problem of interest, another simplified problem was devised. It considered the thermalization of an initial delta function source of 12,000 alpha particles, at 379-keV, in an infinite background plasma of deuterium and electrons at 80-keV. The alpha distribution function calculated by MCFRM was then compared to that found by FOKN at several times prior to thermalization, and the results from four of these comparisons are shown in Fig. 20. The instantaneous distribution function calculated by MCFRM was always in excellent agreement with that predicted by FOKN (as

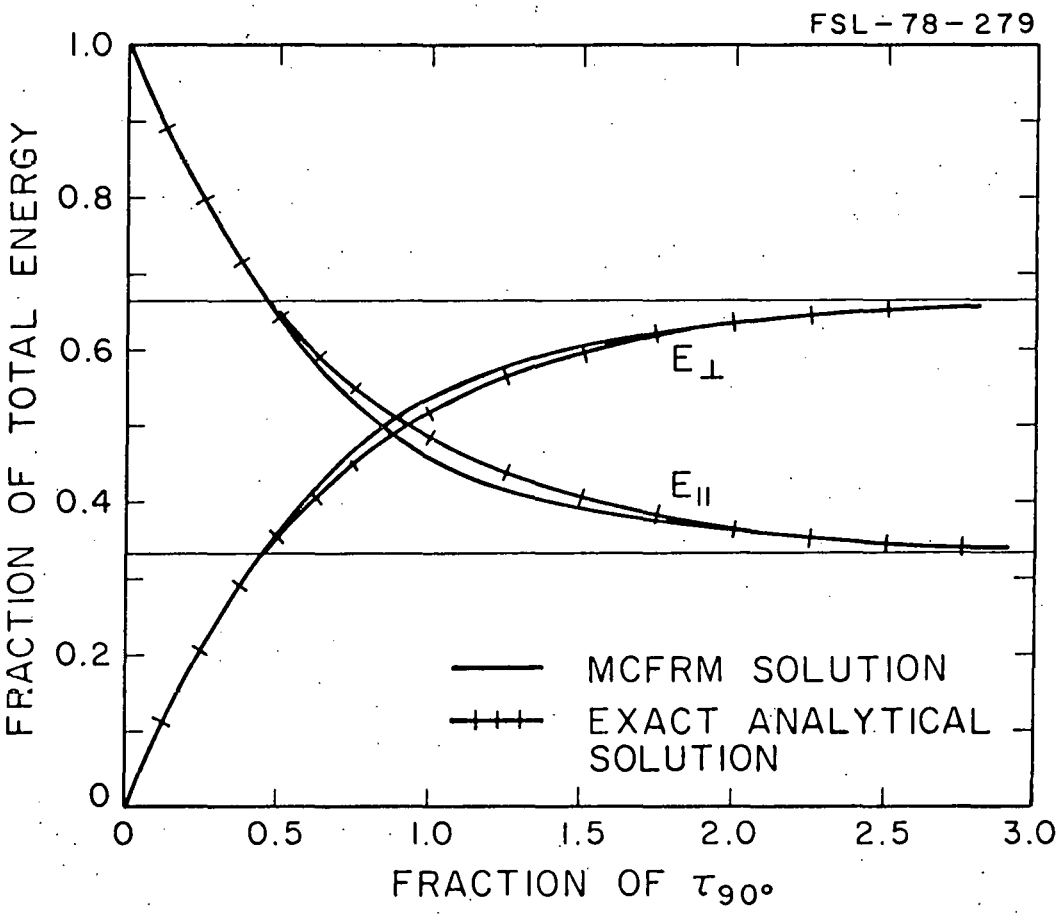

Figure 19. Comparison Between Analytical and MCFRM Solutions for the Problem of a Unidirectional Monoenergetic 80-keV Deuterium Beam Approaching an Isotropic Distribution in a Maxwellian Background of Deuterium With Average Energy = 80-keV.

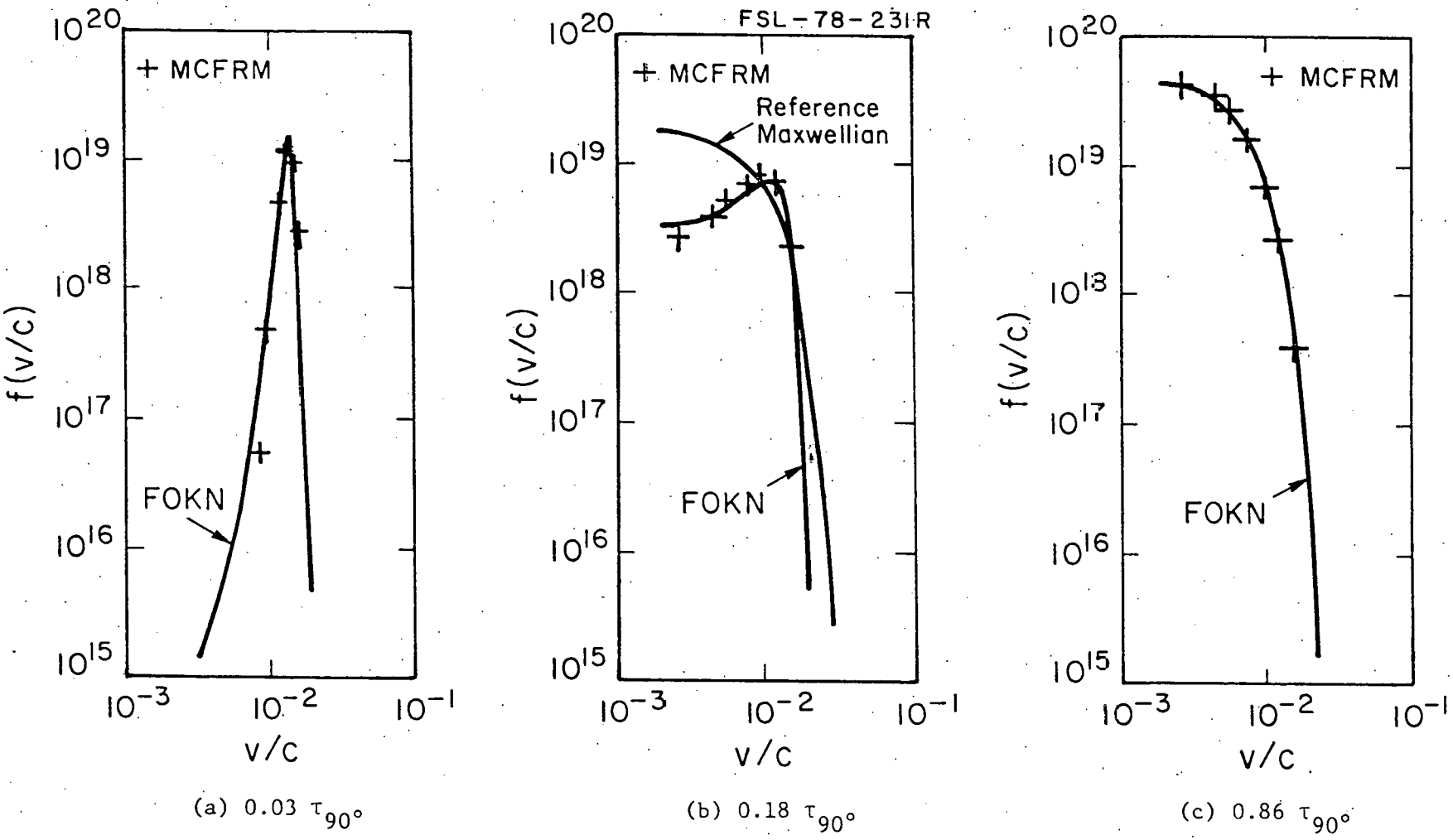

Figure 20. Instantaneous Particle Distribution Function Calculated by MCFRM (+), for a Burst of 379-keV Alphas Thermalizing in an 80-keV Deuterium Background, Compared to That Calculated by the Fokker-Planck Code FOKN, at Three Times Prior to Thermalization.

illustrated by the figure), and it also approached the correct asymptotic Maxwellian. This asymptotic behavior is particularly important since the Maxwellian distribution represents the equilibrium balance between the Spitzer drag term, which is constantly pulling particles down in energy, and the VD and PAS terms, which in turn kick particles back up in energy. The fact that the code reproduces both the transient and the asymptotic forms of the distribution function (as predicted by the Fokker-Planck calculation) indicates that the Monte Carlo scattering treatment is correct.

The third test case involves a full spatial diffusion calculation in order to study both the scattering algorithm and the particle pusher. In this problem the diffusion of an initial delta function of isotropic test particles in an infinite background plasma with a uniform magnetic field was investigated. Under these assumptions, an analytic solution describing the particle distribution in time can be developed from diffusion theory, and it is given by the following forms for one and two dimensional cases

$$\text{1-D:}\quad N(x,t) = \frac{N_o}{\sqrt{4\pi D_\perp t}} \exp\left(-\frac{x^2}{4D_\perp t}\right) \tag{40a}$$

$$\text{2-D:}\quad N(r,t) = \frac{N_o}{\sqrt{4\pi D_\perp t}} \exp\left(-\frac{r^2}{4D_\perp t}\right) \tag{40b}$$

Here N_o is the total number of test particles, and $D_\perp$ is the perpendicular diffusion coefficient. To compare with the Monte Carlo calculation, the spatial dispersion corresponding to these two distribution functions must be evaluated, and it is found to be

$$\text{1-D:} \quad \langle x^2 \rangle = 2D_\perp t \tag{41a}$$

$$\text{2-D:} \quad \langle r^2 \rangle = 4D_\perp t \tag{41b}$$

Therefore, the distributions are spreading linearly in time, with the dispersion relative to an initial plane source increasing at half the rate the dispersion relative to an initial line source increases. The MCFRM calculation argees with these results as shown in Fig. 21; however the real value of this test case comes from evaluating the perpendicular diffusion coefficient predicted by the code, and comparing it to the expected analytic diffusion coefficient. This provides a check on the entire model, including the particle push section of the code.

This check is implemented by drawing upon an analytic approximation for the diffusion coefficient developed by Longmire and Rosenbluth [38] for the case of a uniform plasma with constant magnetic field. Their expression for the diffusion coefficient, $D_{\perp A}$, is:

$$D_{\perp A} = \frac{8\sqrt{\pi}}{3} \left(\frac{m}{2kT}\right)^{1/2} \left(\frac{Zec}{B}\right)^2 n \, \ell n\Lambda \quad . \tag{42}$$

Here $m = Mm/(M+m)$ is the reduced mass for test particle, M, background ion, m, interactions; n and T are the background ion density and temperature; Z is the test particle charge; c is the speed of light; B is the magnetic field strength; and $\ln\Lambda$ is the appropriate Coulomb logarithm with the approximation being accurate to order $1/\ln\Lambda$. For the MCFRM calculation (which considered 500 protons diffusing in a background of deuterium having a density of 5×10^{14} cm^{-3} and temperature

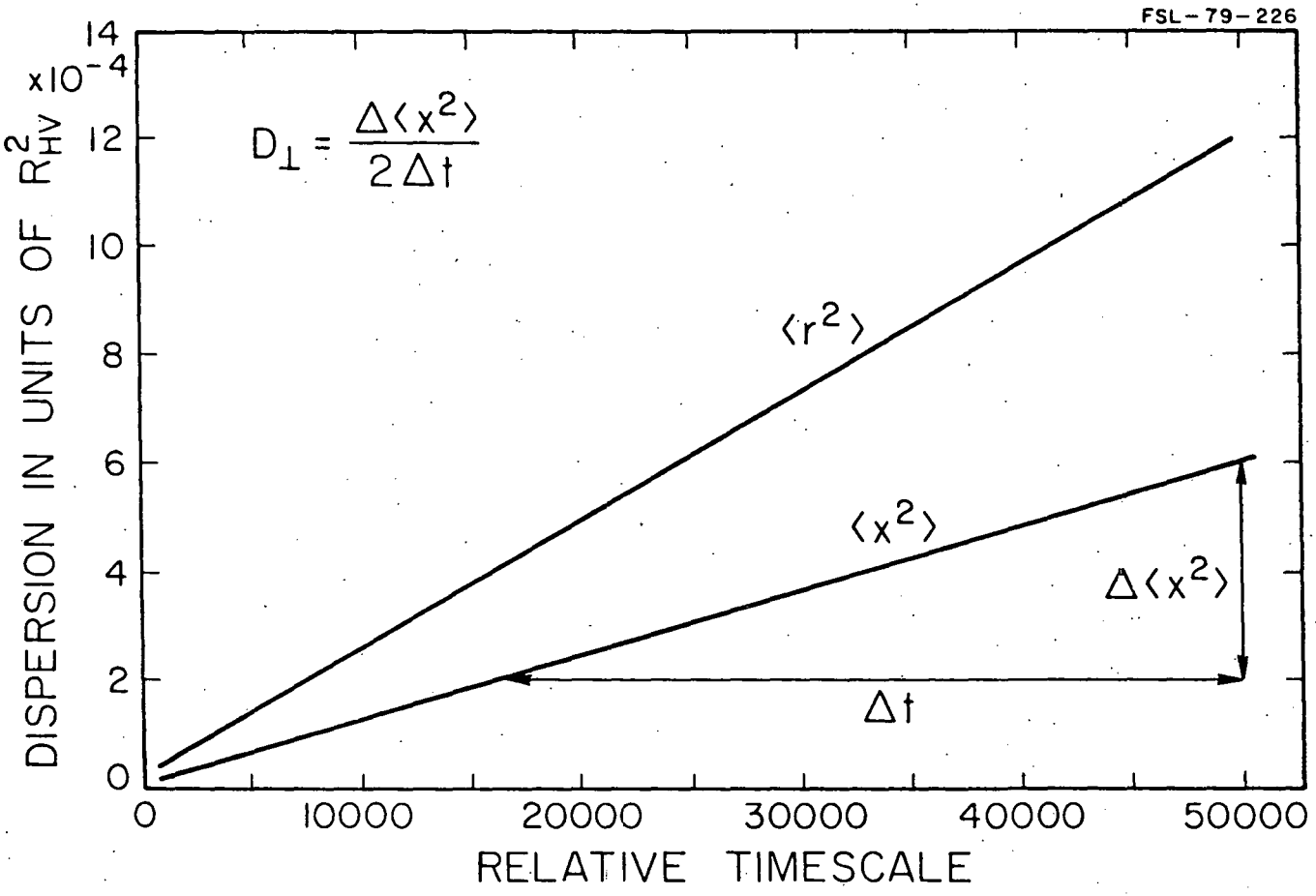

Figure 21. Spatial Dispersion of an Initial δ-Function Spreading in an Infinite, Uniform Medium.

of 100-keV, with an embedded field of 60kG) the expected value of the diffusion coefficient is 5.8×10^4 cm^2/sec. The corresponding numerical value is then found from Eq. 41 (using the slope of the curves in Fig. 21) and is equal to 6.2×10^4 cm^2/sec. This differs by ~5% from the expected value; however the analytic approximation is only valid to within $1/\ln\Lambda$ (which is also ~5% for this case); therefore the numerical value of the diffusion coefficient is found to fall within the error range of the analytic approximation. This demonstrates that the code provides an accurate model of fp behavior over the entire energy range; including the diffusive motion that occurs at lower energies due to PAS.

The final test case involves a check on the method used in MCFRM to construct steady-state fp distribution functions. This method, discussed in Section 3.1, was tested by comparing the MCFRM energy distribution to an approximate solution developed by Cordey and Houghton [39], again for the special case of an infinite plasma with uniform magnetic field, where the initial velocity of the test particles is between the thermal velocities of the ions and the electrons. This approximate distribution function is given by:

$$f(E) = C_o \frac{\sqrt{E}}{E^{3/2} + E_c^{3/2}} \qquad E_c < E \tag{43}$$

where $E_c = (M/2)(3\sqrt{\pi} m_e/4m_i)^{2/3} v_e^2$ is the "critical" test particle energy at which energy transfer rates to the background ions and electrons are equal, and C_o is an arbitrary constant. It is shown in Fig. 22, along with two MCFRM solutions, for the case of 1000, 3.52-MeV alphas in a

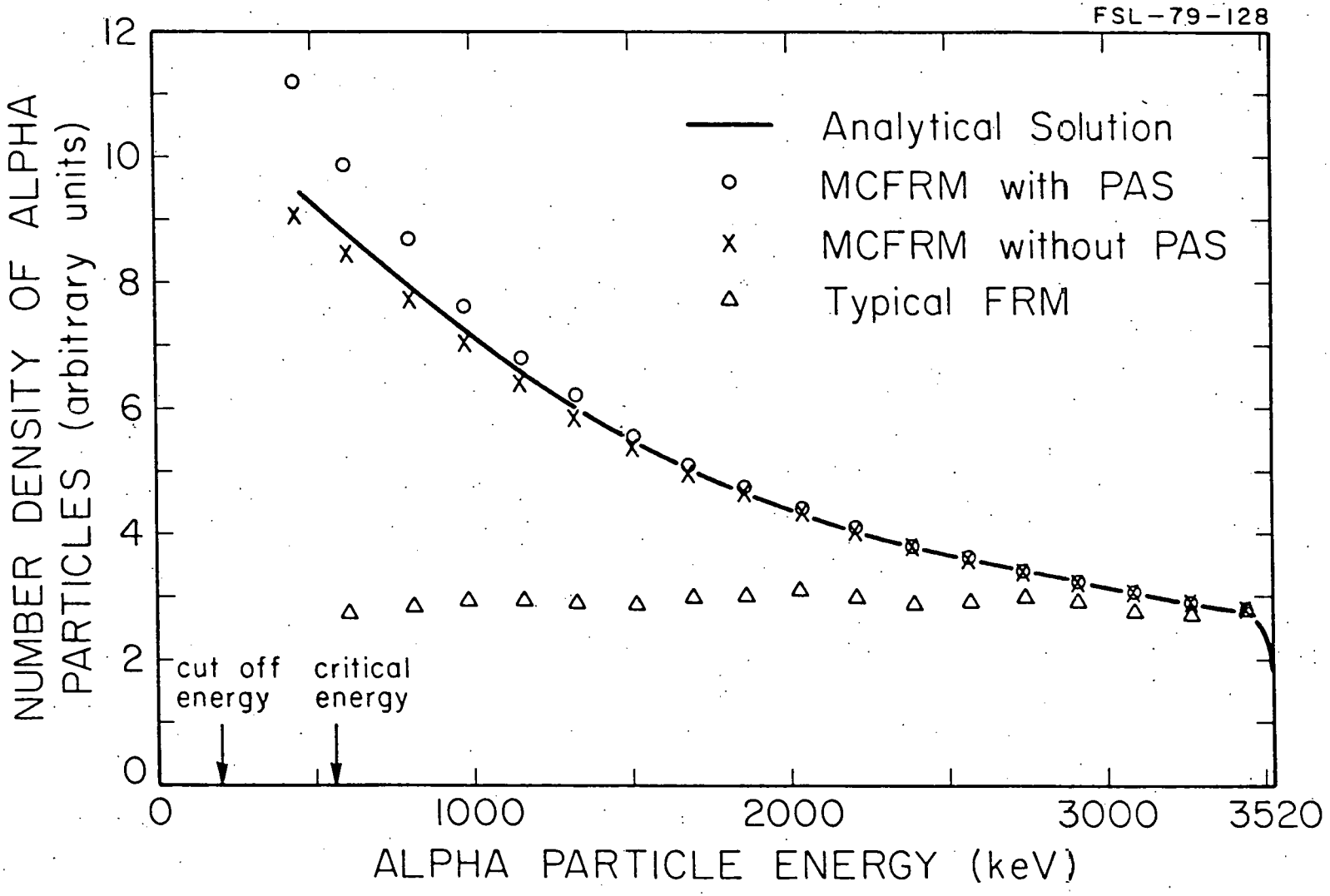

Figure 22. Comparison Between Analytic and MCFRM Distribution Functions for 3.52-MeV Alphas Thermalizing in a 10-keV Deuterium Background Plasma.

10-keV deuterium background, again with a density of 5×10^{14} cm^{-3}. All three solutions are in excellent agreement except at lower energies ($E \sim E_c$) where the analytic approximation begins to break down because it neglects VD and PAS. These effects cause a decreased $\langle dE/dt \rangle$ at lower energies due to upscatter. In a steady-state system this leads to an increase in the distribution function because particles will "pile up" instead of continuing to slow down to zero energy. Consequently, the actual distribution, MCFRM with PAS, is expected to be (and is) larger than the analytic approximation at energies near the "critical" value.

Due to the excellent comparison between the MCFRM calculation and the alternate solutions in all of the test cases, the code has been applied with confidence to the more complicated FRM cases. It has provided a wealth of information regarding the effect of fps on the steady-state FRM, and much of this information has been incorporated into the zero-dimensional model discussed in the next chapter.

CHAPTER 4

THE ZERO-DIMENSIONAL PLASMA MODEL - FRMOD

4.1 Introduction

In Chapter 1, the encouraging experimental results regarding field-reversal [10-14] together with the fact that the FRM offers a small-size alternative to conventional magnetic fusion concepts (eg. the tokamak) were cited as reasons why the FRM has recently come under intense investigation. In order to determine its potential as an advanced-fuel fusion reactor, a globally averaged point model of the steady-state FRM plasma was developed at Illinois. This model (FRMOD) is based upon the Hill's vortex description of the FRM equilibrium (Eqs. 1-3) and uses its simple analytical nature to reduce the balance equations for particles, energy, and pressure to volume averaged, zero-dimensional form. The plasma configuration is thereby "linked" to the magnetic geometry through the vortex model, and the result is thought to be an improvement over the plasma description found in other

FRM reactor studies. This fact, together with the treatment of fp heating and ash buildup that is included in FRMOD allow it to provide a self-consistant picture of the steady-state FRM plasma that is unique to it alone.

In the course of the reactor studies, many additional features were incorporated into the FRMOD code, and it is now one of the most complete FRM plasma models available. In addition to the consistant fp treatment, it also includes the following:

1. The effects of cold neutral gas (that refluxes from the wall or streams in through the beam ports) charge-exchanging and being ionized by the hot plasma, thus representing a power drain and a particle source to the closed field region.

2. Heat conduction losses to the cold, flowing plasma on the open field lines, that is introduced to reduce the cold neutral flux and to help "scrape off" the thermalized fps [40].

3. A model of neutral beam deposition that includes the effects of beam spreading from the source to the plasma and the beam shape, both of which are important in the FRM plasma due to its small size.

4. The ability to evaluate both near-term (D-T) and more advanced ($D-^3He$, Cat-D) fuel cycles.

5. A variety of diffusion laws (including an "anomalous" diffusion rate) that allow different loss rates to be investigated, since the actual loss mechanism in the FRM is not yet known.

6. An optional ion cyclotron resonance heating source, that allows refueling via low energy neutral beams or pellet injection to be considered.

This chapter explains the details of the FRMOD code in order to illustrate the physics, and some of the more crucial assumptions, that went into its development, and it is organized in the following manner. Section 4.2 discusses the major assumptions and their implications in

the code. Section 4.3 defines the terms in the balance equations and goes into their subsequent reduction to globally "averaged" form. Section 4.4 presents the means of coupling the fp heating and ash buildup, predicted by the Monte Carlo code, into the FRMOD calculations, and Section 4.5 takes a general look at the zero-dimensional form of the balance equations in order to establish some expected scaling laws for the FRM system. These scaling laws should prove to be useful when interpreting the reactor parameters presented in Chapter 5.

4.2 Physics Assumptions

As must be done in any fusion reactor study, a number of assumptions have been made concerning the scale-up of the FRM plasma parameters from current experimental values to fusion reactor conditions. This section discusses several of the physics assumptions that have been made in the present study in order to provide some justification for them, if possible, or to indicate how large an extrapolation they represent, if no direct experimental evidence exists to support them. (This latter option is usually required for the FRM case since its experimental data base is so small.) Furthermore, if there is no experimental data at all (as in the case of FRM confinement scaling), the code allows for a variety of different physics assumptions in order to, hopefully, encompass the actual case.

The first assumption regards the stability of the FRM configuration. As was mentioned in Chapter 1, FRM related experiments (eg. the FRTP)

seem to exhibit gross MHD stability (attributed to finite Larmor radius, FLR, effects), but they are eventually disrupted by an m = 2 rotational instability that sets in after a long quiescent period [12,14]. There are indications, however, that the rotation can be prevented by imposing a quadrupole barrier field on the plasma [10,11,13]. The overall reactor designs presented here thus include a quadrupole field, but the effect of this azimuthal, asymmetry is not specifically incorporated into the plasma model because it is thought to be small. To ensure that the necessary FRL stabilization is present, however, the plasma size is chosen on the basis of the stability factor S, which was earlier defined as the ratio of typical gradient lengths (i.e., $B/\vec{\nabla}B$, $n/\vec{\nabla}n$, etc.) to the background ion gyroradius (ρ_i) in the vacuum field.

In the present experiments, where gradient lengths are approximated by the plasma radius, the stability factor typically lies between five and ten; consequently these limits on S are also chosen for this study. (Some results for S = 15 are also presented to indicate how the designs might be affected should stability be observed for larger values of S.) The conventional plasma radius is not, however, a convenient means of relating the plasma size to gradient lengths in the Hill's vortex model. Therefore, a more useful relation has been developed by examining Eqs. 2,26. They show that the the magnetic field is increasing from the field null to 3/2 its vacuum value in a radial distance equal to $R_{HV}/3$, while the density is decreasing from its peak to the open field value. Thus $R_{HV}/3$ provides the same estimate of the gradient lengths, for the vortex model, that the plasma radius gives in the experiments. For all of the results presented here then, $S \equiv R_{HV}/3\rho_i$; and, to ensure FLR

stability, the plasma size, which is subsequently set equal to $3\rho_i S$, is determined by choosing a value for S that lies in the stable range. This fact, together with the quadrupole field mentioned earlier, has led to the assumption that the plasmas considered in this study are stable.

The second general assumption made in the present study involves the plasma energy and particle loss rates. Because FRM experiments give little indication as to the actual particle loss mechanism in the plasma, particle diffusion is normally assumed to be "near-classical" in the code; with the electrons being confined classically, and the ions being lost anomalously due to their large orbits. (For charge neutrality in steady-state, of course, electrons and ions are lost at the same rate.) This sets up an electric field (found by equating the steady-state electron and ion currents perpendicular to the field lines) which is equal to:

$$E_\perp = \frac{D_{\perp e} \vec{\nabla} n_e - Z D_{\perp i} \vec{\nabla} n_i}{n_e \mu_{\perp e} - Z n_i \mu_{\perp i}} \quad . \tag{44}$$

Here $n_{i(e)}$, $D_{\perp i(e)}$, and $\mu_{\perp i(e)}$ are respectively the ion (and electron) densities, classical diffusion coefficients, and mobilities; and $Z = n_e/n_i$ is the average ion charge. The cross field flux, Γ_i, can therefore be expressed in terms of an "ambipolar" diffusion coefficient, $D_{\perp A}$, and is given by:

$$\Gamma_i = n_i \mu_{\perp i} E_\perp - D_{\perp i} \vec{\nabla} n_i = - D_{\perp A} \vec{\nabla} n_i \quad , \tag{45}$$

where the above form of the electric field can be used to show that:

$$D_{\perp A} = Z \left[\frac{n_i \mu_{\perp i} D_{\perp e} - n_e \mu_{\perp e} D_{\perp i}}{Z n_i \mu_{\perp i} - n_e \mu_{\perp e}} \right] . \qquad (46)$$

This expression can be simplified by remembering that for a strong magnetic field:

$$\mu_{\perp e} D_{\perp i} \doteq - \frac{T_i}{Z T_e} \mu_{\perp i} D_{\perp e} \qquad (47a)$$

$$\mu_{\perp e} \ll \mu_{\perp i} \quad ; \qquad (47b)$$

therefore the ambipolar diffusion coefficient can finally be written in the following manner:

$$D_{\perp A} = D_{\perp e} \left(1 + \frac{T_i}{T_e}\right) . \qquad (48)$$

This corresponds to the value of the diffusion coefficient that is used to evaluate the reference case, "near-classical" loss rates in the code; with the energy confinement time presently being set equal to the particle confinement time. (The latter assumption is used because thermal conduction losses are included in a separate calculation, based upon a model that is discussed in Section 4.3.2.) The results are consequently thought to provide a more optimistic look at the FRM than may later be justified by experiment; therefore a provision is also made in the code to allow the use of more pessimistic loss estimates, in order to determine how the reactor parameters would be affected if anomalous diffusion is found.

A final general assumption is that the steady-state FRM configuration can be sustained by simply balancing the particle and energy loss rates in such a way that the plasma pressure profile is maintained. This means that the reversal current must be supplied entirely by tne plasma, itself. If the configuration is a fluid equilibrium, this is automatically true due to diamagnetic effects; however, in practice, a fluid model does not apply over the whole FRM plasma because fluid theory breaks down near the field null. Fortunately, the large ion orbits should result in a fairly continuous ion drift motion (hence reversal current) across the null region, but studies have shown [41] that the electrons will tend to cancel this ion current in a small portion of the plasma, very near the field null, where they also begin to exhibit "large orbit" motion and are thus free to drag up to the ion drift velocity. This can be prevented by introducing additional ion species into the plasma, with charges and velocities that differ from the reversal current carriers. The added drag from these "secondary" ions keeps the electrons from catching up with the ion drift velocity and cancelling the reversal current.

It is thought that fps will serve as the secondary ions in the present reactor designs; therefore a steady-state equilibrium should result, if the plasma pressure profile is maintained. Supplemental work has thus focused on identifying an effective means of refueling the plasma, without drastically disturbing the plasma pressure distribution. Indications are that this can be done either by using low energy neutral beams for refueling [42], with additional energy being supplied by ion cyclotron resonance heating (ICRH), if necessary; or by using cold

pellet injection to refuel [43] and balancing energy losses completely with ICRH. The second option is very attractive for the present application because the pellets (since they contain virtually no energy) do not affect the plasma pressure profile (which drives the reversal current). Furthermore, due to the good cross field conductivity in the FRM, the ICRH should be redistributed across the hot region with a minimal change in the temperature distributions. Thus, the combination of ICRH and cold pellet refueling should allow the FRM plasma to be sustained without disrupting the equilibrium configuration.

The zero-dimensional model, FRMOD, was developed on the basis of these general assumptions. It is, therefore, limited to considering stable FRM equilibria, with diffusive loss rates, that are maintained by neutral beam, or cold pellet, injection (supplemented by ICRH when necessary). The details of this model, and the more specific assumptions relating to its development, are discussed in the next section.

4.3 The Steady-State Balance Equations

4.3.1 Particle Balance

In the FRM, the condition for steady-state particle balance can be expressed in the following way:

$$\begin{bmatrix}\text{Injection}\\ \text{Source Rate}\end{bmatrix} + \begin{bmatrix}\text{Fusion}\\ \text{Source Rate}\end{bmatrix} + \begin{bmatrix}\text{Cold}\\ \text{Neutral}\\ \text{Source Rate}\end{bmatrix} = \begin{bmatrix}\text{Plasma}\\ \text{Leakage Rate}\end{bmatrix} + \begin{bmatrix}\text{Fusion}\\ \text{Burn-up}\\ \text{Rate}\end{bmatrix}$$

Here the injection source is in the form of either low energy neutral beams or cold pellets, the fusion source is due to thermal fp deposition in the closed field region, the cold neutrals are a result of streaming through the beam ports and cold gas reflux from the walls, the leakage is calculated in accordance with diffusion theory, and the burn-up is found from the fusion reaction rate. This type of balance must hold for each individual species in a steady-state plasma; therefore it not only specifies the required refueling rate but also allows the fusion ash concentrations to be determined. In the following discussion, then, the equilibrium density and temperature profiles in the closed field region, given previously as (Eqs. 26,27):

$$n(r,z) = n_o\, r^2(1-r^2-z^2/\kappa^2)$$

$$T = T_i,\ T_e,$$

are used to reduce these individual species balances to volume-averaged "point" form.

The first source term in the above balance, which only applies to fuel species, is written in the following manner:

$$\begin{bmatrix}\text{Average Injection}\\ \text{Source Rate}\end{bmatrix} = \frac{1}{V}\int_V d^3r\ \dot{n}_j = \frac{4}{35}\,\dot{n}_{oj} \qquad (49)$$

Here $V = (4/3)\pi\kappa R_{HV}^3$ is the plasma volume, and $\dot{n}_{oj}$ is the required refueling rate for the j-th injected ion, specified in terms of the "peak" density, n_o. For the Hill's vortex case, the average density is

therefore found to be 4/35 of the peak value. (This may seem small, but it is due to the fact that n_o does not correspond to the physical maximum in the density, which is actually equal to $n_o/4$.) The injection power is then found by evaluating the beam trapping efficiency (using the algorithm discussed in Section 4.3.4) and specifying the injection current such that the trapping rate is equal to the required refueling.

The second source term, due to the thermal fp deposition, generally applies only to ash species, but it can also represent a source of fuel (as in the case of the D-D reactions where the resulting fps include a T and a ^{3}He). It is, of course, related to the fusion reaction rate and is given by:

$$\left[\begin{array}{l}\text{Average Fusion} \\ \\ \text{Source Rate}\end{array}\right] = \frac{1}{V} \int_V d^3r \sum_k f_{RP,k}\, n_1 n_2 \langle\sigma v\rangle_k\, \delta_{jk} = \frac{4}{35}\, \dot{n}_{oj,fp}. \quad (50a)$$

In this equation, the volume averaging only affects the density terms and thus introduces a factor of 64/3465. Therefore, the form which $\dot{n}_{oj,fp}$ takes on in the code is:

$$\dot{n}_{oj,fp} = \frac{16}{99} \sum_k f_{RP,k}\, n_{o1}\, n_{o2} \langle\sigma v\rangle_k\, \delta_{jk} \quad , \quad (50b)$$

where $n_{o1} n_{02} \langle\sigma v\rangle_k$ is tne k-th fp production rate; δ_{jk} is used to represent the fact that these fps are only included if they correspond to the species being considered; and $f_{RP,k}$ represents the fraction of these fps that are deposited in the closed field region. This fraction is estimated on the basis of the Monte Carlo calculation (using the

method discussed in Section 4.4) and thus allows an accurate picture of the actual fp deposition to be obtained.

The last source term in the particle balance is written in the following manner:

$$\left[\begin{matrix}\text{Average Cold Neutral} \\ \text{Source Rate}\end{matrix}\right] = \left(\frac{n_g v_g}{4}\right)_j \frac{S_A}{V}\left(1 - \frac{\sigma_{cxj}}{2\sigma_{Tj}}\right) = \frac{4}{35}\dot{n}_{oj,cg}. \quad (51a)$$

Here $(n_g v_g/4)_j$ is the incident flux of the j-th type of cold gas particles; S_A/V is the plasma surface to volume ratio which is equal to $(3/2R_{HV})(\kappa^{-1}+\varepsilon^{-1}\sin^{-1}\varepsilon)$, where $\varepsilon = \sqrt{1-\kappa^{-2}}$; and the factor of $1-\sigma_{cxj}/2\sigma_{Tj}$, where σ_{cxj} and σ_{Tj} are the charge exchange and total ionization cross sections for these cold neutrals, is included to correct for that fraction of the cold gas interactions where no net particles are deposited because the subsequent hot neutral is lost. The incident flux of these cold particles is then specified by assuming Franck-Condon dissociation (which results in a velocity, v_g, corresponding to 3-eV) and allowing the background gas density to be chosen by the user. Hence, the form which $\dot{n}_{oj,cg}$ takes on in the code (in CGS units) is:

$$\dot{n}_{oj,cg} = \frac{7.895\times10^6}{R_{HV}}\left(\kappa^{-1} + \frac{\sin^{-1}\varepsilon}{\varepsilon}\right)\frac{n_{gj}}{\sqrt{m_j}}\left(1 - \frac{\sigma_{cxj}}{2\sigma_{Tj}}\right), \quad (51b)$$

where n_{gj} is thus the background density of the j-th type of cold neutrals, and m_j is their mass in AMU.

The first loss term, corresponding to leakage, is found by integrating the diffusion flux over the surface of the plasma and is therefore given by:

$$\begin{bmatrix}\text{Average Plasma}\\ \\ \text{Leakage Rate}\end{bmatrix} = \frac{1}{V} \int_{S_A} - D_\perp \vec{\nabla} n \cdot \vec{ds} = \frac{4}{35} \frac{n_{oj}}{\tau_p} \quad . \tag{52a}$$

In this representation, τ_p is defined to be the average particle confinement time for the plasma, and it is consequently equal to:

$$\tau_p = \frac{R_{HV}^2}{7(4+\kappa^{-2})} D_\perp^{-1} \quad . \tag{52b}$$

Furthermore, $D_\perp$ is the cross field diffusion coefficient, which is normally chosen to have the ambipolar value discussed in Section 4.2. Optional anomalous and completely classical values can also be chosen; however for all of these cases $D_\perp$ is expressed in the following general form:

$$D_\perp \alpha \rho_\beta^2 \nu_{c\beta} \tag{53}$$

Here ρ_β is the characteristic step size (normally chosen to be the gyroradius in the vacuum field), and $\nu_{c\beta}$ is the corresponding collision frequency (evaluated using the average plasma density).

The various confinement options in the code result from choosing different values for the characteristic step size and collision frequency and correspond to the following three cases:

1. Classical, where the step size is the electron gyroradius in

the vacuum field, and the collision time is that for electron-ion interactions.

2. Near-classical, where the classical diffusion coefficient is modified by the ambipolar factor $(1+T_i/T_e)$.

3. Anomalous, where the step size is the ion gyroradius in the vacuum field, and the collision time is that for ion-ion interactions.

The corresponding values for the particle confinement times are thus given by

$$\text{Classical:} \quad \tau_p = \frac{5.980\text{x}10^{10}}{(4+\kappa^{-2})} \frac{R_{HV}^2 B_o^2}{Z^2} \frac{\sqrt{T_e}}{n_{oi}} \quad . \tag{54}$$

$$\text{Near-classical:} \quad \tau_p = \frac{5.980\text{x}10^{10}}{(4+\kappa^{-2})} \frac{R_{HV}^2 B_o^2}{Z^2} \frac{\sqrt{T_e}}{n_{oi}(1+T_i/T_e)} \quad . \tag{55}$$

$$\text{Anomalous:} \quad \tau_p = \frac{1.981\text{x}10^{9}}{(4+\kappa^{-2})} \frac{R_{HV}^2 B_o^2}{Z^2} \frac{\sqrt{T_i}}{n_{oi}} \quad . \tag{56}$$

In these equations CGS units are used except for B_o which is the vacuum field strength in kG, $T_{i(e)}$ which are the ion (and electron) temperatures in keV, and m_i which is the average ion mass in AMU.

The other loss term in the particle balance, corresponding to burn-up, is evaluated by integrating the fusion reaction rate over the plasma volume and is found to be:

$$\left[\begin{array}{c}\text{Average Fusion} \\ \\ \text{Burn-up Rate}\end{array}\right] = \frac{1}{V} \int_V d^3r \sum_{\ell} n_\ell n_j \langle\sigma v\rangle_{\ell j} = \frac{4}{35} \frac{n_{oj}}{\tau_{Fj}} \quad . \tag{57}$$

Here τ_{Fj} represents the inverse of the sum of the various fusion reactivities involving the j-th species, $\langle\sigma v\rangle_{\ell j}$, and is therefore:

$$\tau_{Fj} = \frac{99}{16} \left[\sum_{\ell} n_{o\ell} \langle \sigma v \rangle_{\ell j} \right]^{-1} \quad . \tag{58}$$

The fractional burn-up, f_{Bj}, of a fuel species in the FRM can then be conveniently written, in terms of this average fusion time and the particle confinement time, as:

$$f_{Bj} = \left[1 + \tau_{Fj}/\tau_p \right]^{-1} \quad . \tag{59}$$

These individual terms are then recombined to produce the final form of the particle balance equation, which is written in terms of the "peak" density, and is consequently given by:

$$\dot{n}_{oj} + \dot{n}_{oj,fp} + \dot{n}_{oj,cg} = \frac{n_{oj}}{\tau_p} + \frac{n_{oj}}{\tau_{Fj}} \tag{60}$$

This is the form of the equation that is found in the code. It is then used either to evaluate the required refueling rate (for the case of injected particles) or to determine the steady-state ash density (for fps which are not reusable as fuel). In the latter case the injection, cold gas, and burn-up terms are all zero; thus the steady-state ash concentration is found by setting the leakage rate equal to the thermal fp deposition rate and is consequently written as:

$$n_{oj} = \dot{n}_{oj,fp} \tau_p \quad . \tag{61}$$

4.3.2 Energy Balance

Because the model treats the ion and electron fluids separately, there are two separate energy balances included in the code. The first is for the ions:

$$P_{Bi} + P_{Fi} + P_{IC} = P_{ie} + P_{Li} + P_{cx} + P_{HC} \tag{62}$$

and the second is for the electrons:

$$P_{Be} + P_{Fe} + P_{ie} = P_{Le} + P_{Br} + P_{Cy} \tag{63}$$

In these equations $P_{Bi(e)}$ and $P_{Fi(e)}$ correspond to the injection and and fusion absorbed by the ions (and electrons), $P_{Li(e)}$ corresponds to the ion (and electron) leakage powers, P_{IC} represents tne ICRH input, P_{ie} is the power exchanged between the ions and the electrons, P_{cx} represents the charge exchange losses, P_{HC} the heat conduction losses, and P_{Br} and P_{Cy} the bremsstrahlung and cyclotron radiation. In the following discussion, these power terms are expressed as volume averaged power densities, by making use of the previous results for the average value of $\overline{n} = 4n_o/35$ and $\overline{n^2} = 64n_o^2/3465$, and they are specified in terms of CGS units, whth the following exceptions: the energies and temperatures are in keV, the masses are in AMU, and the magnetic field strength is in kG.

The first two terms in these balance equations, $P_{Bi(e)}$, are evaluated by considering each injected species separately. The

individual injection sources, $\dot{n}_{oj}$, (determined from Eq. 60), and the specified injection energies, E_{oj}, allow the total trapped beam power, P_B, to be found; and it is given by the following equation:

$$P_B = 1.831\text{x}10^{-10} \sum_j \dot{n}_{oj} E_{oj} \tag{64}$$

The fraction of this power that is subsequently absorbed by the electrons is then determined by integrating over the resulting slowing down distribution:

$$P_{Be} = \sum_j \int_{E_T}^{E_{oj}} f_j(E) \left\langle \frac{dE}{dt} \right\rangle_{e,j} dE \quad . \tag{65}$$

Here $f_j(E)$ is the steady-state slowing down distribution of the j-th injected species, $\langle dE/dt \rangle_{e,j}$ is the electron drag term for this species (cf. Sivukhin [34]), and the $E_{oj(T)}$ are the corresponing beam injection (and thermal) energies. In the code this energy integral is performed by defining a group structure, such that $\langle dE/dt \rangle_{e,j}$ is constant over a group, and representing the integration as a sum. Then, by further assuming that the "peak to average" ratio is the same for superthermal particle densities as for the background plasma, the following form of the trapped beam power absorbed by the electrons is found:

$$P_{Be} = 1.831\text{x}10^{-10} \sum_j \sum_{g=1}^{G} n_{oj}^g \left\langle \frac{dE}{dt} \right\rangle_{e,j}^g \quad . \tag{66a}$$

In this equation, n_{oj}^g is the "peak" density of the j-th particles in the g-th energy group, $\langle dE/dt \rangle_{e,j}^g$ is the electron drag for the particles in this group, and G is the total number of groups.

The value of the group density, n_{oj}^{g}, is determined by recognizing that, for continuous slowing down, the total energy lost by the particles in a group can also be written as the group width, ΔE_g, times the rate at which particles are being transferred to the next lower group. Then, because the rate of transfer between groups is equal to the source rate in a steady-state situation, the group density will be:

$$n_{oj}^{g} = \frac{\Delta E_g}{\left\langle \frac{dE}{dt} \right\rangle_j^g} \dot{n}_{oj} \quad , \tag{66b}$$

where $\langle dE/dt \rangle_j^g$ is now the total drag (ion plus electron) for the j-th particles at the g-th group energy and $\dot{n}_{oj}$ is again the j-th particle source rate. The remainder of the trapped energy must necessarily go to the ions, hence:

$$P_{Bi} = P_B - P_{Be} \quad . \tag{67}$$

The next two terms considered are the fusion power inputs to the plasma P_{Fi} and P_{Fe}. They are also found by evaluating separate contributions from each k-th type (in this case charged fp) species. Therefore, the fusion power released in these particilar fps must first be found, and it is given by:

$$P_{F,k} = \int_V d^3r \left[n_1 n_2 \langle \sigma v \rangle_k + n_1 \sum_{g=1}^{G} n_2^g \langle \sigma v \rangle_{21k}^g + n_2 \sum_{g=1}^{G} n_1^g \langle \sigma v \rangle_{12}^g \right] E_k . \tag{68}$$

Here $n_1 n_2 \langle \sigma v \rangle_k$ is the k-th background reaction rate, and the

superthermal group structure for the injected ions, together with the beam-background reaction rates $\langle\sigma v\rangle_{21k}$ and $\langle\sigma v\rangle_{12k}$ has been used to include the fusion during slow down. The plasma heating will, of course, only come from the fraction of this power that is deposited in the closed field region (which is written here as $f_{RE,k}$, the fraction of retained energy), and this fraction is estimated by using the method discussed in Section 4.4 (again based upon a Monte Carlo calculation).

The specification of $P_{Fi(e)}$ is completed by splitting the resulting, retained fusion power, for each different charged fp, between the ions and electrons in the appropriate manner. This is done using a convenient formula given by Conn and Kesner [44], which describes the fraction of each fp's energy going to ions during slow-down, $f_{i,k}$, as:

$$f_{i,k} = \frac{1}{3}\frac{E_c}{E_o}\left\{ \ell n \left[\frac{E_c - \sqrt{E_c E_o}+E_o}{E_c + 2\sqrt{E_c E_o}+E_o}\right] + 2\sqrt{3}\ \tan^{-1}\left[\frac{2\sqrt{E_o}-\sqrt{E_c}}{\sqrt{3E_o}} + \frac{\pi}{\sqrt{3}}\right]\right\} . \quad (69a)$$

In this equation E_o is the fp birth energy, and E_c is the critical energy, where the ion drag is equal to the electron drag, which is given by:

$$E_c = 14.8\ m_k\ T_e \left[\frac{\sum_j n_j\ Z_j^2/m_j}{n_e}\right]^{2/3} . \quad (69b)$$

Here $m_{j(k)}$ are the masses of the background ions (and fps), $n_{j(e)}$ are the background ion (and electron) densities, Z_j is the background ion charge, and T_e is the electron temperature. Since the remainder of each

fp's energy $(1-f_{i,k})$ goes to the ions, both $P_{Fi(e),k}$ have been specified and are found by multiplying the k-th charged fp production rate by the fraction of its retained energy that is given to the ions (or electrons). The final form of the expressions for the total fp heating, $P_{Fi(e)}$, is determined by summing the individual contributions over all charged fps giving:

$$P_{Fi} = 2.959\text{x}10^{-11} \sum_{k} \dot{n}_{ok} f_{i,k} f_{RE,k} E_{k} \quad , \tag{70a}$$

where (for electrons) the $f_{i,k}$ factor is replaced by $(1-f_{i,k})$, and the $\dot{n}_{ok}$ term represents the total "peak" production rate for the k-th charged fps, namely

$$\dot{n}_{ok} = n_{o1} n_{o2} \langle\sigma v\rangle_{k} + n_{o1} \sum_{g=1}^{G} n_{o2}^{g} \langle\sigma v\rangle_{21k}^{g} + n_{o2} \sum_{g=1}^{G} n_{o1}^{g} \langle\sigma v\rangle_{12k}^{g} \quad . \tag{70b}$$

The last two related terms are the plasma leakage powers P_{Li} and P_{Le}. For the ions, this power loss is defined in the following manner:

$$P_{Li} = 4.578\text{x}10^{-10} \sum_{j} \left(\frac{n_{oj}}{\tau_{p}} + \frac{3}{5} f_{Lj} \frac{n_{oj}}{\tau_{Fj}} \right) T_{i} \quad . \tag{71a}$$

In this equation, n_{oj}/τ_{p} represents the diffusive losses, where each particle transports $3kT_{i}/2$ out of the system and requires an additional kT_{i} to diffuse through; and $(3/5)f_{Lj} n_{oj}/\tau_{Fj}$ represents the fusion burn-up losses (which are not diffusive and thus remove only $3kT_{i}/2$).

The loss factor f_{Lj} is then defined as:

$$f_{Lj} = 1 - \left[\frac{\sum_i n_i n_j \langle\sigma v\rangle_{ij} \sum_k f_{RE,k}/2}{\sum_i n_i n_j \langle\sigma v\rangle} \right] \tag{71b}$$

Here the $f_{RE,k}$ are again the fraction of the k-th fp's energy (resulting from the $\langle\sigma v\rangle_{ij}$ reaction) that is retained in the plasma, and f_{Lj} therefore accounts for the portion of the "fused" background energy that is carried out of the system by unconfined fps.

The electron leakage is similarly defined to be:

$$P_{Le} = 4.578\text{x}10^{-10} \left[\frac{n_{oe}}{\tau_p} + \dot{n}_{oe} \right] T_e \tag{72a}$$

In this case, n_{oe}/τ_p again accounts for the diffusive losses (where n_{oe} is the "peak" electron density), but the second term, $\dot{n}_{oe}$, now represents the effect of fusion burn-up on the electron energy balance. It is equal to the number of electrons that must be lost to compensate for the charge associated with escaping superthermal fps and is therefore given by:

$$\dot{n}_{oe} = \frac{16}{99} \sum_k (1-f_{RP,k}) Z_k n_{o1} n_{o2} \langle\sigma v\rangle_{12k} , \tag{72b}$$

where $f_{RP,k}$ was defined earlier as the fraction of the k-th charged fps that are not lost, and Z_k is their charge. Finally, since both of these losses are diffusive in nature, the electrons each carry off $5kT_e/2$.

The remaining terms in the electron energy balance are straightforward. The first is the energy exchange term, P_{ie}, which is calculated in accordance with the standard formula for Maxwellian distributions (averaged using the appropriate density weighting):

$$P_{ie} = 8.952\text{x}10^{-23} \frac{n_{oe}}{T_e^{3/2}} \sum_j \frac{n_{oj} z_j^2}{m_j} (T_i - T_e) \quad . \tag{73}$$

The others are the radiation terms. The bremsstrahlung losses, P_{Br}, are found using the standard expression (also appropriately averaged), namely

$$P_{Br} = 9.884\text{x}10^{-26} n_{oe} \sum_j n_{oj} z_j^2 T_e^{1/2} \quad . \tag{74}$$

However, the cyclotron losses, P_{Cy}, are modified slightly (to account for the high β of the FRM) by introducing a $(1-\beta)/\beta$ factor, as suggested by Miley [45]. This factor is included in the average over the plasma volume by recognizing that $(1-\beta)$ represents the magnetic pressure in the plasma (given by the square of the Hill's vortex field strength, Eq. 2), and that β represents the plasma pressure (which is also specified for the Hill's vortex case). The appropriate averaging factor for the cyclotron emission is thus found from:

$$\frac{1}{V} \int_V d^3r \left(\frac{1-\beta}{\beta}\right) n^2 = \frac{16}{3465} n_o^2 \quad , \tag{75}$$

and the final expression for the cyclotron radiation losses is:

$$P_{Cy} = 1.154\text{x}10^{-27}\ \kappa_c\ d\ n_{oe}^2\ T_e^2 \quad . \tag{76}$$

Here $d=(1+n_iT_i/n_eT_e)(1+T_e/204)$ and K_c is the plasma reabsorption coefficient which is calculated in accordance with the Krajeck formula [46] assuming cylindrical geometry.

The remaining terms involve the ion power balance, and two of them are also straightforward. The first, P_{IC}, is the ICRH input which is set equal to the amount of power that is required to satisfy the ion energy balance. This can be done because ICRH replaces the ion temperature in the dependent variable set, when it is used; and, as a result, the ion temperature then becomes an independent value specified by the user, with the required ICRH input being calculated by the code. The details of ICRH coupling into the plasma do not enter into the ion power balance but are, instead, included via an estimate of ICRH efficiency that is also specified by the user. The second simple term is the estimate of charge-exchange losses, P_{cx}, which corresponds to hot charge-exchange neutrals which are not reionized in the plasma. The power they carry out is thus equal to the average rate at which they leave the plasma, (discussed when considering the cold neutral source rate) multiplied by their average energy, $3kT_i/2$. Therefore, this power loss is represented by the following expression in the code:

$$P_{cx} = \frac{2.168\text{x}10^{-3}}{R_{HV}} \left(\kappa^{-1} + \frac{\sin^{-1}\varepsilon}{\varepsilon}\right) \sum_j \frac{n_{gj}}{\sqrt{m_j}} \frac{\sigma_{cxj}}{2\sigma_{Tj}}\ T_i \quad . \tag{77}$$

The final term in the ion power balance is P_{HC}, which represents the heat conduction losses. It is evaluated by using the boundary layer model that is shown in Fig. 23, where a uniform temperature profile is assumed; except for a thin layer (that is taken to be one hot ion gyroradius thick) where the density becomes uniform and the temperature profile takes on the shape of the Hill's vortex pressure distribution. This model is chosen because the large ion orbits should lead to good thermal conductivity in the closed field region (and consequently a uniform plasma temperature); however there needs to be some sort of "transition" to the open field plasma parameters. The width of this transition region is thought to be equal to the width of the energy surface for those hot ions that are "just confined" (i.e., have $P_\theta \sim E$, cf. Fig. 18b).

This distance is nearly equal to the "gyro-diameter" of the hot ions in the magnetic field at the boundary (Eq. 80a); consequently the hot ion gyroradius in the "average" field of Eq. 80a is used to approximate the "step size" for energy diffusion, ρ_E. Futhermore, the geometric average of the closed-field density near the seperatrix (found from the Hill's vortex density profile Eq. 26a) and the open-field density (i.e., $\sqrt{n_B n_c}$), together with an assumed boundary temperature, are used to calculate the collision frequency for heat transfer through the boundary layer, ν_E. (The open-field density enters the problem because heat must conduct across the seperatrix to the open field region before it is lost along the field lines.)

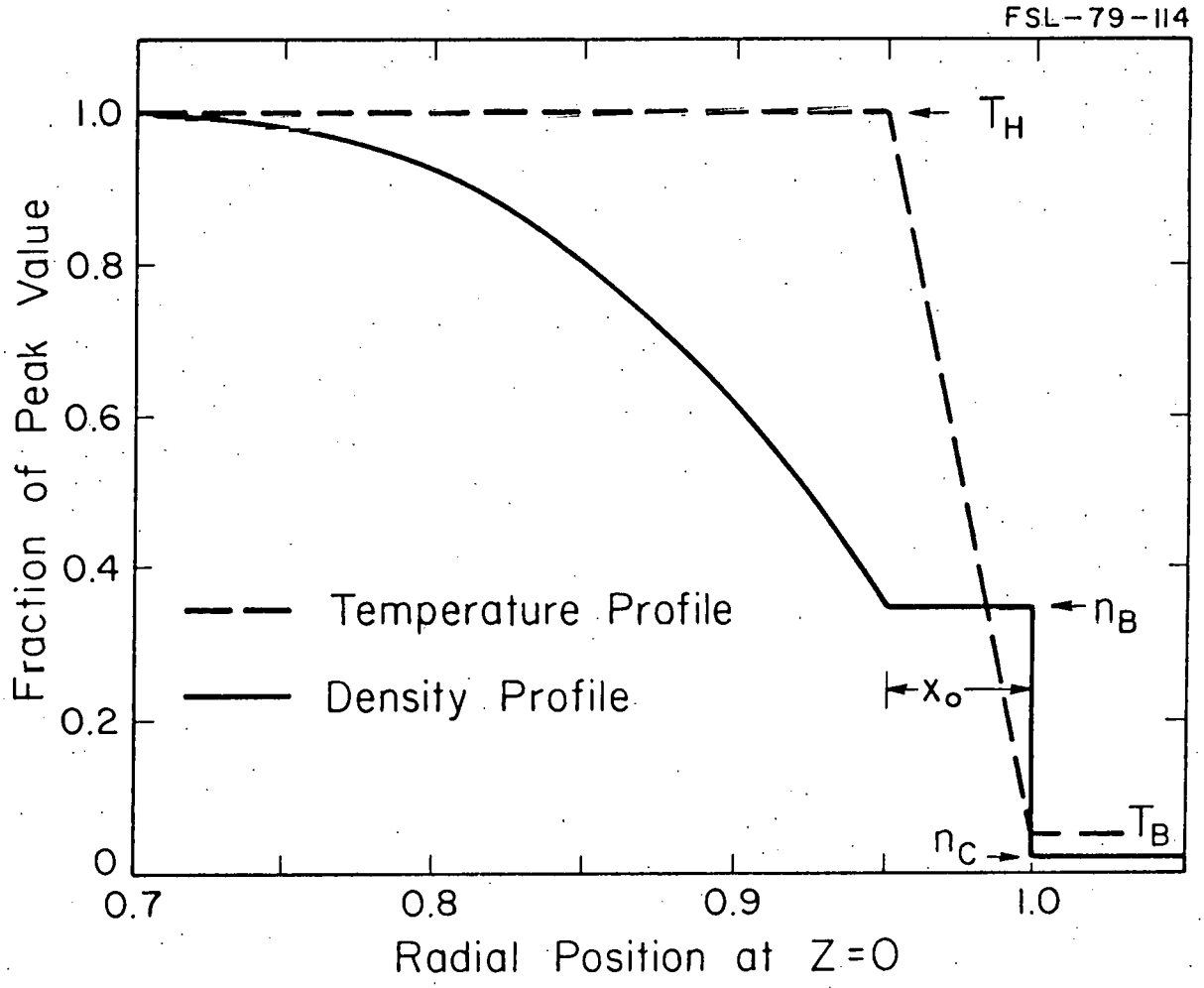

Figure 23. Illustration of the Boundary Layer Model Used to Calculate the Heat Conduction Losses in the FRMOD Code. The distance x_o is equal to the hot ion gyroradius in the vacuum field, n_B is the plasma density on the "hot" side of the boundary layer, and n_C is the cold, open field density.

The total heat conduction losses are thus given by:

$$Q = \int_{S_A} -k_\perp \vec{\nabla}T \cdot \vec{ds} = \frac{16\ k_\perp\ R_{HV}\ \kappa(4+\kappa^{-2})}{15\ x_o(2-5x_o+4x_o^2)}\ T_i \quad . \tag{78}$$

In this equation, x_o is the thickness of the boundary layer (in units of the vortex radius, R_{HV}); T_i is the ion temperature in the hot region, and $k_\perp \alpha \rho_E^2 \nu_E$ is the cross field thermal conductivity:

$$k_\perp = 6.310 \times 10^{-10} \frac{\sqrt{m_i}\ n_B\ n_c\ Z^2}{B^2\ \sqrt{T_B}} \quad . \tag{79}$$

Thus n_B, T_B, and B are the density, temperature, and magnetic field strengtn in the boundary layer; n_c is the density of the cold, open field plasma; and m_i and Z are the average ion mass and charge.

In the spirit of the zero-dimensional nature of the model, $k_\perp$ is evaluated for "average" properties of the boundary layer, which are taken to be those in the region of the steepest temperature gradient (where most of the conduction losses occur). For the Hill's vortex pressure profile, this corresponds to the region near (r = 1, z = 0); therefore the "average" properties are found to be:

$$B^2 = \frac{3}{2} B_o^2 \left[1-4x_o + \frac{26}{3} x_o^2\right] \tag{80a}$$

$$n_B = n_o\ x_o\ [2-5x_o + 4x_o^2] \quad , \tag{80b}$$

with T_B left to be chosen by the user, since the results are fairly

sensitive to its value. The conduction loss estimate is then completed by substituting these "average" boundary layer properties into the expression for the thermal conductivity and converting the losses to a volume averaged form. This results in the following expression (used in the code) for the heat conduction losses, namely:

$$P_{HC} = \frac{5.392\times10^{-19}}{(1-4x_o+\frac{26}{3}x_o^2)} \frac{(4+\kappa^{-2})}{R_{HV}^2 B_o^2} \sqrt{m_i}\ n_{oi}\ n_c\ Z^2\ \frac{T_i}{\sqrt{T_B}} \tag{81}$$

4.3.3 Tne Remaining Balance Equations

The final three balance equations used in the code, are those for pressure, charge, and background composition. The pressure balance condition is satisfied by choosing the "peak" densities, n_{oj}, for each species and energy group, such that the sum of the individual pressure contributions is equal to the total "peak" pressure, P_o, which is given by:

$$P_o = \frac{9B_o^2}{32\pi}(4+\kappa^{-2}) \quad . \tag{82}$$

In the code, the pressure balance then takes on the following form:

$$5.588\times10^{13}(4+\kappa^{-2})\ B_o^2 = n_{oe}T_e + \sum_j (n_{oj}T_i + \sum_{g=1}^{G} n_{oj}^g\ E_j^g) \quad . \tag{83}$$

Similarly, the charge balance requirement is written as:

$$n_{oe} = \sum_j Z_j \left[n_{oj} + \sum_{g=1}^{G} n_{oj}^g \right] \quad , \tag{84}$$

and the balance on the background ion composition, which simply states that the sum of all of the fractional ion densities in the code be equal to the total ion density, i.e.,

$$n_{oi} = \sum_{j} (n_{oj} + \sum_{g=1}^{G} n_{oj}^{g}) \quad . \tag{85}$$

This completes the equations necessary to specify the steady-state plasma parameters. They represent a system of five non-linear algebraic equations, which are solved by choosing values for the stability factor, S; the elongation factor, κ; the magnetic field strength, B_o; the various injection energies, E_{oj}; the open field density, n_c; the boundary layer temperature, T_B; and fuel species density ratios. The remaining plasma parameters are then calculated in the code by using a standard non-linear algebraic equation solver (QNWT) from the MSL subroutine library, which solves the equations by reducing the balance equation residuals to small values. The "solution" criterion is normally chosen to be when the square root of the sum of the squares of these residuals is less than 10^{-4}.

4.3.4 Neutral Beam Deposition

Because of the small size of the FRM plasma, the effects of beam spreading and the actual shape of the beam source are important in evaluating the beam trapping efficiency in the FRM. Therefore, a detailed calculation of the beam trapping efficiency is included in

FRMOD. This calculation begins by assuming that the beam has the following shape when it reaches the plasma:

$$J_o(y,z) = \frac{I_s}{\pi D^2 \tan\theta_y \tan\theta_z} \exp\left[-\left(\frac{y}{D\tan\theta_y}\right)^2 - \left(\frac{z}{D\tan\theta_z}\right)^2\right]. \quad (86)$$

Here I_s is the total beam current (particle/sec), D is the distance from the source to the plasma, $\theta_{y(z)}$ are the beam divergence angles in the y (and z) directions, and the coordinate system is defined such that the beam is travelling in the positive x direction. Once the beam contacts the plasma surface it begins to be attenuated, and the beam current at any distance along the beam path x inside the plasma is therefore given by:

$$J(x,y,z) = J_o(y,z) \exp\left[-\langle\sigma\rangle_T \int_{-x_s}^{x} dx' \, n(x',y,z)\right] . \quad (87)$$

In this equation, $\langle\sigma\rangle_T$ is the total beam ionization cross section, $n(x,y,z)$ is the background density, and x_s is the value of x (which is a function of y and z for the present case) where the beam first makes contact with the plasma. The corresponding geometry is shown in Fig. 24, for the beam coming in at angle β relative to the reference coordinate frame which defines the plasma parameters.

The beam trapping efficiencies, for individual species, are then calculated by dividing the plane perpendicular to the beam direction (the y-z plane in this case) up into small unit areas, $\Delta y \Delta z$, and summing the transmitted beam for each area element over a rectangular region

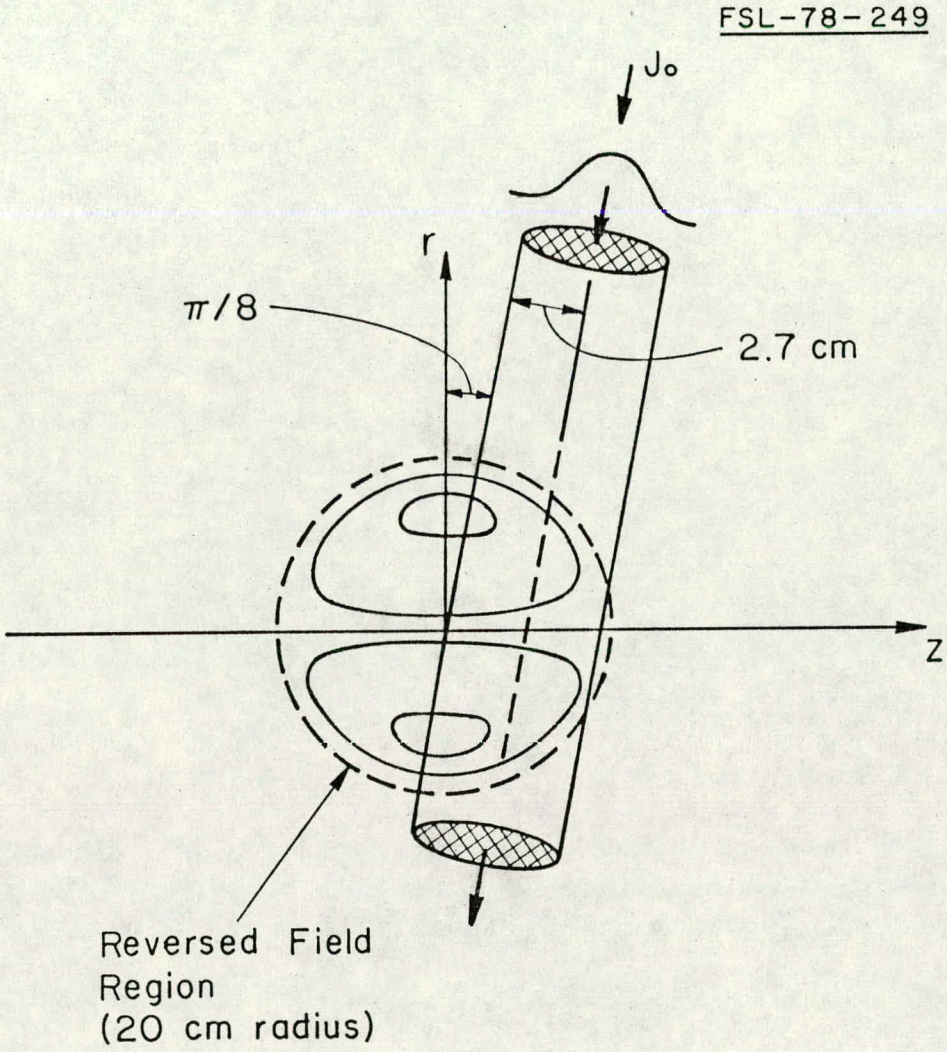

Figure 24. Neutral Beam Injection Geometry for the Trapping Calculation Made in the Code FRMOD. The rotation angle shown ($\pi/8$) was found to give a beam trapping profile that best matched the refueling profile.

that encompasses the projection of the plasma in this plane. The result is divided by the total injected current to find the trapping efficency, which can thus be written as:

$$\eta_{BTj} = 1 - \frac{\Delta y \Delta z}{I_s} \sum_{\ell=1}^{N} J_{o\ell} \exp\left[- \langle\sigma\rangle_{Tj} \int_{x_{s1}}^{x_{s2}} dx' \, n_\ell(x') \right] \quad . \qquad (88)$$

In this form, $J_{o\ell}$ represents the source current evaluated for the appropriate values of y and z (using Eq. 86); $n_\ell(x')$ represents the background density along the path length (found from the same values of y and z, the vortex density profile, and the known rotation angle β); and the values of $x_{s1(2)}$ correspond respectively to the incident (and exit) values of x, for the beam, at this y and z location.

The total trapping cross sections, used in evaluating these trapping efficiencies, are made up of the individual components for the electron, and the ion, interactions and are thus given by:

$$\langle\sigma\rangle_T = \langle\sigma\rangle_{ii} + \langle\sigma\rangle_{ie} + \langle\sigma\rangle_{cx} \quad , \qquad (89)$$

where the $\langle\sigma\rangle_{ii}$ term represents ion-ionization, the $\langle\sigma\rangle_{ie}$ term represents electron-ionization, and the $\langle\sigma\rangle_{cx}$ represents charge exchange. Because the background particles are assumed to have Maxwellian distributions, the averages indicated by the angle brackets can be evaluated as:

$$\langle\sigma\rangle = \frac{2\beta_o}{\sqrt{\pi}v_o^2} e^{-\beta_o^2 v_o^2} \int_o^\infty e^{-\beta_o^2 v^2} \sigma(v) v^2 \sinh(2\beta_o^2 v_o v)\, dv \quad . \qquad (90)$$

In this equation, $\beta_o = \sqrt{m_B/2kT}$ is the inverse of the average background particle velocity, $v_o = \sqrt{2E_o/m_o}$ is the velocity of the injected ion, $m_{B(o)}$ are their respective masses, and v is the relative velocity between the particles. The cross sections, $\sigma(v)$, are then taken from Ref. 47, and the integral over the relative velocity is performed using 26 point Gauss-Laguerre quadrature.

4.4 Fusion Product Heating Estimates

As was indicated earlier, the computer time required for MCFRM calculations makes it impractical to couple the Monte Carlo code directly with the 0-D model; therefore a means of estimating the actual fp energy and particle deposition over a wide range of plasma parameters has been developed. This is made possible through the use of the closed-field and absolute confinement limits discussed in Chapter 2. Studies have shown that virtually all of the closed-field confined fps stay confined within the closed field boundary during slow down; therefore all of their energy (and the particles themselves) are deposited in the closed field region. The remainder of the closed-field energy and particle deposition comes from the marginally confined fps (i.e., those that are absolutely confined but not restricted to the closed field region); consequently both fp energy and particle deposition are represented in terms of the fractional retention of marginally confined fps, and their energy, in the FRMOD code.

The fractional deposition of the marginally confined fps and their energy in the closed field region (respectively referred to as f_{MCP} and f_{MCE}) are, in general, related to the ratio of the fp slowing down time in the hot, closed field region, τ_H, to that in the cold, open field region, τ_c. When τ_H/τ_c is large, the fp deposition should be near the lower, closed-field confinement limit (i.e., f_{MCE} and f_{MCP} will be near zero); but, as τ_H/τ_c becomes smaller, fps which are marginally confined will also be able to deposit a larger fraction of their energy in tne hot region, and fp energy deposition should therefore approach the upper, absolute confinement limit (i.e., f_{MCE} and f_{MCP} will be approaching one).

A similar result is expected as a function of the dimensionless birth energy, E_D, of the fps (where the dimensionless units are those noted earlier, namely $(1/m)(qB_oR_{HV}/c)^2$). This is because the dimensionless energy is a measure of the time which fps spend in the hot (relative to the cold) region. For large dimensionless birth energies, the fps that are marginally confined spend most of their time outside the closed field region, and thus are expected to deposit little of their energy there (corresponding to f_{MCE} and f_{MCP} near zero); but, as the dimensionless birth energy becomes smaller, these marginally confined fps spend more time in the closed field region, and the values for f_{MCE} and f_{MCP} should approach unity.

The final parameter that is expected to influence f_{MCE} and f_{MCP} is the number of slowing down times required to reach thermal energies. This number is related to the parameter $\log(E_o/T_i)$, and if its value is

large (corresponding to many slowing down times) the marginally confined fps will have more opportunities to interact with the hot plasma region than if its value is small. These fps are therefore expected to deposit less of their energy in the open field region because they will tend to be "dragged" inward as they slow down. Consequently, a large value of $\log(E_o/T_i)$ is thought to lead to larger values of f_{MCE} and f_{MCP}.

The influence which these three parameters (τ_H/τ_c, E_D, and $\log(E_o/T_i)$) have on the fractions f_{MCE} and f_{MCP} has caused them to be combined to correlate the values for these fractions that are calculated using the MCFRM code. The results of the correlation search are shown in Figs. 25,26 where the actual values for f_{MCE} and f_{MCP} from selected MCFRM calculations for the six common charged fps (a ^{3}He, T, and p produced by the D-D reaction; an α produced by the D-T reaction; and the α and p produced by D-^{3}He fusion) in a variety of different FRM plasmas are plotted. In both of these figures, the correlation parameter turned out to be equal to $\log[(\tau_H/\tau_c)E_D/\log(E_o/T_i)]$, and (as is illustrated) this correlation provides an excellent means of approximating the actual fp energy and particle deposition over the entire range of parameters. The approximation is then implemented by making use of the fitted curves shown in the figures, and the values for f_{MCE} and f_{MCP} are thus:

$$f_{MCE} = -\,0.42887 \log\left[\frac{\tau_H\, E_D}{\tau_c \log(E_o/T_i)}\right] + 0.25044 \qquad (91a)$$

$$f_{MCP} = -\,0.35011 \log\left[\frac{\tau_H\, E_D}{\tau_c \log(E_o/T_i)}\right] + 0.34500 \qquad (91b)$$

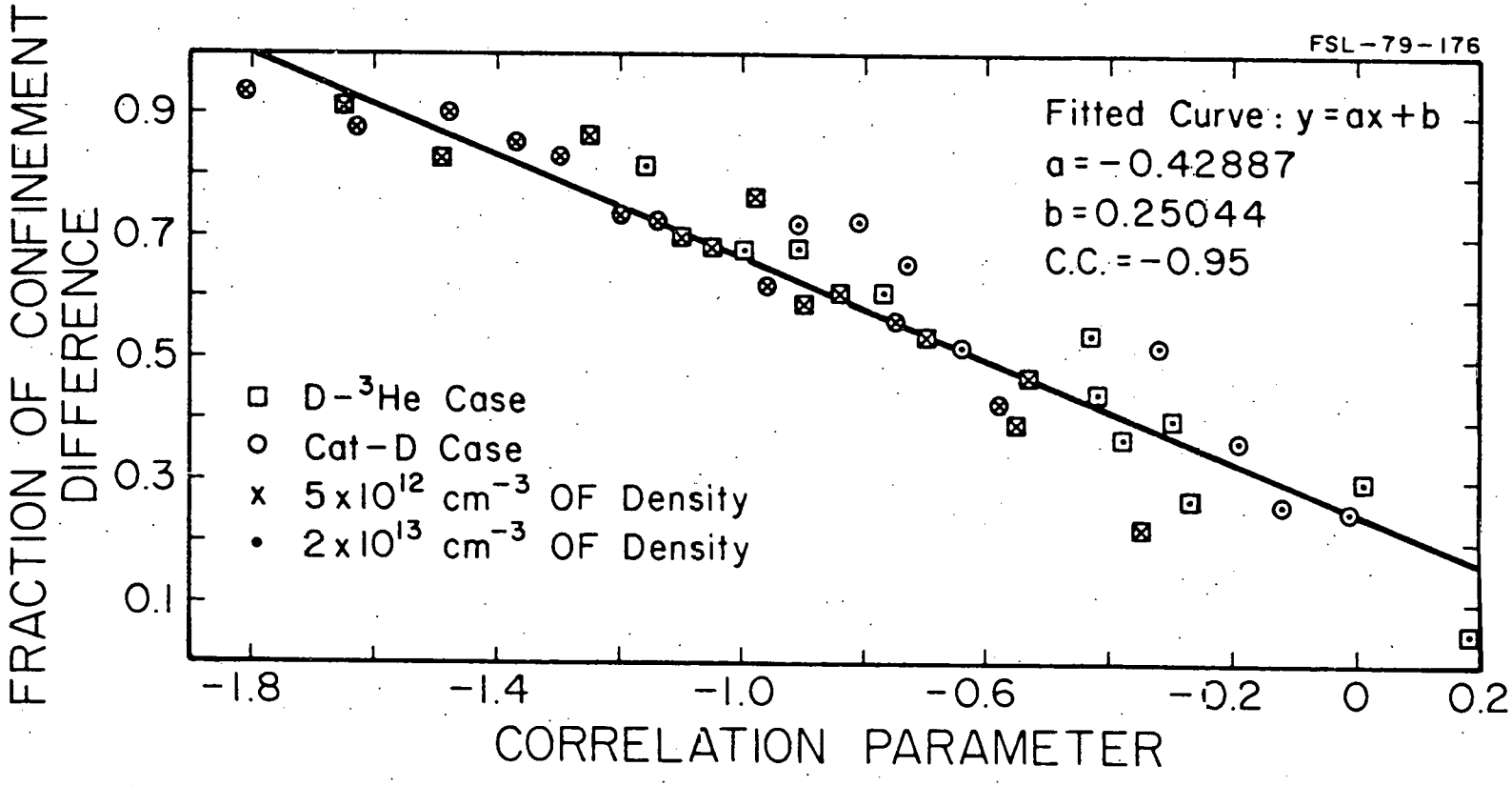

Figure 25. Correlation of the MCFRM Results for the Fracture of the Marginally Confined fp Energy That is Deposited in the Closed Field Region for Typical FRM Plasmas. The correlation parameter is log $[(\tau_H/\tau_c)E_D/\log(E_o/T_i)]$ and the correlation coefficient is -0.95. The line is used to estimate fp energy deposition in the FRMOD code.

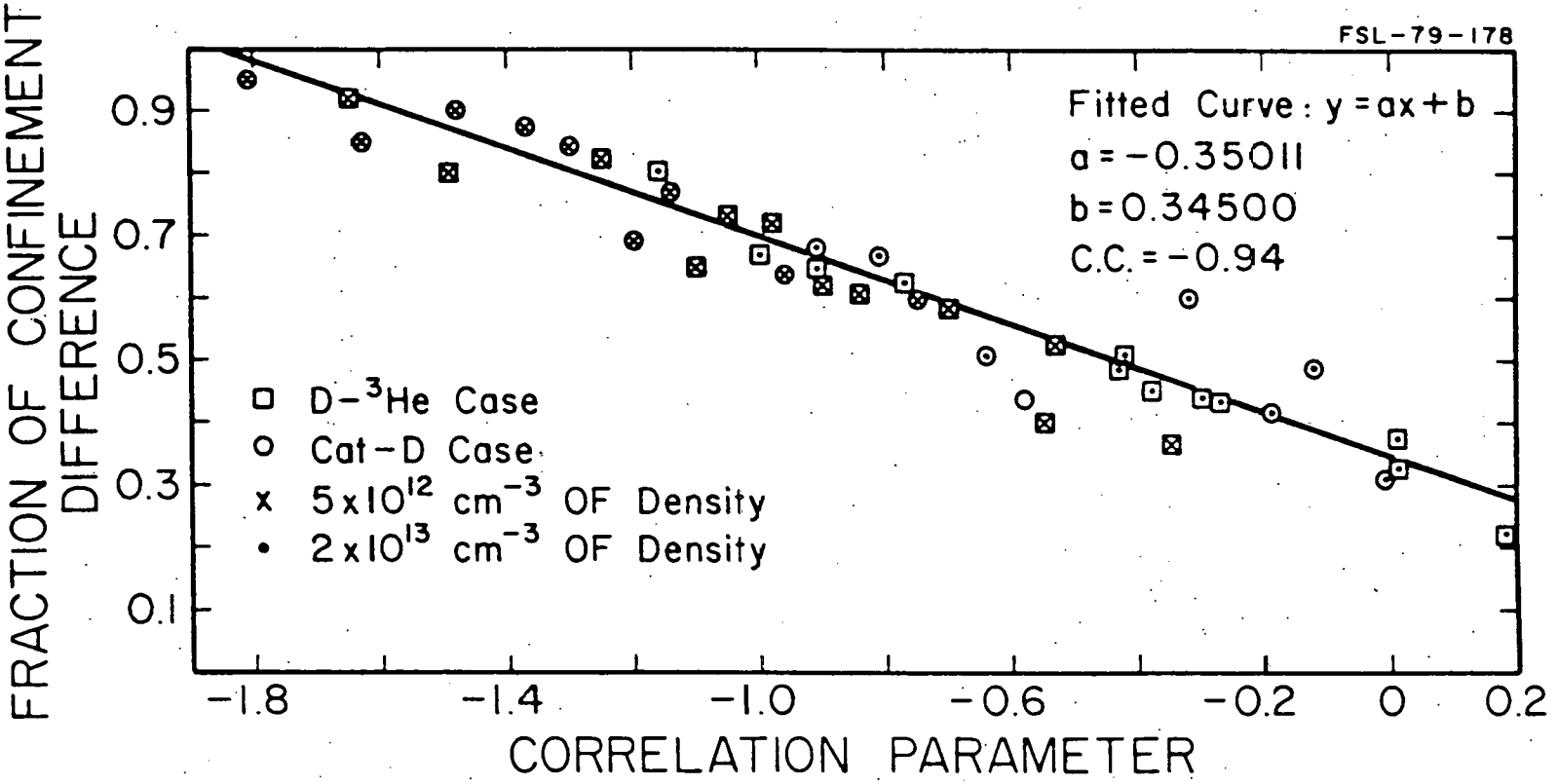

Figure 26. Correlation of the MCFRM Results for the Fraction of the Marginally Confined fps That are Deposited (as ash) in the Closed Field Region for Typical FRM Plasmas. The correlation parameter is again $\log[(\tau_H/\tau_c)E_D/\log(E_o/T_i)]$ and the correlation coefficient is -0.94. The line is used to estimate fp particle deposition in the FRMOD code.

The fraction of fp energy and particles retained in the closed field region is subsequently determined by interpolating between the the closed-field confinement fraction f_{CF} and the absolute confinement fraction f_{AC} (since their difference gives the marginally confined fraction). The fraction of retained energy, f_{RE}, is therefore:

$$f_{RE} = f_{CF} + f_{MCE} (f_{AC}-f_{CF}) \quad , \tag{92a}$$

and the fraction of retained particles, f_{RP}, is similarly given by:

$$f_{RP} = f_{CF} + f_{MCP} (f_{AC}-f_{CF}) \quad . \tag{92b}$$

These fractions (f_{RE}, f_{RP}) will, of course, be different for each charged fp; however, because the confinement limits (f_{AC}, f_{CF}) are general (i.e., not restricted to a specific type of fp) the retained energy and particle fractions for fps other than those mentioned above can also be approximated using this method.

4.5 Scaling Laws

Because the size of the FRM is restricted due to the FLR stabilization, it has somewhat different parametric scaling than is normally found in a fusion reactor. It is therefore useful to consider how the plasma properties are related to the specified parameters: S, κ, and B_o. From the expression for the peak plasma pressure (Eq. 82), and the vacuum magnetic pressure ($B_o^2/8\pi$), an average value for β can be defined for the Hill's vortex FRM model, namely

$$\beta = \frac{9}{35}\,(4+\kappa^{-2}) \quad . \tag{93}$$

The spherical vortex is thus found to make the most efficient use of the applied magnetic field, with elongated plasmas having a β that is reduced by as much as 20% for large values of κ.

This means that the fusion power does not scale linearly with the plasma length, but instead takes on the following form:

$$P_f \alpha \frac{(4+\kappa^{-2})^2\ \kappa\ S^3\ B_o \langle\sigma v\rangle_F}{\sqrt{T_i}\ (1 + f_e\ T_e/T_i)^2} \tag{94}$$

Here $\langle\sigma v\rangle_F$ is the total fusion cross section, $T_{i(e)}$ are the ion (and electron) temperatures, and f_e is the ratio of electrons to ions, n_e/n_i. Similarly, since leakage and bremsstrahlung are the dominate loss mechanisms, the plasma energy multiplication factor Q (defined as the fusion power divided by the total injection power) is given approximately by (for a plasma where fp heating is small):

$$Q \alpha \frac{\langle\sigma v\rangle_F\ \sqrt{T_e}}{415\ \frac{f_e}{\sqrt{m_i}}\ \frac{(4+\kappa^{-2})}{S^2}\ (1 + \frac{T_i}{T_e})\ (1 + f_e\ \frac{T_e}{T_i}) + T_e} \quad . \tag{95}$$

In this relation, the first term in the denominator represents the relative effect of plasma leakage, and the second term (T_e) corresponds to bremsstrahlung losses.

The optimum energy multiplication then occurs when the stability factor is as large as possible and (since $T_e \sim T_i$) falls near the temperature which corresponds to the maximum in the ratio $\langle\sigma v\rangle_F \sqrt{T_e}/(C_L+T_e)$, where C_L is now just a constant equal to $9845/S^2$ for a spherical D-^{3}He plasma. Furthermore, as seen from Eq. 94, larger output powers can be obtained by either elongating the plasma or by increasing the vacuum magnetic field strength. The most attractive of these two alternatives is elongation; however the plasma cannot be made too long because it becomes susceptible to tearing instabilities. To assure that this problem is avoided, the maximum value for the elongation factor is typically taken to be three.

These general scaling laws are useful, but the actual designs may vary from the predicted dependence due to the presence of fp heating and ash buildup. Their influence will tend to reduce the optimum temperature because as the system approaches ignition the Q value begins to peak at lower plasma temperatures where the fusion power input is just beginning to drive the system. It is clear, however, that the FRM is destined to be a small device (due to the limitation on both κ and S), with the only economy of scale coming from the possibility of stacking individual FRM plasmas togetner to form a larger power multiple-celled system.

CHAPTER 5

DISCUSSION OF RESULTS

5.1 Introduction

As was noted earlier, the primary motivation for the studies summarized in this work is an interest in assessing the potential of the FRM as an advanced fuel fusion reactor concept. Indeed, as indicated in this chapter, advanced fuel FRM reactors (i.e., those based on the D-^{3}He and Cat-D fuel cycles) do seem to be feasible (and quite attractive) if future experiments verify that the more optimistic "near-classical" diffusion is characteristic of FRM loss rates. If, on the other hand, the more pessimistic "anomalous" diffusion rates are observed, a viable advanced fuel FRM reactor only appears to be possible if the upper bound on the stability factor S can be extended to fifteen. This chapter will therefore focus on the results obtained for D-^{3}He and Cat-D SAFFIRE reactors with "near-classical" loss rates; however a few results for both D-T systems and those with "anomalous" loss rates will also be presented in order to contrast with the other parameters.

The conceptual reactor designs discussed herein have been termed SAFFIRE (Self-sustained Advanced Fuel FIeld-REversed mirror) reactors to stress the fueling and heating techniques that have been incorporated in an attempt to achieve steady-state operation without the high-energy injection used in other FRM designs. The SAFFIRE concept thus relies upon three important aspects of the Illinois studies, namely the fueling, fp heating and ash buildup, and stability. (The stability aspects of the SAFFIRE design are not addressed, per se, in this work, but they have been examined in detail by Morse [17]. The reader should therefore refer to that study for an in-depth discussion; however, in summary, he concludes that the SAFFIRE design may encounter low growth rate instabilities. He postulates that this may lead to turbulence and enhanced diffusion unless corrective action, such as the possible addition of a quadrupole barrier field, is taken.) To obtain an attractive energy multiplication with advanced fuels, supplemental plasma heating must be held to a minimum, and steady-state or long-pulse operation must be achieved. Calculations show that once reversal is attained, steady-state operation is posible because diffusion-driven, diamagnetic currents will supply most of the reversal current. This allows the beam power to be reduced to a "state of the art" level (i.e., ~1 amp and 10keV). Then, through proper geomertical orientation [42], the beam trapping can maintain the plasma pressure profile, thus sustaining the "driving force" behind the reversal current.

The bulk of the plasma heating is then supplied by fps, supplemented by some auxiliary ion-cyclotron resonance type heating. Steady-state operation consequently relies upon controlling the fp ash buildup, and

the SAFFIRE design includes a cold, flowing plasma on the open field lines that facilitates the "scrape-off" of fp ash. This cold plasma typically has a density of 5-20x10^{12} cm^{-3}, a temperature of 50eV, and (on the basis of a detailed study [40]) should be sustained by the energy it recieves from the marginally confined fps. In addition, this cold plasma layer also serves to shield the closed field region from wall impurities, reducing charge exchange erosion of the plasma surface, and couple the diverted plasma to an energy dump or direct collector.

The remainder of this chapter contains a summary of the SAFFIRE design studies for both D-^{3}He and Cat-D systems. Section 5.2 thus focuses on the FRMOD results relating to various parametric investigations and indicates how the optimum "reference" designs of Section 5.3 were determined. Section 5.3 then summarizes the "reference" case parameters for various systems, while Section 5.4 presents some of the more recent MCFRM results relating to the energy distributions of fps in the FRM and whether or not they give rise to anomalous fp slowing or transport.

5.2 FRMOD Parametric Studies

5.2.1 D-^{3}He Systems

In order to determine the optimum SAFFIRE reactor design, a number of parametric studies were carried out. These studies (summarized in Figs. 27-29) evaluated the plasma energy multiplication, Q, (which is an

approximate figure of merit used to judge overall system performance) over a wide range of the various independent parameters. In the first of these figures the plasma Q-value and the net electrical power output (calculated assuming thermal, direct, and injection efficiencies of 40, 60, and 80% respectively) are plotted vs the ion temperature for several different system parameters. These results (which are for the more optimistic "near-classical" particle confinement time, Eq. 55) indicate that D-^{3}He, FRM reactors are indeed feasible, if these optimistic loss rates are realized. (The low plasma density in the region corresponding to the last "closed" energy surface, Figs. 18a,b, "insulates" the hot, closed-field plasma from the cold, flowing plasma on the open field lines. Particle losses are thus the dominate energy loss mechanism.) Plasma Q-values of ten or more are possible for open field densities of 5×10^{12} cm^{-3} and S factors in the "stable range" (i.e., between five and ten). This corresponds to a small, but efficient, reactor that will produce 0.5MW of net power.

An even more interesting feature of Fig. 27 is however the strong dependence of the system performance on the stability factor S. The SAFFIRE plasma is found to go from a marginal power producer for S of five (Q ~ 1-2), to a reasonably attractive system for S of ten (Q ~ 10-20), to an "ignited" plasma for S of fifteen (Q > 100). (Here the term "ignition is used to denote cases where the only auxiliary heating input to the plasma was that energy supplied by the low energy, 10keV refueling beams.) This exponential dependence is much stronger than that predicted by the general scaling law, Eq. 95 (which finds that Q is proportional to S^2) due to the effect of fp heating. This leads to

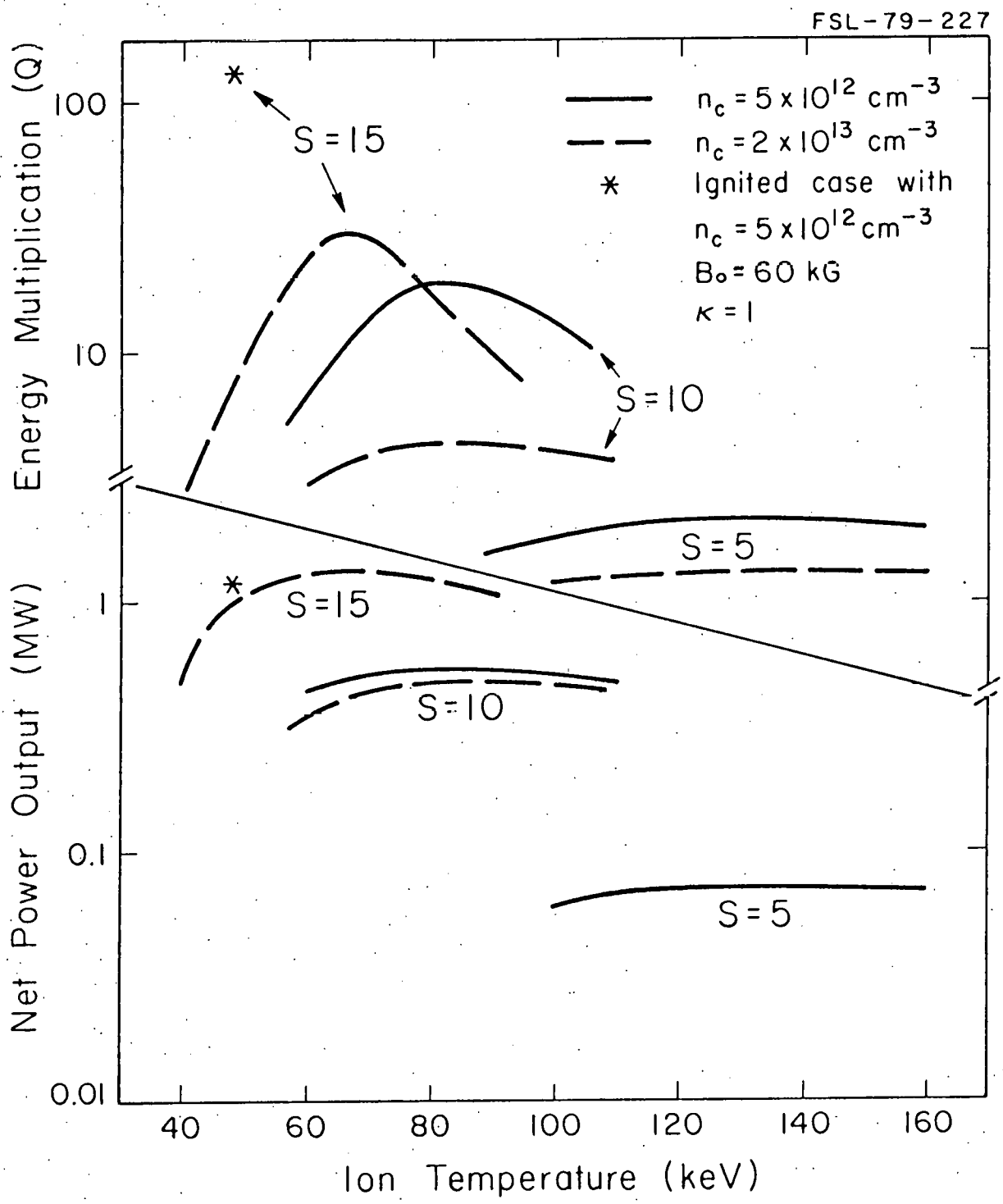

Figure 27. Energy Multiplication Factor and Net Power Output vs the Plasma Ion Temperature for D-^{3}He Systems With "Near-Classical" Loss Rates.

drastic reductions in the required injection power at larger S values; consequently it is extremely important that a theoretical basis be developed for establishing the actual limitations of S in the FRM. Especially if the more optimistic loss rates are not observed, because, as will later be shown, the SAFFIRE concept requires an S of fifteen for the more pessimistic, "anomalous" confinement time of Eq. 56.

A final facet of Fig. 27 relates to the previously mentioned possibility of "ignited" advanced fuel operation in the FRM. If such operation is indeed possible, the cold, flowing plasma on the open field lines could have a very valuable purpose (in addition to protecting the closed field region from neutrals, cf. Ref. 40); that of controlling thermal runaway. As the S = 15 cases of Fig. 27 show, when the open field density is increased from $5x10^{12}cm^{-3}$ to $2x10^{13}cm^{-3}$ the "ignition window" disappears. The flowing plasma has lowered the plasma operating curve by reducing the fp energy deposition in the closed field region; consequently it appears that the open field plasma can be used to assure that the operating curve intersects the ignition curve at only one point, thus leading to thermal stability.

A second parametric study is summarized in Fig. 28. It illustrates the effect of the vacuum magnetic field strength on the plasma Q-value (and the total fusion power output), and another unexpected result is found. Eq. 95 had predicted that the Q-value would be independent of the magnetic field; however this is not the case when fp heating is considered. The plasma energy multiplication increases approximately linearly with the magnetic field strength. The reason for this is again

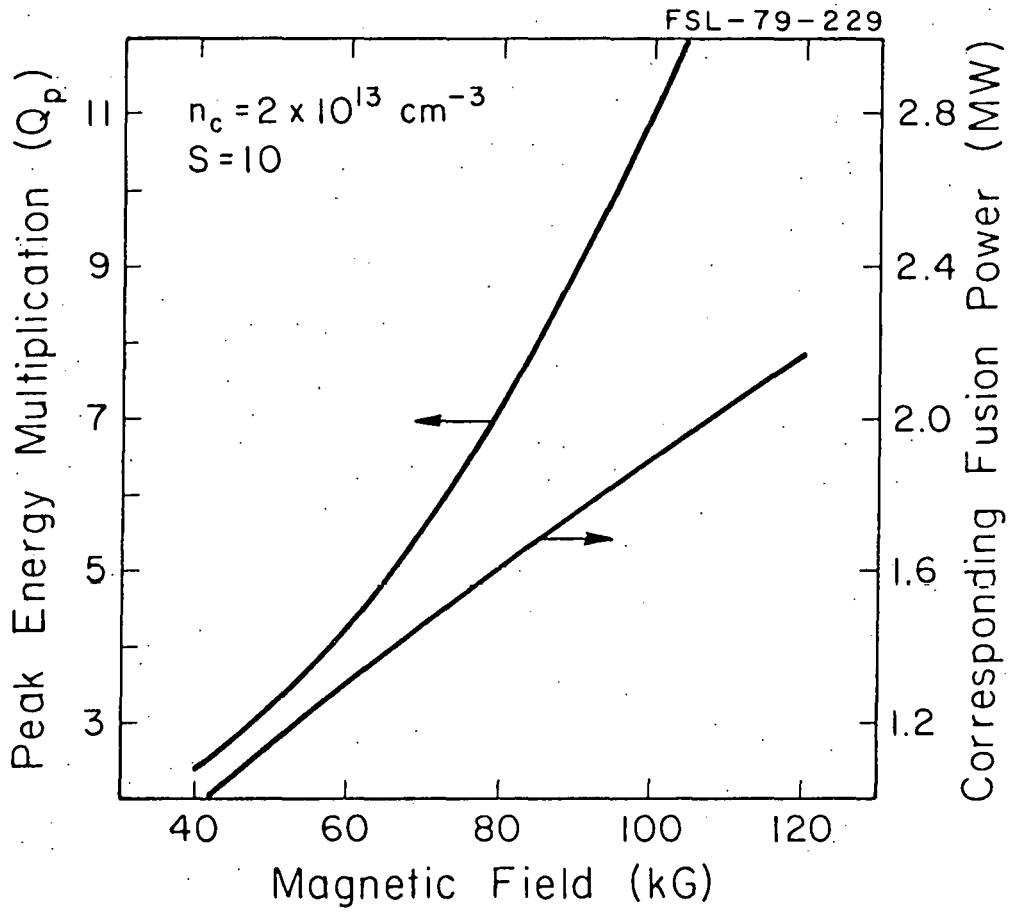

Figure 28. Peak Plasma Energy Multiplication Factor and Corresponding Fusion Power Output vs Magnetic Field Strength for D-^{3}He Systems With "Near-classical" Loss Rates.

the influence of the fp heating term. As the magnetic field (and consequently the closed field plasma density) increase, the ratio of the fp slowing down time in the hot, closed field region to that in the cold, open field region becomes smaller. This causes a larger fraction of the fp energy to be retained in the hot plasma, leading to larger Q-values. Indeed, for the 40kG case only 30% of the fp energy is retained in the SAFFIRE plasma, but for the 100kG case almost 50% fp energy retention is found. The effectiveness of this method for enhancing the plasma performance is, of course, limited due to the economic and technological constraints on the magnetic field coils; therefore a relatively moderate field strength of 60kG has been chosen for the present reference designs. The push to higher fields could become important, however, should "anomalous" loss rates be found to occur.

The final parametric study involves an investigation into the viability of the SAFFIRE concept if the FRM confinement scales like the "anomalous" loss time of Eq. 56. The results of this study are summarized in Fig. 29, where the plasma Q-value is again plotted vs the ion temperature. This figure illustrates that a substantial degradation in the plasma performance ocurs (as expected); however there is still a design window for the SAFFIRE, if the stability limitation can be extended to fifteen. The net power produced by the optimum ($Q \sim 5$) reactor would be 1.8MW and its net efficiency is ~38%.

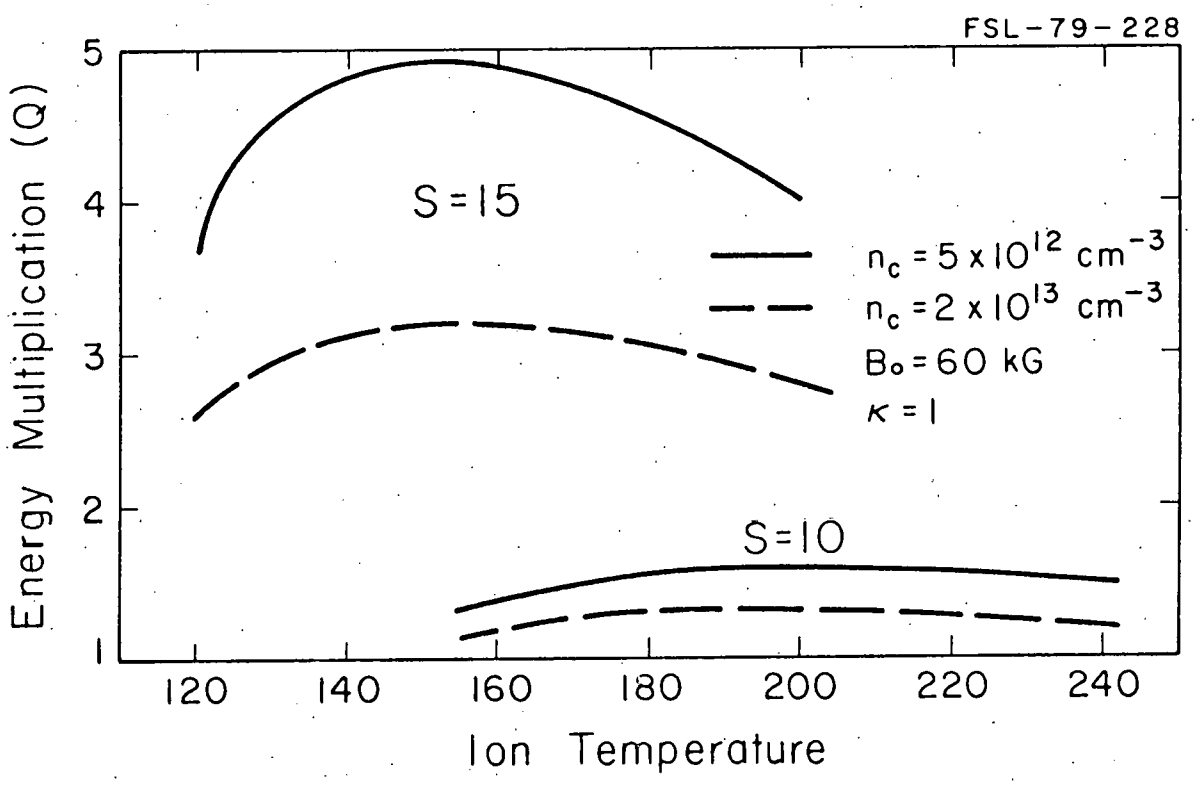

Figure 29. Energy Multiplication Factor vs the Plasma Ion Temperature for D-^{3}He Systems With Anomalous Loss Rates.

5.2.2 Cat-D Systems

A number of similar parametric studies have also been made for Cat-D, SAFFIRE reactors, but the majority of the results are similar to those already presented for D-^{3}He. The Cat-D discussion is therefore limited to the optimization curves shown in Fig. 30. These curves illustrate that Cat-D, FRM reactors are also feasible, having even higher energy multiplication factors than their D-^{3}He counterparts (i.e., a peak Q-value, for S of ten and an open field density of 5×10^{12} cm^{-3}, of 54 as compared to 19 for the equivalent D-^{3}He design). The enhanced Cat-D preformance is due to a combination of small effects, all of which improve the system performance. These effects include: A lower Z-effective which leads to a 36% increase in the fusion power density relative to D-^{3}He and also to a decrease in the radiation losses. An increased energy confinement time (4.6 sec as compared to 3.1 sec for the comparable D-^{3}He system) due to the larger system size that results from the lower charge to mass ratio (hence larger average gyroradius) of the Cat-D plasma ions. A higher charged fp energy retention (69% as compared to 51% for D-^{3}He) which leads to an overall fp heating input, for the Cat-D plasma, that is nearly equal to that for D-^{3}He, in spite of the fact that a much larger fraction of the total Cat-D fusion power is in the form of neutrons. Cat-D FRMs, consequently, also hold the promise of "ignited" operation, if the optimistic loss rates and increased S values are possible. For these "ignited" cases, the open field plasma can again serve as a control over thermal runaway, since the "ignition window" also disappears when the open field density is increased in the Cat-D system.

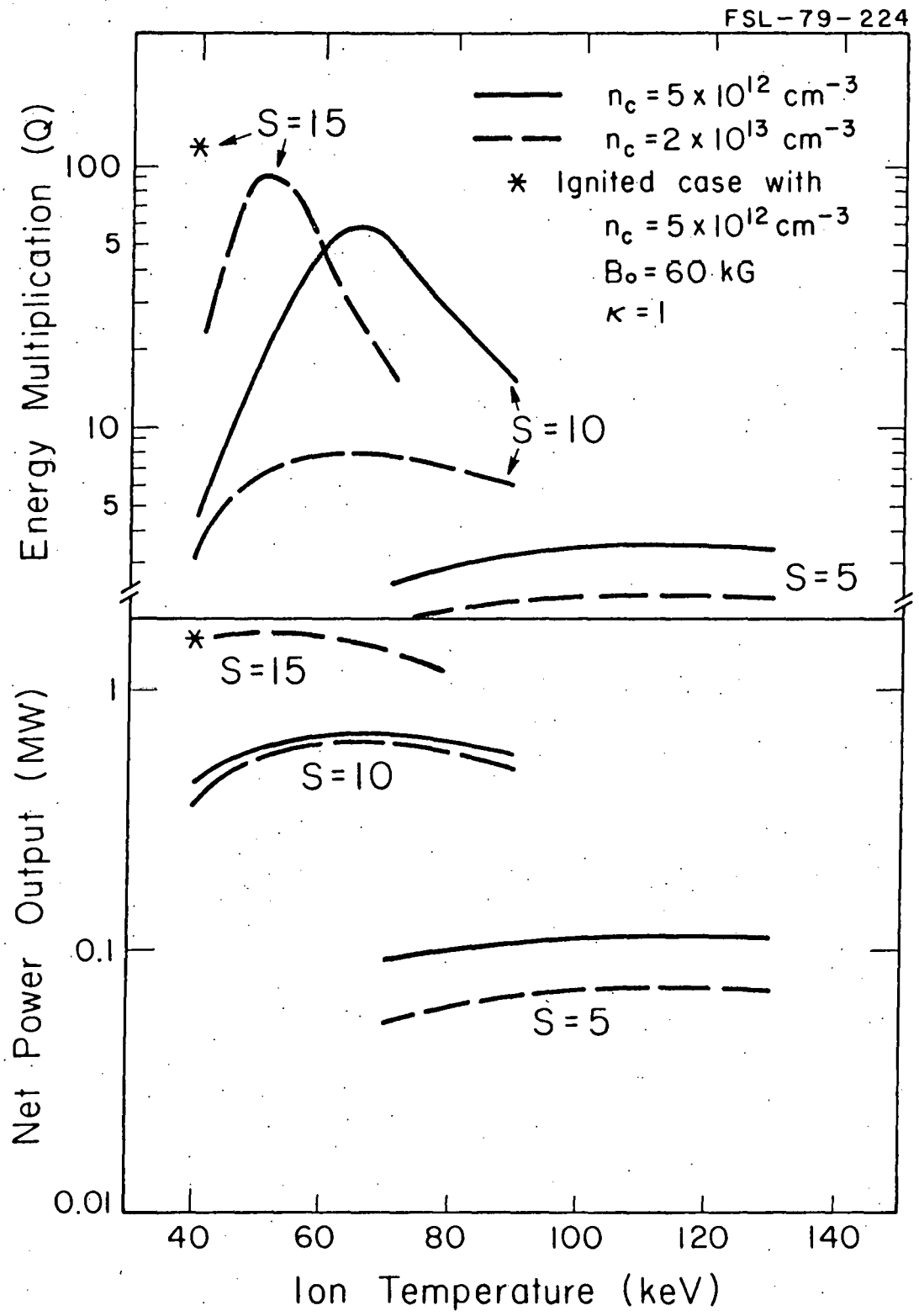

Figure 30. Energy Multiplication Factor and Net Power Output vs the Plasma Ion Temperature for Cat-D Systems With "Near-classical" Loss Rates.

5.3 Reference Case Summaries and Comparisons

5.3.1 D-^{3}He Systems

The first reference case comparison is presented in Table 1 where the plasma parameters for the "optimum" (i.e., peak Q-value) systems with S of five (Case A), S of ten (Case B), and S of fifteen (Case C) are presented. In all three of these cases the "near-classical" loss rates (Eq. 55) were used, and the open field density was 5×10^{12} cm^{-3}; furthermore, for comparison purposes, the vacuum field strength and elongation factor were held at 60kG and one respectively. The most interesting feature of Table 1 is the behavior of the particle and energy confinement times as the stability factor increases. The confinement improves as S increases from five to ten; however for S of fifteen the confinement is worse than that for S of ten, in spite of the fact that the S of fifteen plasma has a smaller surface to volume ratio and should therefore have better confinement.

This paradox occurs because the optimum temperature (i.e., that where the peak Q-value occurs) is lower for the S of fifteen plasma than for S the S of ten case because plasma losses are no longer dominated by leakage (which scales inversly with T). Radiation losses (which are proportional to T) begin to become important and, consequently, a lower optimum temperature results. The lower temperature leads to an increased collisionality, which causes particles to diffuse faster, and, because this effect is stronger than the decrease in the surface to

Table 1

Reference Case Comparison of Principle Plasma Parameters for Three D-^{3}He SAFFIRE Designs With Different Stability Factors

	Case A	Case B	Case C
Stability Factor, $S = \frac{R_{HV}}{3\rho_i}$	5	10	15
Vacuum Field (kG)	60	60	60
Elongation Factor, κ †	1	1	1
Plasma Radius, Volume (cm, ℓ)	14.2, 12	21.5, 42	25.1, 66
Ion, Electron Temp. (keV)	140, 91	80, 76	48, 48
Ion, Electron Density ($x10^{14}cm^{-3}$)	3.7, 5.6	5.3, 7.9	8.9, 13.5
Particle, Energy Confinement Times (sec)	4.5, 1.7	8.0, 3.1	5.3, 2.5
Retained fp Energy (%)	24	51	69
Fractional Ash Buildup (%)	7	16	11
Gross Power (MW)	0.48	1.2	2.4
Radiation (%)	16	28	41
Leakage (%)	77	65	52
Conduction (%)	6	3	2
Neutrons (%)	1	3	5
Energy Multiplication, Q	2.1	19	129
Fusion, Net Electric Power (MW)	0.32, 0.07	1.1, 0.54	2.4, 1.2
Overall Efficiency* (%)	23	49	50

*Assumes thermal, direct, injection, and ICRH efficiencies of 40, 60, 80, and 80% repectively.

†Larger output powers are obtained for elongated ($\kappa > 1$) plasmas.

volume ratio, the "ignited" plasma of Case C has poorer confinement than the driven plasma of Case B. As a result, Case C also has a smaller ash buildup fraction (only 11% as compared to 16% for B) even though the fp retention has increased to 69% (as compared to 51% in Case B).

The most significant feature of Table 1 is, however, the fact that all three cases produce net power. Case A (with S of five) is somewhat marginal, having a Q-value of 2.1 and an overall efficiency of 23%, but Case B (with S of ten) is not. With a Q-value of 19 and an overall efficiency of 49%, the plasma of Case B makes an attractive system. The low neutron production rate (only 3% of the total output power) leads to reduced activation problems and more flexibility in siting (along with a higher overall efficiency); while the ability to elongate individual cells (see Table 4) together with the possibility of stacking many cells into a longer system mean that the SAFFIRE concept could fill an important void in the present fusion reactor scheme--that of providing an intermediate sized (i.e., 50-100MW) power plant [48].

5.3.2 Cat-D Systems

The second reference case comparison (Table 2) is similar to the first except that it invloves Cat-D systems. The "optimum" designs for systems with S of five, ten, and fifteen, having "near-classical" loss rates and an open field density of $5 \times 10^{12} cm^{-3}$, are again shown. The Cat-D results are similar to those for D-^{3}He; however several important differences will be noted here. The first is that the Cat-D plasmas are

Table 2

Reference Case Comparison of Principle Plasma Parameters for Three Cat-D SAFFIRE Designs With Different Stability Factors

	Case A	Case B	Case C
Stability Factor, $S = \frac{R_{HV}}{3\rho_i}$	5	10	15
Vacuum Field (kG)	60	60	60
Elongation Factor, κ[†]	1	1	1
Plasma Radius, Volume (cm, ℓ)	15.2, 15	23.8, 56	27.7, 89
Ion, Electron Temp. (keV)	100, 75	65, 62	40, 39
Ion, Electron Density ($\times 10^{14} cm^{-3}$)	5.9, 6.4	8.0, 9.1	13.1, 15.0
Particle, Energy Confinement Times (sec)	6.0, 2.6	10.3, 4.6	6.9, 3.5
Retained fp Energy (%)	37	69	80
Fractional Ash Buildup (%)	7	14	10
Gross Power (MW)	0.50	1.5	3.5
Radiation (%)	14	24	32
Leakage (%)	53	36	29
Conduction (%)	3	2	1
Neutrons (%)	30	38	38
Energy Multiplication, Q	3.4	59	119
Fusion, Net Electric Power (MW)	0.39, 0.11	1.5, 0.67	3.4, 1.6
Overall Efficiency* (%)	29	46	45

*Assumes thermal, direct, injection, and ICRH efficiencies of 40, 60, 80, and 80% repectively.

[†]Larger output powers are obtained for elongated ($\kappa > 1$) plasmas.

slightly larger than their D-^{3}He conterparts (89 as compared to 66 liters for the S of fifteen cases) due to their lower "effective-Z." This allows the "average" Cat-D plasma ion to have a larger gyroradius than that for the D-^{3}He case, and the result is a larger plasma for the same S factor.

The increased size together with the lower average energy of the Cat-D fps is also reflected in the fp retention for the Cat-D plasmas. In Case B (with S of ten), 69% charged fp retention is found as compared to only 51% for the equivalent D-^{3}He case. As was noted earlier, this fact, together with the improved energy confinement time and lower Z-effective, allows the S of 5 and 10, Cat-D plasmas to attain significantly higher Q-values than are found in the equivalent D-^{3}He systems (e.g., 59 as compared to 19 for S of 10). However, the shift to increased neutron production (hence thermal conversion) causes the Cat-D system to gain little in overall efficiency. In fact, for S of 10 the D-^{3}He system is actually more efficient (49% as compared to 46% for Cat-D) in spite of its lower Q-value. As indicated by Tables 1 and 2, the Cat-D reactors trade-off leakage and neutron power on almost a 1/1 basis. Each per cent increase in neutron production in the Cat-D system corresponds to a per cent decrease in the leakage relative to D-^{3}He. The Cat-D reactors also have slightly smaller radiation and conduction losses due to their lower Z-effective and reduced operating temperatures.

The Cat-D version of SAFFIRE [49] is thus a viable supplement to the D-^{3}He reactors. It does not require the development of a source of ^{3}He,

which could prove to be the "Achilles' heel" of the D-^{3}He fuel cycle, but it does involve a higher neutron production rate, which will lead to increased shielding requirements and activated material. An evaluation of these complicated economic and environmental trade-offs is necessary to determine which fuel cycle is most attractive; however the Cat-D system appears to be especially adaptable to applications involving remote placement or synthetic fuel production.

5.3.3 Systems With Anomalous Loss Rates

The cases discussed in the previous two sections were assumed to have the "near-classical" confinement of Eq. 55. Such confinement is theoretically reasonable for a closed field line geometry such as the FRM; however seldom has theory predicted, in advance, the observed confinement scaling for a fusion device. In order to illustrate the consequence of a more optimistic type of loss mechanism, several cases calculated using the "anomalous" loss rate of Eq. 56 are presented in Table 3. These cases are also for an open field density of 5×10^{12} cm^{-3} and a vacuum field strength of 60kG; however a stability factor of fifteen was required in order to obtain a viable system for the D-^{3}He and Cat-D fuel cycles (S of ten was suficient for D-T).

The most striking feature of Table 3 is the high plasma temperature that is required in the case of the "anomalous" loss rates. This high temperature not only reduces the collisionality of the plasma but also increases the plasma size, both of which serve to decrease leakage. In

Table 3

Reference Case Comparison of Principle Plasma Parameters for D-^{3}He and Cat-D SAFFIRE Designs With "Anomalous" Loss Rates to a D-T Fueled FRM

	D-^{3}He	Cat-D	D-T
Stability Factor, $\varepsilon = \frac{R_{HV}}{3\rho_i}$	15	15	10
Vacuum Field (kG)	60	60	60
Elongation Factor, κ	1	1	1
Plasma Radius, Volume (cm, ℓ)	45.6, 398	49.0, 495	26.0, 74
Ion, Electron Temp. (keV)	160, 115	120, 94	60, 53
Ion, Electron Density ($\times 10^{14} cm^{-3}$)	2.6, 3.9	4.4, 4.9	7.4, 8.1
Particle, Energy Confinement Times (sec)	4.7, 2.6	5.4, 3.0	0.58, 0.32
Retained fp Energy (%)	83	95	79
Fractional Ash Buildup (%)	15	11	9
Gross Power (MW)	5.7	8.8	29
Radiation (%)	30	20	1
Leakage (%)	66	45	16
Conduction (%)	2	1	-
Neutrons (%)	2	34	79
Energy Multiplication, Q	4.9	8.1	57
Fusion, Net Electric Power (MW)	4.7, 1.8	7.9, 3.1	29, 12
Overall Efficiency* (%)	39	40	43

*Assumes thermal, direct, injection, and ICRH efficiencies of 40, 60, 80, and 80% repectively.

addition, the larger plasma also retains a higher fraction of the charged fps, and this is reflected in their energy retention fraction (> 80%). The increased loss rates, however, do keep the ash buildup under control, and the steady-state ash fraction turns out to be no larger than that for the "near-classical" cases (i.e., < 15%).

The key point made by Table 3 is that the SAFFIRE concept is still viable for the "anomalous" los rates, if the current limitation on S can be extended from ten to fifteen. This extension is thought to be a minimal one for two reasons. The first is that the present limit of ten has been chosen based upon the fact that field-reversed theta pinch (FRTP) experiments have successfully operated at $S \lesssim 10$. Their operation at higher S values has not been observed; however this is due to experimental limitations rather than instabilities. It appears that FRTPs can go to higher S values and, due to their similarity, the same should be true for FRMs. Secondly, theoretical investigations of FRM stability have concluded that the FRM configuration is stable in the limit as S -> 1, and that it is unstable for large S values (> 30) where the MHD description becomes valid. The FRM lies in the intermediate ground between these two analysis, and it is not yet clear exactly how large S can become before finite orbit stabilization begins to break down. The extension to S of fifteen thus seems to be no more "questionable" than the selection of "near-classical" loss rates for the earlier reference case studies. Finally, as Case C indicates a viable D-T fueled FRM reactor is feasible even if the present stability bound of ten is found to be the actual limit, and anomalous loss rates are the rule. The output power split from the D-T plasma, of course, shifts

strongly towards neutrons (79% as compared to 34 and 2% for Cat-D and D-^{3}He respectively); however the reduced recirculating power, relative to the Cat-D and D-^{3}He cases, actually leads to a higher overall efficiency for the D-T system. Still, the D-^{3}He device potentially offers the advantage of reduced radioactivity (tritium and induced), making this particularly attractive for small plants where a location near the user is desired.

5.3.4 Elongated Systems

The effect of elongation on the SAFFIRE reference design is summarized in Table 4 where the principle plasma parameters for D-^{3}He and Cat-D systems with S of 10 and "near classical" loss rates are shown. As the table indicates the parametric scaling vs the elongation factor κ is almost exactly as indicated by Eq. 94. The fusion output increases by a factor of ~2 for both D-^{3}He and Cat-D, just as Eq. 94 predicts for $\kappa = 3$, while the Q value decreases slightly relative to the $\kappa = 1$ case. This latter result is not accurately predicted by Eq. 95, again because of the effect of fp heating. While the actual superthermal fp confinement is unaffected by system elongation, the closed field fp energy deposition is slightly less in an elongated plasma, (relative to the corresponding spherical case) due to the reduced β (Eq. 93). The lower β leads to lower background densities for elongated FRM plasmas, and, as a result, to reduced fp energy deposition (i.e., 49% for the $\kappa = 3$ case vs 51% for $\kappa = 1$). The Q values are thus slightly lower for the elongated case because the reduction in fp heating is offset by an increase in the injection power.

Table 4

Reference Case Comparison of Principle Plasma Parameters for Two Elongated SAFFIRE Designs with D-^{3}He and Cat-D Fuel Cycles

	D-^{3}He	Cat-D
Stability Factor, $S \equiv \frac{R_{HV}}{3\rho_i}$	10	10
Vacuum Field (kG)	60	60
Elongation Factor, κ	3	3_o
Plasma Radius, Volume (cm, ℓ)	21.5, 125	22.8, 150
Ion, Electron Temp. (keV)	80, 75	60, 57
Ion, Electron Density ($x10^{14}cm^{-3}$)	4.4, 6.6	7.2, 8.1
Particle, Energy Confinement Times (sec)	11.6, 4.3	12.6, 5.5
Retained fp Energy (%)	49	67
Fractional Ash Buildup (%)	18	14
Gross Power (MW)	2.3	2.9
Radiation (%)	29	25
Leakage (%)	64	36
Conduction (%)	4	2
Neutrons (%)	3	37
Energy Multiplication, Q	16	37
Fusion, Net Electric Power (MW)	2.2, 1.1	2.9, 1.3
Overall Efficiency* (%)	48	45

*Assumes thermal, direct, injection, and ICRH efficiencies of 40, 60, 80, and 80% repectively.

Elongated plasmas do however have other characteristics which offset their reduced Q-values. The most significant of these characteristics are an increased net power output per cell (i.e., 1.1 and 1.3MW respectively for the D-^{3}He and Cat-D plasmas as compared to 0.54 and 0.67MW for the corresponding spherical cases), and a possible enhanced resistance to instability (as postulated by Morse [17]). In addition, the elongated plasma is also more attractive from an engineering standpoint because a larger fraction of the total vacuum volume is filled with hot plasma (due to the fact that there are fewer intervening "breaks" between cells per unit length) and because a smaller number of individual cells are required to reach a given total output power. This latter point greatly reduces the complexity of the supporting systems; however plasma elongation is limited by the onset of tearing instabilities to $\kappa < 5$. A conservative value of $\kappa = 3$ has thus been chosen for the present studies.

As a result of these arguments, the parameters from Table 4 have served as the basis for an overall economic evaluation of the SAFFIRE reactor concept [48], and the system potentially appears to be economically competative. Under the optimistic assumptions of mass production of units, 60% direct conversion efficiency, 40% thermal conversion efficiency, and the previously mentioned physics scaling, the SAFFIRE reactors produce power at a cost of ~ 45mills/kw-h. This compares favorably with that produced by current oil fired "peaking" units, and it becomes competative with coal fired units for coal prices of ~ \$50/ton (presently ~ \$25/ton). The SAFFIRE concept thus could conceivably offer a viable supplement to the larger and more capitol

intensive Tokamak and Tandem Mirror reactors assuming that the basic confinement principle (i.e., stable, steady-state field-reversal) with "near-classical" particle loss rates) can be verified, and that the conditions postulated in the economic analysis of Ref. 48 develop (namely, the feasibility of mass production of small, local fusion units). If, however, the optimistic "near-classical" confinement scaling is not observed, a viable SAFFIRE reactor does not appear to be attainable unless the present stability limitations can be extended from 10 to 15).

5.4 Fusion Product Energy Distribution Functions

5.4.1 Introduction

Since the SAFFIRE reactors require a high plasma temperature ($T_{i,e} > 40$-keV) due to their advanced-fuel nature, most of the fps in these reactors mainly slow down through Coulomb collisions with background ions. Because the rate of energy transfer to ions increases as the fp energy decreases (Fig. 31) the high electron temperatures flatten the distribution function of fps in SAFFIRE relative to those found in low temperature D-T fusion reactors. Such distributions may give rise to anomalous slowing and alpha transport [50]; therefore the energy distributions of fps in SAFFIRE have been examined. The analysis has focused on the 3.67-MeV alphas and 14.7-MeV protons produced in the D-^{3}He reaction; however the techniques are general and thus apply to other fps as well.

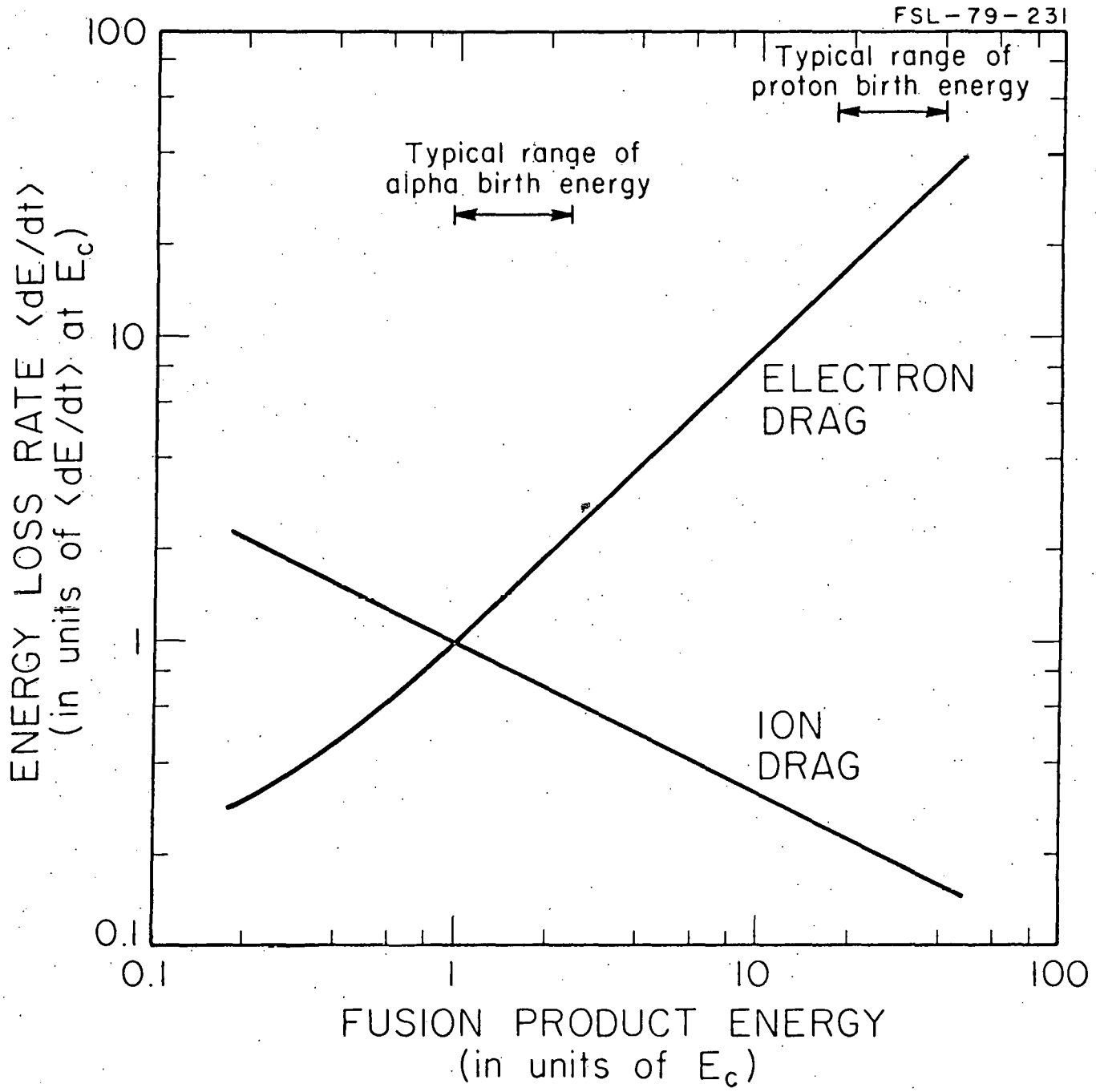

Figure 31. Comparison of Relative Contributions of Electron and Ion Drag in SAFFIRE. For this case $\bar{n}_e = 1.5\ \bar{n}_i = 7.5 \times 10^{14} cm^{-3}$ and $T_{i,e} = 50$-keV.

It should be noted that the consequences of anomalous slowing are not clear. Physically such slowing could occur by resonant coupling of energy from the fp into wave energy associated with the background plasma (e.g. Alfven waves are a potential background mode considered in several analyses [50]). At the best, the main consequence would be to reduce the fp slowing down time, reducing the loss fraction and enhancing energy deposition. If, indeed, this occured, present SAFFIRE results would be conservative and ignition might be easily achieved. On the other hand, various complications could off-set this benefit. Depending on the details of the particle-wave coupling, velocity space diffusion could result in enhanced losses. Further, waves induced in the background could result in turbulence and in increased energy and particle loses from the thermalized plasma. A clear understanding of these effects is not possible based on studies of anomalous slowing to date, and this is beyond the scope of the present study. However, since the MCFRM code makes it possible to calculate fp distribution functions based on classical slowing, it was thought to be important to examine these distributions to see if conditions (namely a sufficiently positive slope of the energy distribution function) exist that could trigger anomalous slowing.

Finally, it might be noted that there is not experimental evidence for anomalous slowing to date. Some neutral beam injection experiments on tokamaks should have, according to theory, encountered threshold effects. However none have been reported. Still, with injection only at 25-keV, these experiments are quite different from conditions expected in

fusion grade plasmas with MeV fusion products. Thus, the possibility of anomalous slowing can not be ignored.

In order to establish a framework for evaluating the MCFRM results in the more complicated FRM cases, a brief summary of a Fokker-Planck analysis of fp distributions in a uniform plasma, developed by Ohnishi [51], will first be presented. The form which the Fokker-Planck equation assumes in this application is:

$$\frac{\partial f}{\partial t} = \Gamma\left\{(2v^3)^{-1}\frac{\partial^2}{\partial v^2}\left(v^2\frac{\partial^2 g}{\partial v^2}f\right)-v^{-2}\frac{\partial}{\partial v}\left[f\left(v^2\frac{\partial h}{\partial v}+\frac{\partial g}{\partial v}\right)\right]-\frac{f}{\tau_p}+\frac{S\delta(v-v_o)}{4\pi v^2}\right\} \quad (96)$$

where f is the velocity dependent fp distribution function, $\Gamma = 4\pi e^4 Z^2 \ell_n \Lambda / m^2$, and S is the birth rate of the fps. In this form the leakage associated with τ_p is assumed to be isotropic and independent of energy. This assumption is not entirely valid; however, as the results will show, Eq. 96 does provide a good first approximation to the actual case.

General expressions for the Rosenbluth potentials h and g are given in Ref. 52, but for the present application, where $v_i > v >> v_e$ ($v_{i,e}$ are the background ion and electron thermal velocities), the coefficients of Eq. 96 can be simplified to:

$$v^2\frac{\partial h}{\partial v}+\frac{\partial g}{\partial v} = -\frac{4}{3\sqrt{\pi}}\frac{m}{m_e}\frac{n_e v^3}{v_e^3} - m \qquad \frac{n_j Z_j^2}{m_j} \quad (97a)$$

$$\frac{\partial g}{\partial v} = \sum_j n_j Z_j^2 = n_e Z_{eff} \quad (97b)$$

$$v^2\frac{\partial^2 g}{\partial v^2} = \frac{4}{3\sqrt{\pi}}\frac{n_e v^2}{v_e} + \frac{1}{v}\sum_j n_j Z_j^2 v_j^2 \quad (97c)$$

These simplifications can subsequently be used to allow an approximate solution for the fp energy distribution function f(E) to be expressed in the following simple form:

$$f(E) = \frac{S\tau_s (E_o^{3/2} + E_c^{3/2})^{\gamma/3}}{(E_o^{3/2} + E_c^{3/2}} \frac{\sqrt{E}}{(E_c^{3/2} + E^{3/2})^{\gamma/3}} \tag{98}$$

where

$$\tau_s = \frac{3\sqrt{2}\ m\ T_e^{3/2}}{8\sqrt{\pi}\ \sqrt{m_e}\ n_e e^4 Z^2 \ell n\Lambda} \tag{99}$$

$$E_c = \left[\frac{3\sqrt{\pi}}{4n_e} \sum_j \frac{n_j Z_j^2}{m_j}\right]^{2/3} \frac{m}{m_e^{1/3}}\ T_e \tag{100}$$

$$\gamma \doteq 3 - \tau_s/\tau_p \tag{101}$$

$$T_e = \frac{m_e}{2}\ v_e^2 \tag{102}$$

Thus τ_s is the electron drag time for the fps, E_c is the critical energy i.e., the energy at which the electron and ion drag contributions are equal, and E_o is the fp birth energy. The above analytical form (Eq. 98) is particularly valuable in interpreting the actual FRM cases.

5.4.2 Analytical Approximation

The predicted dependences of the fp energy distribution functions on the plasma electron temperature and the superthermal particle loss rate

are summarized in Figs. 32,33 for D-^{3}He alphas and in Figs. 34,35 for D-^{3}He protons. The superthermal proton distribution is found to have "good" curvature (i.e., negative slope) under almost all conditions, with only severe loss during slow down giving rise to a flattened distribution; however, such is not the case for alphas. Due to the high electron temperatures found in SAFFIRE (i.e., T_e > 40keV), the critical energy (which is ~ $10.5m_{fp}T_e$ for the D-^{3}He SAFFIRE plasmas) is nearly equal to the alpha birth energy. The shape of the alpha distribution is thus strongly dependent on the electron temperature.

For T_e > 50-keV, the critical energy is nearly equal to the alpha birth energy and the alphas slow down mainly through Coulomb collisions with ions. Since the ion drag is a decreasing function of energy and $f(E) \propto 1/\langle dE/dt \rangle$, this causes the superthermal alpha energy distribution to have regions of positive slope, as shown by the curves in Fig. 32. Many of the reference case designs presented in Section 5.3 had T_e > 50keV; therefore it is important that the distribution of alphas in the FRM be investigated in order to determine the extent of this effect and whether or not it can lead to anomalous slowing. Superthermal particle losses can also affect the energy distribution of the alphas, and (as shown in Fig. 33) the loss of alphas during slowing down also leads to regions of positive slope.

The preliminary results thus indicate that high energy protons in the FRM will have a more conventional $E^{-3/2}$ shaped energy distribution function and are not expected to experience anomalous slowing, unless

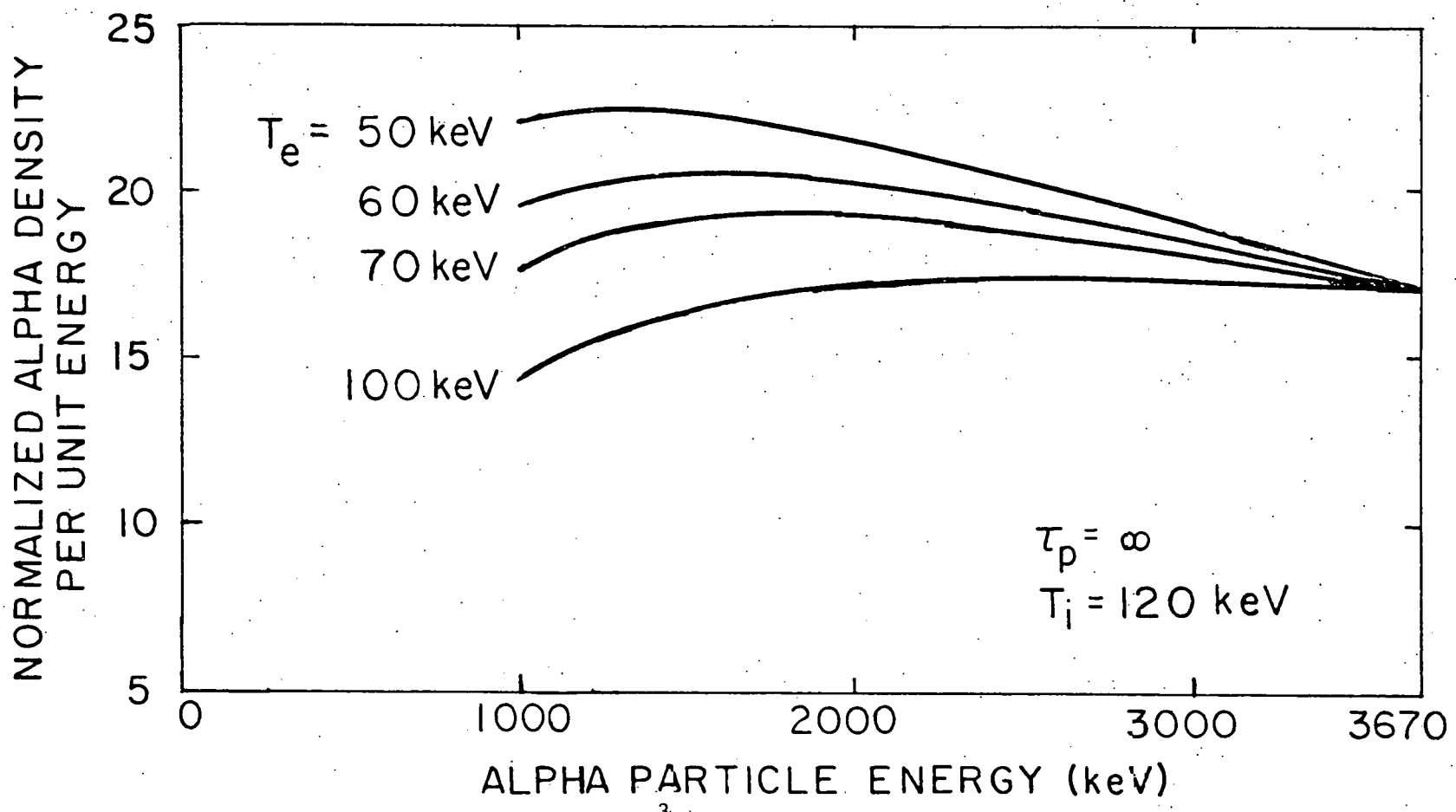

Figure 32. Energy Distribution of D-^{3}He Alphas at Several Electron Temperatures for an Ion Temperature of 120 keV and no Particle Loss During Slow-down. The critical energy is greater than the alpha birth energy for all cases except T_e=50keV where is is 3.2 MeV.

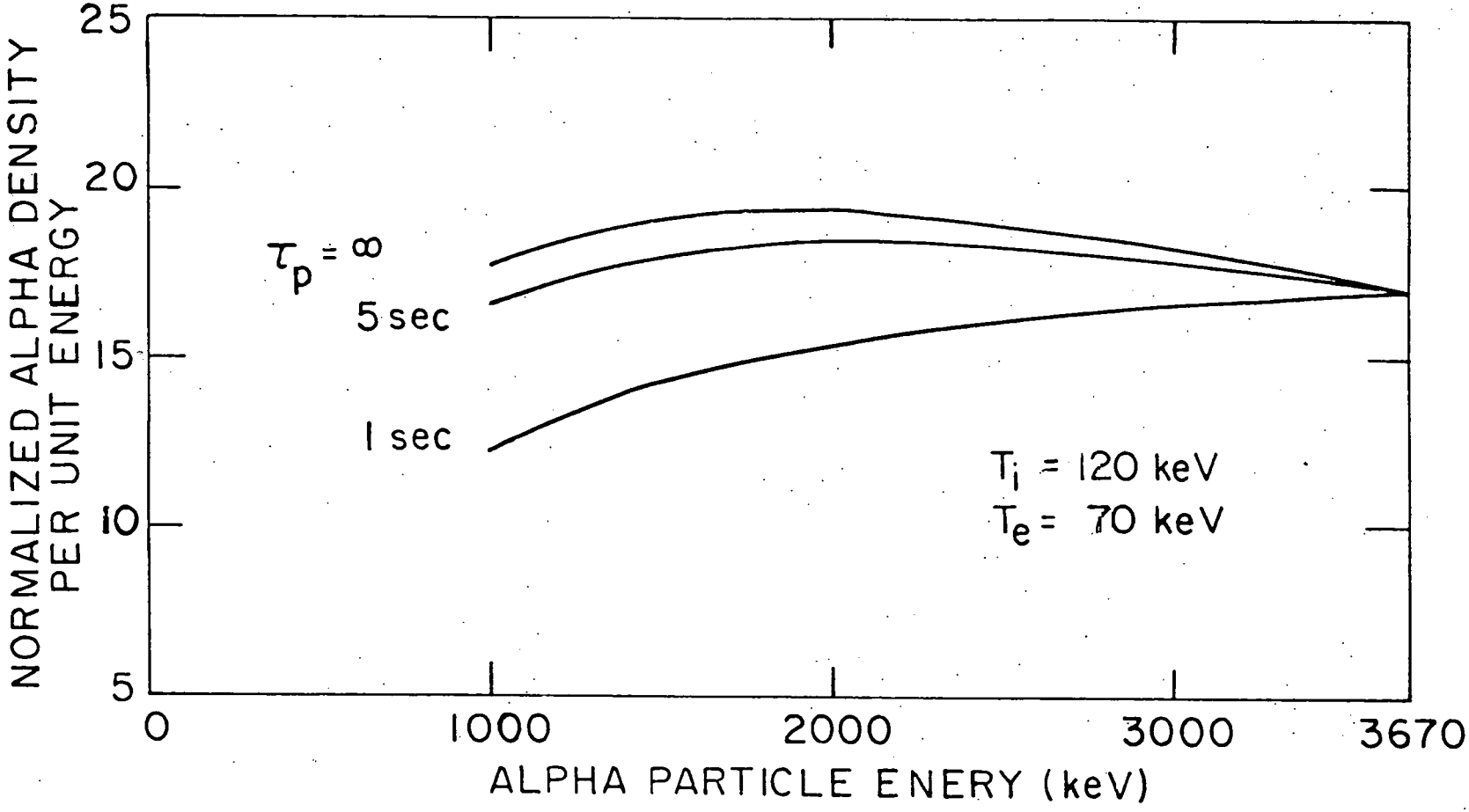

Figure 33. Energy Distribution of D-^{3}He alphas for several different loss rates during slowdown. The critical energy is 2.94 MeV for all three cases.

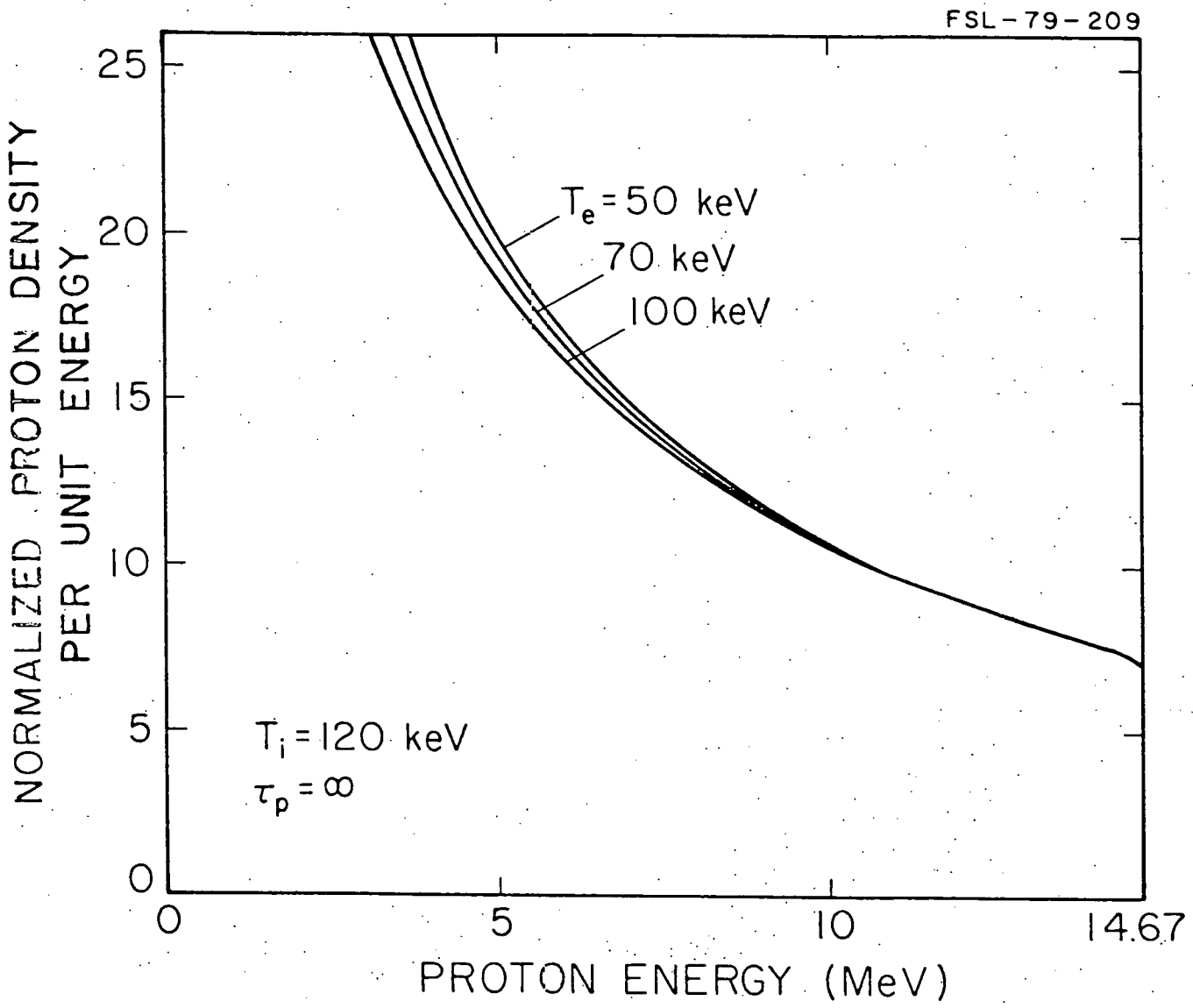

Figure 34. Energy Distribution of D-^{3}He Protons at Several Electron Temperatures for an Ion Temperature of 120 keV and no Particle Loss During Slow-down. For all cases the critical energy is less than 1.1 MeV .

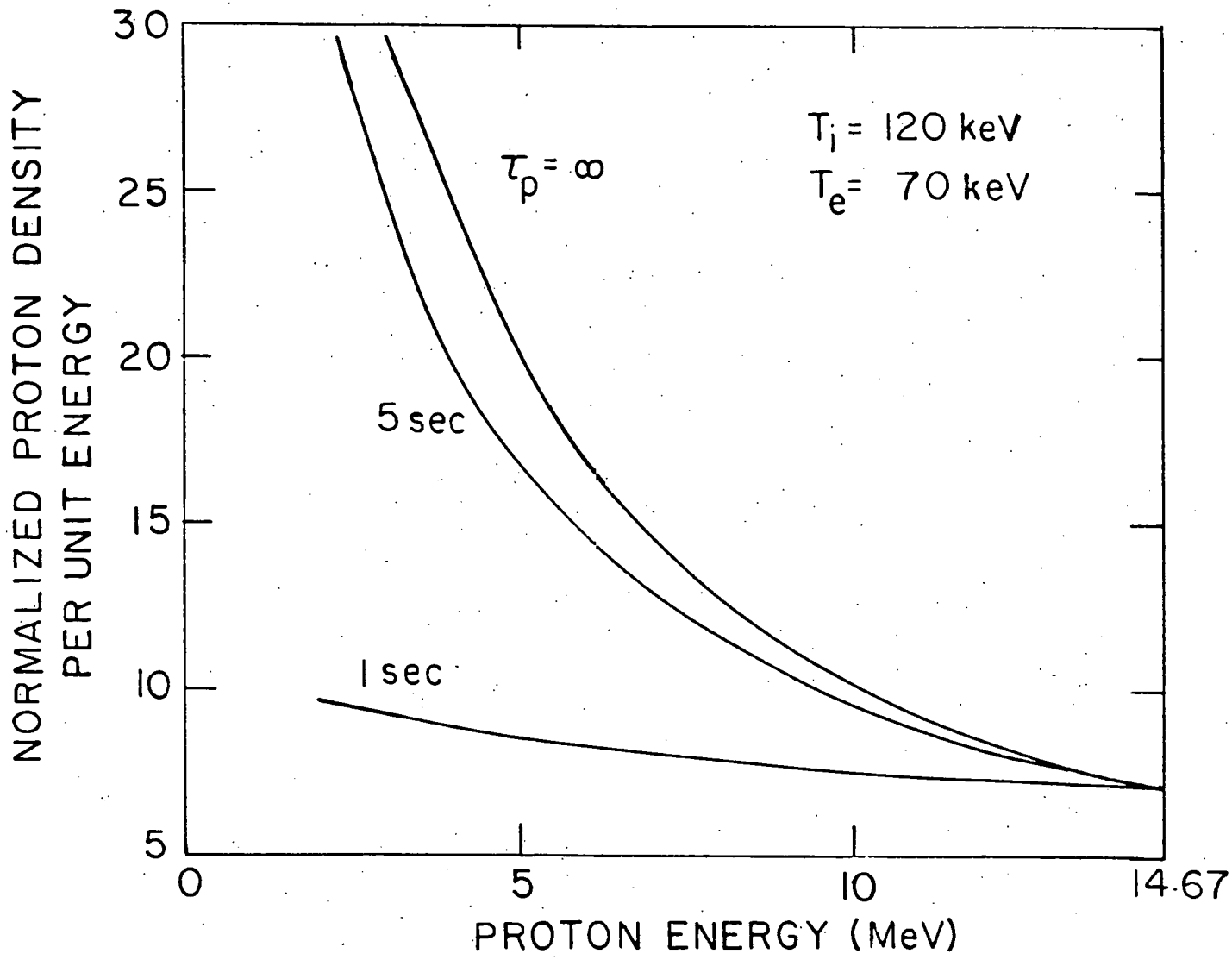

Figure 35. Energy Distribution of D-^{3}He Protons for Several Different Loss Rates During Slow-down. The critical energy is 0.74 MeV for all three cases.

there are substantial losses during slow down, or the distributions are anisotropic. The latter may be a problem for protons in SAFFIRE because their high energy gives rise to a significant fraction of prompt losses which <u>are</u> anisotropic. Since the sufficient conditions for anomalous effects are that $\partial f(\vec{v})/\partial v_{\parallel}$ or $\partial f(\vec{v})/\partial v_{\perp}$ be greater than zero in some region of velocity space [50], a more detailed look at the proton distribution is needed in order to draw any final conclusions regarding their resistance to anomalous slowing. Such a detailed analysis is beyond the scope of this work, however the fact that their average slope is negative is encouraging.

The preliminary results for the alpha distributions are quite different. Their distributions are found to exhibit regions of positive slope for typical SAFFIRE conditions. It should be remembered, however, that positive slope is a necessary, but not a sufficient condition for anomalous slowing and transport under the isotropic conditions expected to exist for alphas due to their reduced prompt losses. The sufficient conditions [50] are again that $\partial f(\vec{v})/\partial v_{\parallel}$ or $\partial f(\vec{v})/\partial v_{\perp}$. These conditions are not satisfied for any of the preliminary alpha results under the isotropic assumption. Severe loss during slow-down ($\tau_p < 1$ sec) may, however, produce either of these conditions in the alpha distribution. The MCFRM results are thus particularly valuable in identifying if superthermal losses are significant, and if they can be controlled by varying the system parameters.

5.4.3 MCFRM Results

The actual distribution of alpha particles in the FRM is shown in Figs. 36,37. In Fig. 36 the "ideal" case with no open field plasma ($n_c = 0$) is compared to the "standard" case (with a 50-eV, $n_c = 3.2 \times 10^{13}$ cm^{-3} plasma on the open field lines), while Fig. 37 illustrates how a change in the plasma size (or equivalently the stability factor) affects the alpha distribution. As these figures show, the actual results are similar to those predicted by the analytic approximation; however the open field plasma (which can only be treated via MCFRM) is found to shift the region of positive gradient to lower energies. The open field plasma does this by lowering the "effective" electron temperature which the alphas sample during slow-down. This, in turn, lowers the critical energy and along with it, the region where $\langle dE/dt \rangle$ is a decreasing function of energy. Increased superthermal-particle losses, resulting from particle interactions in the cold plasma layer, thus do not give rise to anomalous alpha slowing or transport in typical SAFFIRE plasmas, as long as the distributions remain isotropic.

Several other features of the cold plasma layer are depicted by Fig. 37. The discrepancy between the results for $n_c = 0$ and $n_c = 3.2 \times 10^{13}$ cm^{-3} is explained by recognizing that a decrease in the plasma size introduces two competing effects (when a cold, open-field plasma is present). The first is an increase in particle loss during slow-down, which causes a reduction in the energy distrubiton at lower energies (cf. Fig. 33), and

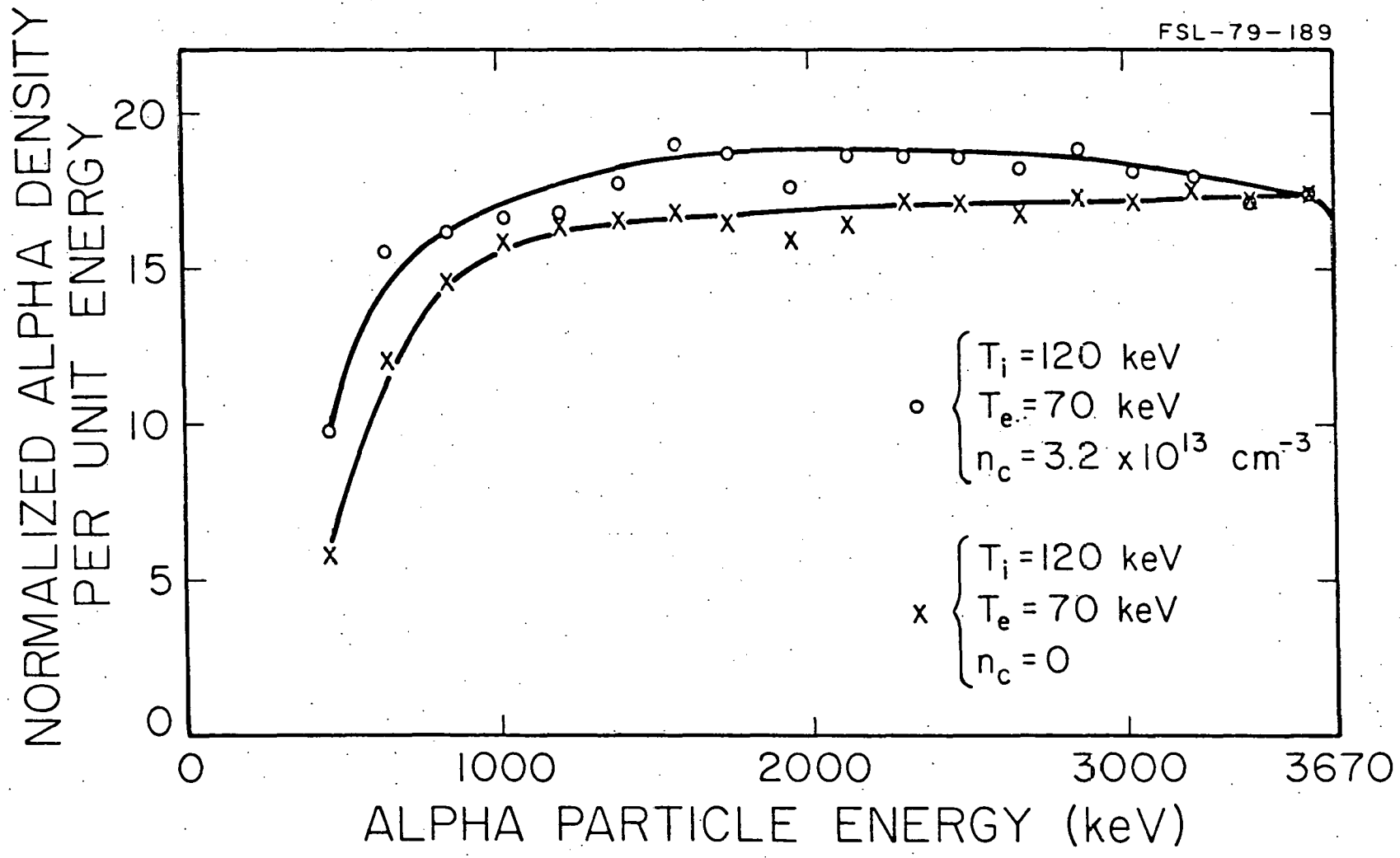

Figure 36. Energy Distribution of D-^{3}He Alphas in tow Equivalent FRMs, One Having no Plasma on the Open Field Lines. Note the effect of the lower "average" electron temperature due to the cold, open field plasma.

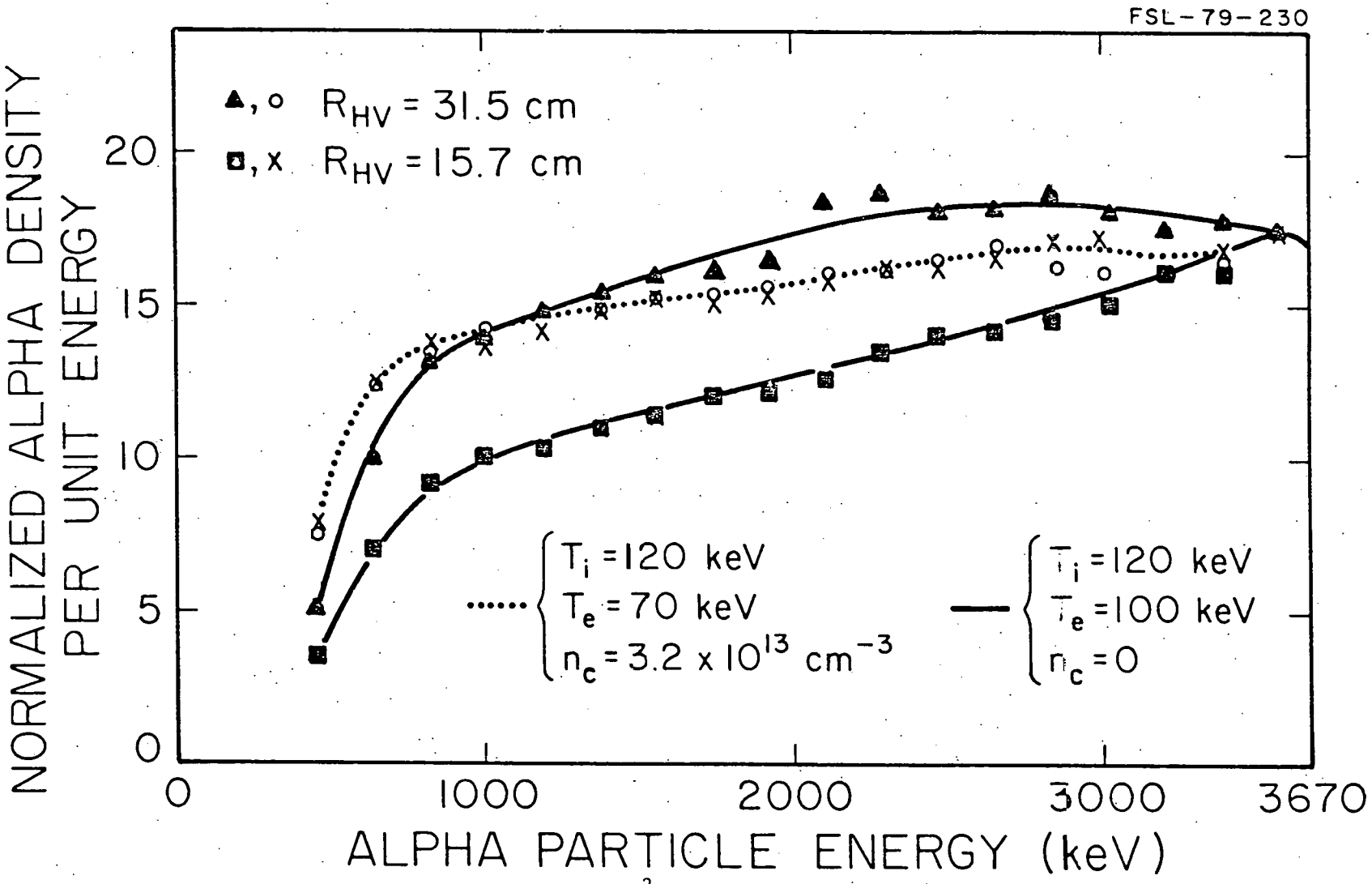

Figure 37. Energy Distribution of D-^{3}He Alphas in two Different Sized FRM Plasmas. Note that the distribution is independant of plasma size when a cold, open field plasma is present.

the second is a decrease in the "effective" electron temperature, which causes an increase in the energy distribution at lower energies (cf. Fig. 32). With $n_c = 0$, only the effect of increased losses during slow-down is present, and the positive gradient of the alpha energy distribution is increased in the smaller 15.7-cm plasma. The lower "effective" electron temperature (resulting from interaction in the open field region) introduces an opposing influence in the $n_c = 3.2 \times 10^{13}$ cm^{-3} case, however, and the net result is a distribution that is independent of the plasma size. It should be noted that none of these results meets the sufficient conditions for anomalous slowing (i.e., $\partial f/\partial v_{\parallel} > 0$ or $\partial f/\partial v_{\perp} > 0$), assuming isotropic distributions. Future work will therefore focus on the isotropic assumption in order to determine its validity in the presence of increased superthermal losses.

The proton birth energy is much greater than that of the alphas; consequently the protons slow down mainly by electron interactions. The electron drag is an increasing function of energy (cf. Fig. 31); thus the proton energy distribution was expected to have a negative gradient and (in general) does, as the analytic results (Figs. 34,35) showed. The only effect which was found to introduce a positive gradient into the proton energy distribution was a severe loss during slow-down (i.e., $\tau_p < 1$ sec); therefore the only proton distribution study presented involves a reduction in plasma size in order to increase slowing down losses. The results of this study (shown in Fig. 38) illustrate that proton energy distributions in smaller plasmas do have reduced negative gradients, but are still not susceptible to any anomalous effects, unless they result from anisotropy.

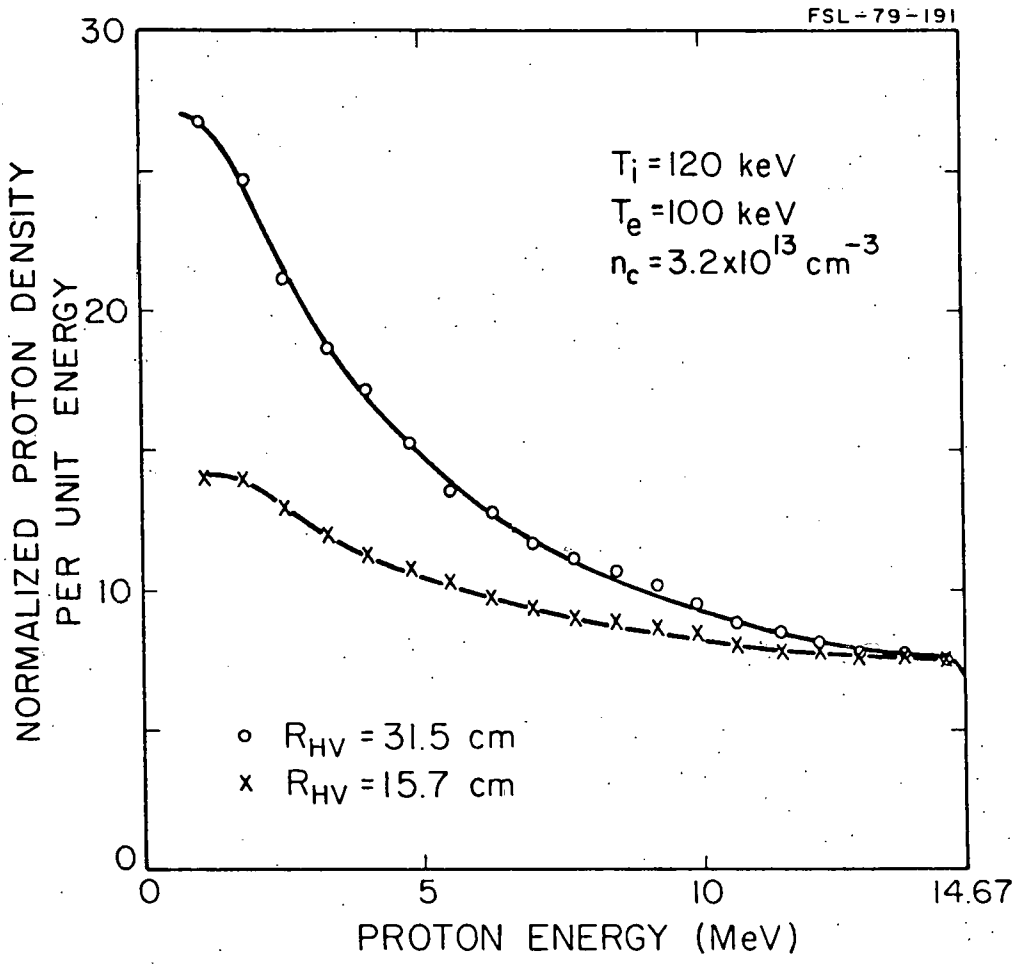

Figure 38. Effect of Plasma Size on the Photon Energy Distribution in the FRM. Since the ion temperature is 120 keV for both cases, this corresponds to varying the stability factor.

In summary then, the SAFFIRE plasmas do not appear to have the potential for exhibiting anomalous fp slowing, unless the fp distributions are anisotropic. Almost all the alphas are absolutely confined in the FRM geometry; therefore their distribution is expected to be isotropic and anomalous alpha slowing is not expected. Prompt proton losses may, however, give rise to an anisotropic superthermal proton distribution in the FRM. The incorporation of velocity component information into the proton studies is thus necessary before final conclusions concerning the resistance of the protons to anomalous effects can be drawn.

CHAPTER 6

CONCLUSIONS AND RECOMMENDATIONS FOR FUTURE WORK

The two main objectives of this work were earlier cited as: The development of a more consistent model of the FRM plasma; and to provide an accurate calculation of the effect of fusion products on the FRM. To achieve these two objectives, two new computer models were developed. The first is a zero-dimensional, two fluid (ion and electron) plasma burn code (FRMOD), while the second is a Monte Carlo particle code (MCFRM). Together, these two codes have allowed both objectives to be achieved. Not only has the behavior of fps in the FRM been calculated throughout their slowing down, but the development of a unique method of coupling the results of the Monte Carlo calculation with the 0-D model (discussed in Section 4.4) has allowed fp heating and ash buildup to be included in the evaluation of the steady-state plasma parameters over a wide range of parameters. Finally, because the Monte Carlo solution technique provides a wealth of detailed information about fps in the steady-state FRM, fp energy distributions have also been calculated.

A brief summary of the unique features of the present analysis and some of the characteristics of the FRM system which have, for the first time, been identified includes:

1. The application of a Monte Carlo treatment of Coulomb scattering to fp motion in the FRM; thus allowing both fp energy and particle deposition to be evaluated.

2. The use of a modified Hill's vortex model of the FRM equilibrium (that allows for possible elongation) which not only provides a straightforward means of coupling the results of the Monte Carlo calculation into the plasma burn code, but also provides an improved basis for reducing the three-dimensional balance equations for particles and energy to zero-dimensional form.

3. The subsequent identification of a significiant amount of fp heating and ash buildup in the FRM plasma (a result which was not previously expected due to the small size of the FRM).

4. A simplified means of expressing the absolute and closed-field confinement limits for fps in the FRM; which allows these limits to be determined for any charged fp in any FRM plasma by specifying only the vacuum field strength and the plasma size.

5. A corresponding means of correlating the MCFRM results for the actual fp energy and particle deposition in the closed field region of the FRM over a wide range of system parameters.

6. A model of heat conduction losses to the cold, flowing plasma on the open field lines that assumes the development of a low density "boundary layer" which helps to "insulate" the closed field region.

7. A calculation of fp energy distributions in the steady-state FRM, and a discussion of their trends.

As the above list indicates, many advances in the understanding of the FRM have resulted from the present study, and, as a result, a detailed investigation into the potential of the FRM as an advanced-fuel fusion reactor concept (SAFFIRE) was made. The SAFFIRE concept was found to be both attractive and flexible; offering a small-sized (50-100MW) supplement to tokamaks and tandem mirrors. Utilizing the low

activation D-^{3}He or the fuel self-sufficient Cat-D fuel cycles, the SAFFIRE reactors are especially well suited for specialized applications (such as synfuel production or localized "peaking" units).

As is often the case in a study of this type, however, new questions and opportunties for additional work have been identified. The following recommendations are therefore included to serve as an impetus for supplemental investigations.

1. The incorporation of electric fields into the Monte Carlo calculation. These fields will affect fp motion at lower energies thus altering the ash buildup fractions predicted by the present analysis. The magnitude of the fields could be estimated by calculating the prompt fp losses as a function of the magnetic flux coordinate and using this information to evaluate the space charge buildup.

2. The incorporation of large angle nuclear elastic scattering into the collision model. This effect could have a significant influence on the distribution of the high energy protons and can be included in a straightforward manner due to the Monte Carlo nature of the model.

3. An investigation into the diffusion rate of background particles in the FRM. Assuming that the actual background density profile is adequately described by the Hill's vortex model, a first order estimate of the spatially dependent (1-D) diffusion coefficient could be obtained by starting a group of test particles on a grid that was consistent with the vortex density profile. The known density gradient together with the initial rate at which particles were displaced spatially would allow an estimate of $D(\psi)$ to be found. This would have the advantage of including finite orbit effects.

4. A calculation of fp induced currents in the FRM. This would involve a straightforward extension of the technique used to calculate the steady-state fp energy distribution. The energy distribution would simply need to be broken down into its parallel and perpendicular components, weighted by v_θ, and integrated to give the total fp current. Current density profiles could also be obtained by breaking the spatial integration into groups.

5. The field model could be made more general by representing it on a grid structure, as opposed to the present Hill's vortex description, and including quadrupole effects.

6. An investigation into whether or not the superthermal fp distributions are anisotropic, and, if so, what effects this has on the overall fp energy and particle deposition.

This list is, of course, not an exhaustive one and, due to the wealth of detailed information generated by the Monte Carlo treatment seems to be limited only by the creativity of the individual user. The author, therefore, encourages the reader to consider other possible adaptations as well; especially since the groundwork laid here is thought to have potential applications in many areas.

In conclusion, then, two valuable new tools for investigating the potential of small field-reversed systems have been developed. The models have been thoroughly tested and applied extensively in the development of the SAFFIRE reactor concept at Illinois. They have subsequently led to the identification of several unique aspects of the FRM, both from an engineering and from a physics standpoint; however these results are thought to be only the "tip of the iceberg". With the growing interest in reversed-field geometries (due to their inherent small size and resulting possibility of "near term" development) opportunities for related applications of the present work are being identified at an increasingly rapid pace. The hope is, therefore, that the present methods are not laid aside, but used to form the basis for additional studies which will one day lead to the commercial use of fusion energy.

REFERENCES

1. G. M. Swift and F. H. Southworth, "Bundle Divertor Designs for the ILB Advanced Fuel Tokamaks," Proc. Seventh Symposium on Engineering Problems of Fusion Research, Vol. II, 1198 (1977).

2. T. K. Fowler and B. G. Logan, "The Tandem Mirror Reactor," Comments on Plasma Physics and Controlled Fusion Research, 2, 167 (1977).

3. W. C. Condit, T. K. Fowler, and R. F. Post, Status Report on Mirror Alternatives, UCRL-52008, Lawrence Livermore Laboratory, Livermore, CA (1976).

4. N. Christofilos, Proc. II United Nations International Conference on the Peaceful Uses of Atomic Energy, 32, 279 (1958).

5. J. R. McNally, Jr., ORNL-3392, 89, Oak Ridge National Laboratory, Oak Ridge, TN (1963).

6. J. R. McNally, Jr., "Simplified Approach to Attaining a Proton E-layer," ORNL-TM-4965 (1975).

7. N. C. Christofilos, "Astron Plasma Parameters Confined in the Closed Magnetic Well of a Proton E-layer," Proceedings of the Nuclear Fusion Reactors Conf. Culham, England, 173 (1969).

8. D. V. Anderson, et al., "Theoretical Study of E-layer and Plasma Behavior in Astron," Proceedings of the Fourth International Conference on Plasma Physics, Madison, WI, Vol. I, 137 (1971).

9. N. C. Christofilos, et al., "Trapping Experiments in the Astron," Proceedings of the Fourth International Conference on Plasma Physics Madison, Wisc., Vol. 1, 119, (1971).

10. H. H. Fleischman, et al., Phys. Rev. Letters, 27, 1428 (1971) and 29, 256 (1972).

11. D. A. Hammer, et al., Physics Letters, 60A, 31 (1977).

12. R. K. Linford, W. T. Armstrong, D. A. Platts, and E. G. Sherwood, "Field Reversal Experiments (FRX) in Theta Pinches," Bult. APS, 23, (1978).

13. A. G. Es'kov, R. Kh. Kurtmullaev, et al., "Features of Plasma Heating and Confinement in a Compact Toroidal Configuration," 7th IAEA Conference on Plasma Physics and Controlled Thermonuclear Research, Innsbruck (1978). In print.

14. A. Eberhagen and W. Grossman, "Theta pinch Experiments with Trapped Antiparallel Magnetic Fields," Z. Physik 248, 130-149 (1971).

15. J. A. Byers, Phys. Rev. Letters, 39, 1476 (1977).

16. L. D. Pearlstein and J. P. Friedberg, Phys. Fluids 21, 1218 (1978).

17. Edward Clemens Morse, Ph.D. Thesis, Nuclear Engineering, University of Illinois, Urbana, IL, 1979.

18. R. N. Sudan and M. N. Rosenbluth, Phys. Rev. Letters 36, 972 (1976).

19. R. V. Lovelace, Phys. Fluids 19, 723 (1976).

20. J. M. Finn and L. Sparks, "Equilibria of Field-Reversed Ion Rings," LPS230, Laboratory of Plasma Studies, Cornell Univ. (1977).

21. W. C. Condit, et al., "The Field-Reversed Mirror as a Power Reactor," Proc. 2nd Topical Meeting on the Technology of Controlled Nuclear Fusion, USERDA-CONF-760935-PI, Vol. 1 , 107 (1976).

22. G. A. Carlson, et al., "Conceptual Design of the Field-Reversed Mirror Reactor," UCRL-52467, Lawrence Livermore Laboratory (1978).

23. A. C. Smith, Jr., et al., "Preliminary Conceptual Design of the Moving Ring Field-Reversed Mirror Reactor," Pacific Gas and Electric Company Report 78FUS-1 (1978).

24. M. J. M. Hill, "On a Spherical Vortex," Phil. Trans. Royal Soc. (A), Part 1, 214, (1894).

25. D. Driemeyer, G. H. Miley, and W. C. Condit, "A Monte Carlo Method for Calculating Fusion Product Behavior in Field-Reversed Mirrors," ANS Topical Meeting Computational Methods in Nuclear Engineering, Vol. 2, 7-37 (1979).

26. D. E. Post, P. H. Rutherford, H. P. Furth, R. R. Smith, "Calculation of Neutral Beam Heating of Tokamaks," Second European Conference on Computational Physics, Garching, Germany, April 1976.

27. E. C. Morse, "High Beta, Low Aspect Ratio Plasmas," in ERDA-COO-2218-41, (G. H. Miley, ed.), Univ. of Illinois, Urbana, IL (1976).

28. M. Y. Wang and G. H. Miley, Nuclear Fusion, 19, 1 (1979).

29. V. D. Shavranov, Sov. Phys. - JETP 6, 545 (1958).

30. V. D. Shafranov, Sov. Phys. - JETP 10, 775 (1960).

31. A. Garren, et al., Proc. II United Nations International Conference on the Peaceful Uses of Atomic Energy, 31, 65 (1958).

32. C. L. Longmire, D. E. Nagle, and F. L. Ribe, Phys. Rev. 114, 1187 (1959).

33. J. M. Dawson, H. Okuda, B. Rosen, "Collective Transport in Plasmas," Methods in Computational Physics, 16, 282 (1976).

34. D. V. Sivukhin, Reviews of Plasma Physics, (Edited by M. A. Lentovich, Consultants Bureau, NY), Vol. 4, 93 (1966).

35. L. Spitzer, Jr., Physics of Fully Ionized Gases, Ch. 5, 129, Interscience, New York, NY (1962).

36. B. A. Trubnikov, Reviews of Plasma Physics, (Edited by M. A. Lentovich, Consultants Bureau, NY), Vol. 1, 105 (1965).

37. "FOKN: A Relativistic Fokker-Planck Code with Large Angle Scattering and Radiation Losses," Lawrence Livermore Laboratory Report, UCID-17196 (1976).

38. C. L. Longmire and M. N. Rosenbluth, Phys. Rev. 103, 507 (1956).

39. J. G. Cordey and M. J. Houghton, Nuclear Fusion 13, 215 (1973).

40. J. G. Gilligan, et al., "Divertor Design for the D-^{3}He Field-Reversed Mirror," Proc. Third ANS Topical Mtg. on Fusion, Sante Fe, NM (1978).

41. D. E. Baldwin and M. Rensink, "Electron Effects in Ion-Current Field Reversal," Lawrence Livermore Laboratory, Rept. UCRL-80912 (1978).

42. D. R. Gibson, "Neutral Beam Fueling Requirements for a Steady-State Field-Reversed Mirror," M.S. Thesis, University of Illinois (1979).

43. J. C. DeVeaux, "A Study of the Pellet Fueling of Field Reversed Mirrors," M.S. Thesis, University of Illinois (1979).

44. R. W. Conn and J. Kesner, Nuclear Fusion 15, 775 (1975).

45. G. H. Miley, Fusion Energy Conversion, American Nuclear Society, Hinsdale, Illinois, 1976.

46. R. A. Krajcik, Nuclear Fusion 13, 7 (1973).

47. R. L. Freeman and E. M. Jones, "Atomic Collision Processes in Plasma Physics Experiments," UKAEA Research Group, Culham Laboratory, SBN:85311-027-1 (1974).

48. J. G. Gilligan, "An Approach to Advanced Fuel Fusion Economics," University of Illinois, Internal Report, April 1979.

49. D. Driemeyer, J. Gilligan, G. Miley, T. Blue and C. Baker, "A Cat-D Version of SAFFIRE--Potential and Problems," Eighth Symposium on Engineering Problems of Fusion, Research, November 13-16, 1979, San Francisco, CA.

50. D. J. Sigmar and M. C. Chan, "Anomalous Alpha Particle Transport in Thermonuclear Tokamak Plasma," ORNL/TM-6027 (1977).

51. D. Driemeyer, M. Ohnishi, and G. H. Miley, "Studies of Fusion Product Energy Distributions in Field-Reversed Mirrors," Trans. Am. Nuc. Soc., San Francisco, CA, Nov. 11-16, 1979.

52. M. N. Rosenbluth, W. MacDonald, and D. Judd, Phys. Rev., 107, 1 (1957).

APPENDIX A

FRMOD User's Guide

The zero-dimensional FRM plasma burn code, FRMOD, described in this work is written in the FORTRAN language and is currently available on the Control Data Corporation (CDC) 7600 computer at the Magnetic Fusion Energy Computer Center (MFECC), sponsered by the U. S. Department of Energy, in Livermore, CA. This guide will assume that the user is familiar with the system architecture and some of the utility programs available on the MFE-7600 machine, since online documentation is available for system routines through the use of the DOCUMENT utility. Users may therefore refer to it for answers to system related questions.

The files associated with the FRMOD code are available through the FILEM utility, using the command:

FILEM .RDS 1345 .DRIEM <list> / t v,

where <list> is a string of file names chosen from Table A1, t is the user allocated time limit, and v is the priority value. For execution of the already compiled version of FRMOD, XFRMOD, the following command would then be issued:

XFRMOD D=data,H=output / t v.

Here the data and output files (see Tables A3 and A5 for examples) may have any name except NEWDAT, which is a temporary scratch file used for outputting the converged values of the five dependant variables for each case (see Table A6). These values can thus be copied into new data

files and used as an initial guess for additional parametric calculations involving related FRM plasmas. A value of t equal to one should normally be sufficient for completing a series of parametric studies; however the code can be restarted by typing:

+XFRMOD? / t v,

where ? is a letter corresponding to the channel being used, if the initial time allocation runs out.

The program is currently set up to be run in an interactive mode with periodic action required of the user if the code is having problems converging. When such action is needed the code will prompt the user at the terminal. This interaction feature was included because the set of algebraic equations describing the steady-state plasma parameters is highly non-linear, and numerical convergence is consequently difficult in some cases. Thus, when a solution has not converged after some maximum number of iterations (typically 100) control returns to the user and a revised guess for the five dependant parameters may be entered. (Continuation using the existing values of the parameters is also possible if zeroes are entered for the new guess.) Control also returns to the user if the solver begins to search for a solution where the values of the dependant parameters are no longer physical (i.e., negative), and a revised guess should always be entered in that case.

To illustrate the use of the FRMOD code, a typical data file, and the first portion of its corresponding output file are given in Tables A3 and A5. They are for an elongated D-^{3}He study vs the stability factor, S. As Table A3 indicates, the input to the code is

specified in NAMELIST format; except for the initial guess for the five dependant variables, which may be entered in a free format style (where the values are terminated by commas) when the guess is typed in from the terminal, or in a fixed G10.0 format mode when the guess is specified as part of the data file. The output file can then be examined by disposing it, using the ALLOUT or NETOUT utilities, or by printing it at the terminal, using the TRIX AC editor, if it is short. Because the input is in NAMELIST format extremely compact data files are normally possible. The user does, however, have the freedom to specify otner values for many parameters; thus a summary of all user specifiable variables, and their default values, is given in Table A2. Similarly, because the code represents a large amount of information symbolically in its output summary, a key to the output file is also included in Table A4.

Finally, for those individuals who are interested in a bit more detail, a brief flow chart for the FRMOD code is provided in Fig. A1. This should aid in locating general sections of the code; however specific questions regarding more subtle modifications should be referred to the author. In any case, when changes are made in the FRMOD code the new FORTRAN source file must be recompiled and loaded along with the FORTLIB libraries. The command for this process is:

```
CHATR I=FRMOD,L=0,LIB=(F') / t v,
```

and the new version of XFRMOD can then be executed in the above manner.

TABLE A1

Files Associated with the FRMOD Code.

File Name	Type	Remarks
FRMOD	F	FORTRAN source for the FRMOD code.
XFRMOD	B	Compiled version of the FRMOD code.
DATHE1	D	Data file for a study of reference D-^{3}He plasmas with no heat conduction losses.
DATHE2	D	Data file for a study of reference, spherical D-^{3}He plasmas with heat conduction losses.
DATHE3	D	Data file for a study of elongated D-^{3}He plasmas.
DATHE4	D	Data file for a study of spherical D-^{3}He plasmas with different magnetic field strengths.
DATHE5	D	Data file for a study of spherical D-^{3}He plasmas with anomalous diffusion losses.
DATCD2	D	Data file for a study of spherical Cat-D plasmas.
DATCD3	D	Data file for a study of elongated Cat-D plasmas.
DATDT2	D	Data file for a study of spherical D-T plasmas.
DATDT5	D	Data file for a study of spherical D-T plasmas with anomalous diffusion losses.

TABLE A2

Input Variables for the FRMOD Code

Block	Variable Name	Default Value	Remarks
IN1	N	5	The number of dependant variables.
IN1	ITMAX	100	The maximum number of iterations used by QNWT before control returns to the user.
IN1	FPRNT	20	The number of iterations between intermediate printouts by QNWT.
IN1	EPS	10	Convergence criterion for QNWT.
IN1	IPRNT	1	Detailed printout occurs every IPRNT-th iteration.
IN2	ZKAP	1	The plasma elongation factor, κ.
IN2	IDIF	1	The diffusion coefficient control: 0 -> Classical diffusion. 1 -> For near-classical diffusion. 2 -> Anomalous diffusion.
IN2	ICD	0	The Cat-D system flag: 0 -> Fixed fuel fractions. 1 -> Cat-D fueled system.
IN2	RHO	9.7E-7	The resistivity of the first wall (Ω-m), used in calculating the cyclotron losses.

Block	Variable Name	Default Value	Remarks
IN2	FH	0.1	The hole fraction of the first wall, used in calculating the cyclotron losses.
IN2	EC	1.0	The extraneous cyclotron loss factor.
IN2	GAMED	0.8	The correction for the electron drag reduction in the circulating current.
IN3	FB(1)	0.5	Fraction of the fuel that is deuterium.
	FB(2)	0.0	Fraction of the fuel that is tritium.
	FB(3)	0.5	Fraction of the fuel that is helium-3.
Note: For Cat-D systems, these fractions are chosen by the code.			
IN3	C3	0.7	The sensitivity parameter for attempting to converge on an improved initial guess.
IN3	ETATH	0.4	The thermal conversion efficiency.
IN3	ETADC	0.6	The direct conversion efficiency.
IN3	ETAI	0.8	The beam injection efficiency.
IN3	ETAIC	0.8	The ion cyclotron coupling efficiency.
IN3	DIST	500.0	The distance from the beam source to the plasma (cm).
IN3	TANY	.017452	The tangent of the beam divergence angle in the y-direction.
IN3	TANZ	.017452	The tangent of the beam divergence angle in the z-direction.
IN3	BBETA	$\pi/8$	The beam orientation angle relative to the coordinate frame used to describe the background plasma.

Block	Variable Name	Default Value	Remarks
IN3	BMAX	10.0	The cutoff value for the beam shaping factor.
IN3	NBI	20	The number of grid divisions used to integrate the beam trapping.
IN4	EAV(1)	650.0	The average energy (in keV) of the six
	EAV(2)	750.0	fps found in a deuterium fueled system.
	EAV(3)	1600.0	Namely, the ^{3}He, T, and p produced by
	EAV(4)	2000.0	D-D fusion; the α produced by D-T
	EAV(5)	2100.0	fusion; and the α and p produced by
	EAV(6)	5500.0	D-^{3}He fusion.
Note: The next four values are used in calculating the fraction of the marginally confined fps and their energy that is deposited in the closed field region.			
IN4	AE	-0.42887	The slope of the correlation line for energy deposition.
IN4	BE	0.25044	The intercept of the correlation line for energy deposition.
IN4	AP	-0.35011	The slope of the correlation line for particle deposition.
IN4	BP	0.34500	The intercept of the correlation line for particle deposition.

Block	Variable Name	Default Value	Remarks
IN4	TC	0.05	The temperature of the plasma on the open field lines (keV).
IN4	XNC	0.02	The density of the plasma on the open field lines ($x10^{15}cm^{-3}$).
IN4	TBL	1.0	The temperature of the boundary layer region (keV).
IN4	GAMW	1.0	The thickness of the boundary layer in units of the average ion gyroradius in the vacuum magnetic field. If GAMW=0, there are no heat conduction losses.
IN4	IFED	0	Control over the fp energy and particle deposition: 0 -> FRMOD approximation is used. 1 -> No fp heating or ash buildup. 2 -> Closed-field confinement limit. 3 -> Absolute confinement limit. 4 -> Input values are used.
IN5	E(k,j)	24*0.0	The energy of the k-th energy group of the j-th injected species (keV). The first group is a temperature, not an energy, and the species are: 1 -> Electrons. 2 -> Deuterium.

Block	Variable Name	Default Value	Remarks
			3 -> Tritium.
			4 -> Helium-3.
			5 -> Alphas.
			6 -> Protons.
IN5	EINC(j)	6*0.0	The beam energy increment between cases for the j-th injected species (kev).
IN5	TINC	20.0	The ion temperature increment between cases (keV).
IN5	XNG	1.0E+8	The density of cold neutrals at the surface of the closed field region (cm^{-3}).
IN5	S	10.0	The plasma stability factor.
IN5	B0	60.0	The vacuum magnetic field strengtn (kG).
IN5	GAMC	1.0	A factor used to destroy the confinement in order to study the effects of enhanced diffusion.
IN5	FRE	6*0.0	The fraction of the six charged fps' energy retained in the closed field region. Normally, these fractions are found using the correlations.
IN5	FRP	6*0.0	The fraction of the six charged fps deposited in the closed field region. Normally, these fractions are also found using the correlations.

Block	Variable Name	Default Value	Remarks
IN5	NPT	3	The number of different background temperatures calculated for each set of input parameters. If only beam heating is used this value corresponds to the number of different injection energies for each set of parameters.
IN5	IDAT	1	The control over whether the input is from disk or from the terminal.
IN5	NG	2	The number of energy groups. This number should be increased if the beam power is large.
	ICMAX	none	Chosen when inputting an initial guess for the five dependant variables. If ICMAX>1, this number of iterations is used in an attempt to improve the initial guess and enhance the probability of finding a solution. (If this value is set larger than one a large amount of intermediate output is generated at the terminal. Also, ICMAX=5 should be sufficient to allow a reasonable guess to be evaluated.

Block	Variable Name	Default Value	Remarks
	X(1)	none	Initial guess for either the background ion temperature (keV), if X(1)>1, or the relative ICRH input, if X(1)<1. For the first case the ICRH input is zero, neutral beams are the only energy input to the plasma, and the ion temperature thus becomes a dependant variable. When X(1)<1, however, the ion temperature is fixed, and the ICRH input becomes a dependant variable.
	X(2)	none	Initial guess for the temperature of the background electrons (keV).
	X(3)	none	Initial guess for the peak density of the background ions ($x10^{15}cm^{-3}$).
	X(4)	none	Initial guess for the ratio of the electron to ion density.
	X(5)	none	Initial guess for the fraction of the background that is fuel.

TABLE A3

Sample Data File for a Spherical D-^{3}He Plasma Study

```
 $ IN1
 $ IN2
 $ IN3
 XNC=0.005 GAMW=1.0 $ IN4
 E(1,2)=60.0 E(1,3)=60.0 E(1,4)=60.0 E(1,5)=60.0 E(1,6)=60.0
 E(3,3)=750.0 E(3,4)=650.0 E(3,5)=2100.0 E(3,6)=5500.0
 E(2,2)=10.0 E(2,4)=10.0 S=10.0 NRT=3 IDAT=1 $ IN5
1.3099E-04 56.90      6.382      1.503      0.9815
5.9994E-05 75.51      4.597      1.507      0.8383
9.7782E-05 88.87      3.766      1.512      0.7630
 S=15.0 NRT=1 $ IN5
 48.24      47.97      7.830      1.503      0.8906
 S=0.0 $ IN5
 $ IN1
 $ IN2
 $ IN3
 XNC=0.02 $ IN4
 E(1,2)=100.0 E(1,3)=100.0 E(1,4)=100.0 E(1,5)=100.0 E(1,6)=100.0
 E(3,3)=750.0 E(3,4)=650.0 E(3,5)=2100.0 E(3,6)=5500.0
 E(2,2)=10.0 E(2,4)=10.0 S=5.0 NRT=4 IDAT=1 $ IN5
1.7430E-03 67.67      4.789      1.500      0.9761
1.8593E-03 77.96      3.989      1.500      0.9640
2.0064E-03 86.51      3.488      1.501      0.9508
2.1787E-03 93.35      3.138      1.501      0.9383
 E(1,2)=60.0 E(1,3)=60.0 E(1,4)=60.0 E(1,5)=60.0 E(1,6)=60.0
 S=10.0 NRT=3 $ IN5
3.2873E-04 54.70      6.600      1.502      0.9382
2.9904E-04 78.21      4.854      1.506      0.8683
3.6158E-04 85.50      3.961      1.511      0.7998
 E(1,2)=40.0 E(1,3)=40.0 E(1,4)=40.0 E(1,5)=40.0 E(1,6)=40.0
 S=15.0 $ IN5
1.5418E-04 38.11      9.926      1.501      0.9506
2.9425E-05 59.40      6.801      1.506      0.8283
5.0084E-05 76.60      4.669      1.512      0.7083
 S=-1 $ IN5
```

TABLE A4

Definition of Symbols Found in the Output File

Symbol	Meaning
TI	Ion temperature (keV).
TE	Electron temperature (keV).
P/AV	Peak to average temperature.
XNBO	Peak background ion density (cm^{-3}).
XNEO	Peak background electron density (cm^{-3}).
TAUPN	Particle confinement time for anomalous diffusion (sec).
TAUE	Energy confinement time (sec).
TAUPC	Particle confinement time for classical diffusion (sec).
GAMC	Anomalous loss factor.
PHIO	Neutron flux at the plasma surface (#/cm^2/sec).
RHV	The spherical vortex radius (cm).
RHO	The average ion gyroradius in the vacuum field (cm).
IDIF	The type of diffusion for this case:
	0 -> Classical.
	1 -> Near-classical.
	2 -> Anomalous.
PMAG	The magnetic pressure.
PPLAS	The plasma kinetic pressure.
BETA	The plasma beta value.
IR-MA	The plasma current required to maintain the equilibrium.
ID-MA	The diamagnetic plasma current contribution.

Symbol	Meaning
II-MA	The injected plasma current contribution.
F-E	The ratio of the electron to the ion density.
F-D	The fractional density of thermal deuterium.
F-T	The fractional density of thermal tritium.
F-He	The fractional density of thermal helium-3.
F-AL	The fractional density of thermal alphas.
F-PR	The fractional density of thermal protons.
FAI	Fraction of the ion input power from injected beams.
FCFI	Fraction of the ion input power from charged fps.
FIC	Fraction of the ion input power from ICRH.
FLI	Fraction of the ion power losses in leakage.
FIE	Fraction of the ion power losses to the electrons.
FHC	Fraction of the ion power losses in heat conduction.
FAE	Fraction of the electron input power from NB injection.
FCFE	Fraction of the electron input power from charged fps.
FIE	Fraction of the electron input power from the ions.
FLE	Fraction of the electron power losses in leakage.
FBR	Fraction of the electron power losses in bremsstrahlung radiation.
FCY	Fraction of the electron power losses in cyclotron radiation.
AKCY	Fraction of the cyclotron radiation absorbed by the first wall.

Symbol	Meaning
RHO	The resistivity of the first wall (Ω-m).
FH	Fraction of the first wall that is holes.
FI	Fraction of the charged fusion power that is given to the ions.
FE	Fraction of the charged fusion power that is given to the electrons.
FL	The fraction of the charged fusion power that is not deposited in the closed field region.
FRDDH	Fraction of the 820-keV, D-D, ^{3}He's energy retained in the closed field region.
FRDDT	Fraction of the 1010-keV, D-D, T's energy retained in the closed field region.
FRDDP	Fraction of the 3020-keV, D-D, p's energy retained in the closed field region.
FRDTA	Fraction of the 3520-keV, D-T, α's energy retained in the closed field region.
FRDHA	Fraction of the 3670-kev, D-^{3}He, α's energy retained in the closed field region.
FRDHP	Fraction of the 14680-keV, D-^{3}He, p's energy retained in the closed field region.
FHC	Fraction of the total plasma output power in heat conduction losses.

Symbol	Meaning
FBR	Fraction of the total plasma output power in bremsstrahlung radiation losses.
FCY	Fraction of the total plasma output power in cyclotron radiation losses.
FLP	Fraction of the total plasma output power in particle leakage losses.
FCF	Fraction of the total plasma output power in charged fp losses.
FNF	Fraction of the total plasma output power in neutrons.
PI-MW	The total injection power (MW).
PF-MW	The total fusion power (MW).
QVAL	The energy multiplication factor.
PN-MW	The net electrical power output (MW).
ETAI	The neutral beam injection effiency.
FVAL	The ratio of total to background fusion power.
ETATH	The thermal conversion efficiency.
ETADC	The direct conversion efficiency.
ETAIC	The ion cyclotron heating efficiency.
E0-D,T,H	The beam injection energy for each species (keV).
IBD,T,H-A	The beam injection current for each species (amps).
PI-D,T,H	The beam power for each injected species (MW).
TAUF	The average fusion time for each species (sec).
SGVEI	Electron ionization rate for each species (cm^3/sec).

Symbol	Meaning
SGVPI	Proton ionization rate for each species (cm^3/sec).
SGVCX	Charge exchange rate for each species (cm^3/sec).
AT	The beam attenuation for each injected species.
TBL	Boundary layer temperature (keV).
XNBL	Boundary layer density (cm^{-3}).
KPRP	Cross field thermal conductivity in the boundary layer (ergs/keV/cm).
GAMW	Thickness of the boundary layer in units of the hot ion gyroradius.
XO-CM	Thickness of the boundary layer (cm).
SAREA	The surface area of the plasma (cm^2).

TABLE A5

Output Summary Corresponding to the First Case Generated

by the Data File Shown in Table A3

```
NEW CASE WITH FIELD OF   60.0 KG, VOLUME OF  27.09 LITRE,
ELONGATION OF    1.0  AND STABILITY FACTOR OF   10.0

TI    =  60.000        TE    =  56.903        R/AW  =  1.0000
XNB0  = 6.32831E+15    XNE0  = 9.49989E+15    R/AW  =  8.7500
TAURN = 0.16982        TAUE  =  1.7374        TAURC =  7.8979
GAMC  =  1.0000        TAUP  =  3.8443        RHI0  = 2.02845E+12
RHW   =  18.630        RHO   = 0.62101        IDIF  =  1.0000
RMAG  =  1005.8        RPLAS =  1005.8        BETA  =  1.2857
IR-MA =  4.4477        ID-MA =  4.7808        II-MA =  0.
F-E   =  1.5086        F-D   = 0.46074        F-T   = 1.18046E-03
F-HE  = 0.46074        F-AL  = 4.08900E-02    F-BR  = 3.32597E-02

ION ENERGY FLOW, FRACTION OF 0.25748      MW

FAI   = 3.32198E-02    FCFI  = 0.41598        FIC   = 0.55080
FLI   =-0.49597        FIE   =-0.36564        FHC   =-0.13488

ELECTRON ENERGY FLOW, FRACTION OF 0.48200      MW

FAE   = 0.             FCFE  = 0.80468        FIE   = 0.19532
FLE   =-0.38386        FBR   =-0.56818        FCY   =-4.79582E-02
AKCY  = 1.16872E-02    RHO   = 9.70000E-07    FH    = 0.10000

CHARGED FUSION ENERGY FLOW, FRACTION OF  1.0020      MW

FI    = 0.10689        FE    = 0.38707        FL    = 0.50605
FRDDH = 0.95760        FRDDT = 0.59006        FRDDR = 0.76198
FRDTA = 0.60159        FRDHA = 0.59138        FRDHR = 0.46208

OUTPUT ENERGY FLOW, FRACTION OF  1.1846      MW

FHC   = 2.93168E-02    FBR   = 0.23118        FCY   = 1.95133E-02
FLP   = 0.26398        FCP   = 0.42805        FNP   = 2.71060E-02
```

OVERALL ENERGY FLOWS AND EFFICIENCIES

PI-MW = 0.15048	PE-MW = 1.0341	QVAL = 6.8724
PN-MW = 0.44971	ETAI = 0.80000	FVAL = 1.0000
ETATH = 0.40000	ETADC = 0.60000	ETAIC = 0.80000

BEAM INJECTION AND TRAPPING INFORMATION

E0-D = 10.000	E0-T = 0.	E0-HE = 10.000
IBD-A = 0.44849	IBT-A = 0.	IBH-A = 0.84666
PI-D = 4.424935E-03	PI-T = 0.	PI-HE = 4.833888E-03
TAUE = 80.888	TAUE = 8.3669	TAUE = 27.145
SGVEI = 7.37795E-09	SGVEI = 0.	SGVEI = 1.55581E-08
SGVPI = 1.91789E-08	SGVPI = 0.	SGVPI = 9.49032E-09
SGVCX = 3.04120E-08	SGVCX = 0.	SGVCX = 1.25468E-08
AT-D = 0.98863	AT-T = 0.	AT-HE = 0.98712

A 50.0 EV, 5.0E+12 CM-3 COLD PLASMA GIVES 1.0E+08 CM-3 NEUTRALS

TBL = 1.0000	XNBL = 3.87300E+14	KPRP = 9.34131E-08
GAMW = 1.0000	XO-CM = 0.62101	SAREA = 4361.6

TABLE A6

Scratch File NEWDAT Resulting From the Data File

Shown in Table A3

```
 $IN5
1.3099E-04 56.90      6.328      1.503      0.9215
5.9998E-05 75.51      4.597      1.507      0.8383
9.7772E-05 88.87      3.766      1.512      0.7630
 $IN5
 48.24      47.97      7.830      1.503      0.8906
 $IN5
1.7430E-03 67.67      4.720      1.500      0.9761
1.8598E-03 77.96      3.989      1.500      0.9640
2.0064E-03 86.51      3.488      1.501      0.9508
2.1787E-03 93.35      3.138      1.501      0.9383
 $IN5
3.2873E-04 54.70      6.600      1.502      0.9382
2.9904E-04 72.21      4.854      1.506      0.8683
3.6158E-04 85.50      3.961      1.511      0.7998
 $IN5
1.5418E-04 38.11      9.926      1.501      0.9506
2.9489E-05 59.40      6.201      1.506      0.8283
5.0081E-05 76.60      4.669      1.512      0.7083
```

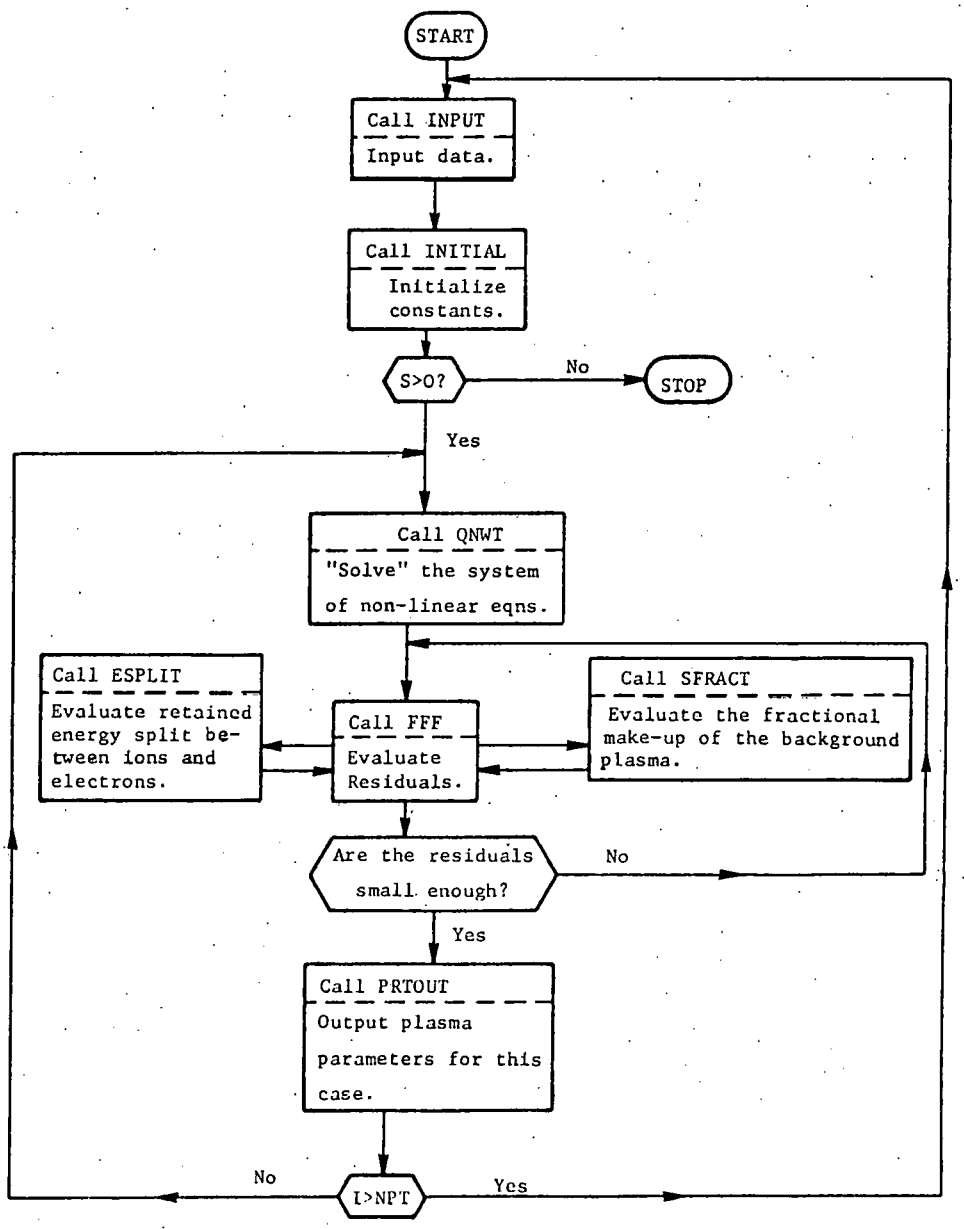

Figure A-1. FRMOD Flow Chart.

APPENDIX B

MCFRM User's Guide

The Monte Carlo particle code MCFRM, described in this work is also written in the FORTRAN language and is available on either the MFE-7600 or the CRAY-1 computers. The discussion presented here will, however, deal only with the steps required to execute the code on the CRAY, since the majority of its use should be on that machine. The file containing the source can be obtained through FILEM by using the command:

```
FILEM .RDS 1345 .DRIEM MCFRMD / t v.
```

Presently, the program requires precompilation because of the dual machine option; therefore, before sending the FORTRAN source to the CRAY, the following must be done:

```
TOCFT MCFRMD MCFRM / t v.
```

This converts the program to a format that is acceptable by the CRAY, and the result is in a file named MCFRM, which is now ready to be sent to the CRAY. The file is transferred using the command:

```
NETOUT C MCFRM / t v.
```

Once logging onto the CRAY the user is ready to compile and load the MCFRM code by issuing the command:

```
RCFT I=MCFRM,L=0,LIB=(F',T') / t v.
```

This writes the executable file, XMCFRM, which can subsequently be run by typing:

```
XMCFRM D=data,H=output, BOX=(Box & ID) / t v.
```

Here the data, and output files can have any names, and a value for the time allocation t can be estimated by using the fact that the code runs at ~50μs per particle per timestep; thus following 1000 particles through 1000 timesteps requires ~50 seconds of execution time. The code can, however, be restarted by typing:

+XMCFRM? / t v,

where ? is a letter corresponding to the channel being used, should the initial time allocation run out.

Upon completion, two output files will have been generated. The first (whose name was specified on the execute line) contains printed output, and the second is a grapnics file beginning with the letter F. This file contains plots of the instantaneous particle distribution vs r, and the distribution vs P_θ, during slow down. It also contains a brief summary of the printed output along with a plot of one particle's trajectory. This graphics file can either be given to the operating system (wnich produces output in the form of microfiche) or plotted at a remote site by using the NETPLOT utility. The first option is selected by typing:

GIVE ALWITH. F 999999 END / t v,

while the second option is implemented by typing:

NETOUT <site> ALWITH. F F. L. D. BOX & ID / t v.

In the latter case, <site> is the code identifying the remote destination, and the D. option can be omitted if the user wishes to keep a copy of the graphics file on disk.

To illustrate the use of the MCFRM code, a typical data file and a condensed version of the corresponding output file are given in Tables B2 and B4. As Table B2 indicates, the input to the code is specified in NAMELIST format, and therefore a complete listing of the input variables is provided in Table B1. In addition, to aid in interpreting the printed output of Table B4, a summary of the output symbols is also provided in Table B3. Finally, for those individuals who are interested in the details of the code, a brief flow chart is provided in Fig. B1. This should help in locating general sections of coding; however specific questions should be referred to the author.

TABLE B1

Input Variables to the MCFRM Code

Block	Variable Name	Default Value	Remarks
TPART	RO	20*0.0	Selected by subroutine DISTRIB (if IFLAT is false) to represent the birth distribution of fps in the FRM.
TPART	UO	20*0.0	Note: The code assures that PARTO histories are followed in its initialization of particles.
TPART	CTHO	-1.0	Used to initialize particles in velocity space, if only one history is desired: CTH = 1.0 + CTHO
TPART	PHIO	0.0	PHI = PI + PHIO. Otherwise, the values of CTH and PHI are selected isotropically.
TPART	ET	Default values chosen from the value of IFP	Energy, mass, and charge of the test particles, corresponding to the following six cases by default: IFP = 1 --> 820-keV, D-D, ^{3}He. = 2 --> 1010-keV, D-D, T. = 3 --> 3020-kev, D-D, p. = 4 --> 3520-keV, D-T, α. = 5 --> 3670-keV, D-^{3}He, α. = 6 --> 14680-keV, D- He, p.
	AMT		
	ZT		

Block	Variable Name	Default Value	Remarks
			However, an alternate type of test particle can be specified by entering new values for ET(1), AMT(1), and ZT(1).
TPART	PTHETA	10.0	Used for making orbit studies where only one particle history is calculated. For these studies, IONE and IFLAT must be true; furthermore, NLCP must be false to see unconfined particles. (PTHETA is entered in units of $m\omega_o R_{HV}^2$.)
TPART	PARTO	1000	The number of particle histories that the code tries to assure are followed.
TPART	NPTH	20	The number of P_θ groups used in constructing the distribution plots vs P_θ during slow down.
TPART	NUMR	Chosen by DISTRIB	The number of radial starting positions, RO, in physical space.
TPART	NUMU	Chosen by DISTRIB	The number of starting angle cosines, UO, in physical space.
TPART	NUMTHET	Chosen isotrop'ly	The number of starting angle cosines, CTH, in velocity space.
TPART	NUMPHI	Chosen isotrop'ly	The number of starting azimuthal angles, PHI, in velocity space.

Block	Variable Name	Default Value	Remarks
BACK	RHV	20.0	Hill's vortex radius (cm).
BACK	BVAC	60.0	Vacuum magnetic field strengtn (kG).
BACK	TI1	100.0	Closed field ion temperature (keV).
BACK	TE1	90.0	Closed field electron temperature (keV).
BACK	T2	0.05	Open field temperature (keV).
BACK	DEN10	5.0E15	Peak closed field ion density (cm^{-3}).
BACK	DEN20	2.0E13	Open field ion density (cm^{-3}).
BACK	FFI	1.0	Used to "turn off" tne ion drag, while still including the electron drag.
BACK	DRGEN	1.0E04	variable drag enhancement factor.
BACK	AMI	2.6	Average ion mass (AMU).
BACK	AME	5.5e-4	Electron mass (AMU).
BACK	ZION	1.5	Average ion charge.
BACK	FCUTOFF	3.0	The multiple of the hot ion temperature corresponding to the cutoff energy.
BACK	CAPRTST	1.0	Used to allow for a vacuum layer between the open and closed field regions. Vacuum exists if CARPTST>1.
BACK	ZK	1.0	Plasma elongation factor, κ.
BACK	FRV	0.001	Maximum allowable change in the particle velocity during a timestep. FRV is used to determine DRGEN during the run.

Block	Variable Name	Default Value	Remarks
ONE	RMIN	0.0	Minimum radial boundary on orbit plots.
ONE	RMAX	1.6	Maximum radial boundary on orbit plots.
ONE	ZMIN	-1.6	Minimum axial boundary on orbit plots.
ONE	ZMAX	1.6	Maximum axial boundary on orbit plots.
ONE	ESCALE	0.0	The number of hot ion temperatures equal to the maximum energy on the energy distribution plots. The maximum energy on the plots will be chosen by the code if ESCALE=0.0.
ONE	NEPLT	20	The number of energy groups used.
ONE	NPDEL	1000	The number of timesteps between intermediate printouts.
ONE	NITPLT	9000	The maximum number of timesteps per orbit plot.
ONE	NDT	32	The number of timesteps per cyclotron period.
ONE	NITMAX	10	The maximum number of timesteps.
ONE	NRU	12	The number of radial bins used in constructing plasma heating profiles.
ONE	NZU	30	The number of axial bins used in construction plasma heating profiles.
ONE	NPLT	1	The particle history that is plotted.

Block	Variable Name	Default Value	Remarks
LGIC	NDRG	FALSE	Used to specify "no drag".
LGIC	NPAS	FALSE	Used to specify "no pitch-angle scattering or velocity diffusion."
LGIC	IFLAT	FALSE	Used to specify that a "test case" is being run where the background density is uniform.
LGIC	IONE	FALSE	Used to specify only one history, NPLT chooses which one.
LGIC	NLCP	TRUE	Used to include histories of particles that are not confined.
LGIC	IQUIT	FALSE	Used to run multiple cases.
LGIC	IGRID	FALSE	Used to indicate that the user is specifying the starting spatial grid. Values for the array RO and UO must subsequently be entered, if IGRID is true.

TABLE B2

Sample Data File for a Typical MCFRM Calculation

In This Case Six Consecutive Runs Were Made for

Each of the Six Standard Fusion Products.

```
IFP=1 $ IPART
TI1=60.0 TE1=56.9 DEN10=6.32E15
DEN20=5.0E12 RHV=18.6 $ BACK
NPLT=625 $ ONE
IQUIT=.F. $ LGIC
IFP=2 $ IPART
$ BACK
$ ONE
$ LGIC
IFP=3 $ IPART
$ BACK
$ ONE
$ LGIC
IFP=4 $ IPART
$ BACK
$ ONE
$ LGIC
IFP=5 $ IPART
$ BACK
$ ONE
$ LGIC
IFP=6 $ IPART
$ BACK
$ ONE
IQUIT=.T. $ LGIC
```

TABLE B3

Definition of Symbols Found in the Output File

Symbol	Meaning
NIT	Integer number of timesteps in units of $2\pi/NDT/\omega_o$ where $2\pi/\omega_o$ is the cyclotron period of the test particle in the vacuum field, and NDT is the number of timesteps that correspond to a cyclotron period.
NSTOP	The number of particle histories that have been terminated by NIT.
ETAV	The average energy of the remaining test particles in (keV).
FDRG	The average fractional change in the particles' velocity, due to drag, during the last timestep.
FPAS	The average fractional change in the particles' velocity, due to pitch-angle scattering and velocity diffusion during the last timestep.
DRGEN	The drag enhancement factor.
DVXSQ	The deviation in the particles position relative to the x-plane (in units of RHV^2).
DVRSQ	The deviation in the particles position relative to the cylindrical axis (in units of RHV^2).

Symbol	Meaning
BVAC	The vacuum magnetic field strength (kG).
RHV	The radius of the spherical vortex region (cm).
VTOT	The initial velocity of the test particles, in units of ($RHV \times NDT \times \omega_o / 2\pi$).
OMEG	The cyclotron frequency of the test particles in the vacuum field, ω_o, (sec^{-1}).
DELT	The lengtn of a timestep (sec).
NDT	The number of timesteps per cyclotron period.
TI-1	The ion temperature in the closed field region (keV).
TE-1	The electron temperature in the closed field region (keV).
DEN1	The average ion density in the closed field region (cm^{-3}).
T-2	The temperature in the open field region (keV).
DEN2	The ion density in the open field region (cm^{-3}).
RTST	The minimum radius where the cold plasma properties are used in the calculation (same as CAPRTST).
FION	The fraction of the retained fp energy that is given to the ions.
FELE	The fraction of the retained fp energy that is given to the electrons.
FAC	The fraction of the charged fps that are absolutely confined.
FHCF	Fraction of the charged fp energy that is deposited in the closed field region.

Symbol	Meaning
FHOF	Fraction of the charged fp energy that is deposited in the open field region.
FHLC	Fraction of the charged fp energy that is carried out of the system by unconfined fps.
PDCF	Fraction of the charged fps that are deposited in the closed field region.
PDOF	Fraction of the charged fps that are deposited in the open field region.
PDWA	Fraction of the charged fps that hit the wall.
ETAV	The average superthermal fp energy (keV).
TAUSD	The average slowing down time for the confined fps (sec).
TAUP	The average confinement time for the fps (sec).
CLNE1	The Coulomb logarithm for ion-electron interactions in the closed field region.
CLNI1	The Coulomb logarithm for ion-ion interactions in the closed field region.
NLC	The number of the test particles that were in the loss cone (i.e., unconfined at birth).
CLNE2	The Coulomb logarithm for ion-electron interactions in the open field region.
CLNI2	The Coulomb logarithm for ion-ion interactions in the open field region.
NSTOP	The total number of histories that were calculated.

TABLE B4

Condensed Version of the Output File Generated by the

Data File Shown in Table B2

```
radial starting positions
  0.524     0.637     0.707     0.765     0.821     0.891

starting angle cosines
 -0.540    -0.281    -0.089     0.089     0.281     0.540

particle histories that were found to be in the loss fraction
      7        12        17        22        27        47        52        57        87       122
    152       157       162       182       187       192       197       202       217       222
    227       232       237       257       262       267       297       332       362       367
    372       392       397       402       407       412       427       432       437       442
    447       467       472       477       502       507       512       537       542       547
    572       577       582       602       607       612       617       622       637       642
    647       652       657       672       677       682       687       692       712       717
    722       747       752       757       777       782       787       792       797       812
    817       822       827       832       847       851       852       856       857       861
    862       867       882       887       892       897       902       917       922       927
    932       937       952       957       962       967       972       987       992       997
   1002      1007      1022      1026      1027      1031      1032      1036      1037      1042
   1052      1056      1057      1061      1062      1066      1067      1071      1072      1076
   1077      1082      1087      1091      1092      1096      1097      1101      1102      1106
   1107      1111      1112      1117      1122      1126      1127      1131      1132      1136
   1137      1141      1142      1146      1147      1152      1157      1161      1162      1166
   1167      1171      1172      1176      1177      1181      1182      1187      1192      1196
   1197      1201      1202      1206      1207      1211      1212      1216      1217      1222
   1227      1231      1232      1236      1237      1241      1242      1246      1247      1251
   1252      1257

    nit nstop    etav        fdrg        fpas        drgen       dvxsq       dvrsq
      0     0 3.670e+03 0.          0.          1.000e+04 4.594e-01 4.594e-01
   1000   117 1.457e+03 5.367e-04 7.101e-04 2.948e+04 2.252e-01 4.560e-01
   2000   403 9.796e+02 9.690e-04 1.746e-03 2.948e+04 2.332e-01 4.608e-01
   3000   667 8.182e+02 6.688e-04 1.270e-03 1.783e+04 2.386e-01 4.733e-01
   4000   876 6.856e+02 8.140e-04 1.603e-03 1.783e+04 2.445e-01 4.783e-01
   5000   983 6.572e+02 6.191e-04 1.219e-03 1.198e+04 2.512e-01 4.952e-01
   6000  1027 6.872e+02 6.697e-04 1.361e-03 1.414e+04 2.215e-01 4.701e-01
   7000  1046 6.190e+02 7.128e-04 1.479e-03 1.414e+04 2.615e-01 4.556e-01
   8000  1059 5.227e+02 6.462e-04 1.323e-03 1.689e+04 2.873e-01 4.577e-01
   9000  1063 4.543e+02 5.827e-04 1.177e-03 1.224e+04 6.409e-02 4.130e-01
  10000  1066 2.561e+02 6.359e-04 1.395e-03 6.648e+03 2.295e-01 2.910e-01
  10297  1068 1.764e+02 8.238e-04 1.930e-03 5.129e+03 2.295e-01 2.910e-01

 the superthermal particle energy distribution is  [e,f(e)]
[    92.,   0.41][   275.,   4.02][   459.,   5.37][   642.,   5.67][   826.,   6.02]
[  1009.,   6.17][  1193.,   6.43][  1376.,   6.32][  1560.,   6.40][  1743.,   6.63]
[  1927.,   6.40][  2110.,   6.29][  2294.,   6.36][  2477.,   6.34][  2661.,   6.22]
[  2844.,   6.08][  3028.,   6.06][  3211.,   5.98][  3395.,   5.81][  3578.,   5.69]

 the ptheta distribution at the cutoff, energy is  [pth,f(pth)]

[-0.360,   0.0][-0.338,   0.0][-0.316,   0.0][-0.294,   0.0][-0.272,   0.0]
[-0.250,   0.0][-0.228,  13.6][-0.206,  74.9][-0.184, 114.0][-0.162, 174.5]
[-0.140, 143.1][-0.118, 107.8][-0.096,  69.8][-0.073,  50.3][-0.051,  36.8]
[-0.029,  57.1][-0.007, 106.6][ 0.015,  70.3][ 0.037,   8.2][ 0.059,   0.0]
```

```
      additional parameters for this case
      bvac =   60.000          rhv  =  18.000            vtot = 4.85348e-02
      tauc = 2.17147e-08      delt  = 6.78584e-10         ndt =           32
      ti-1 =   60.000          te-1 =  56.900            den1 = 7.22286e+14
       t-2 = 5.00000e-02      den2  = 5.00000e+12        rtst =  1.0000
      fion = 0.74426          felc  = 0.25573             fac = 0.83836
      fhcf = 0.57840          fhof  = 0.243 4            fnlc = 0.17774
      pdcf = 0.60555          pdlc  = 0.39444            pdwa = 0.00000
      etav =   1973.4        tausd  = 7.37972e-02        taup = 6.25519e-02
     clne1 =   18.254        clni1  =  21.252             nlc =          192
     clne2 =   13.346        clni2  =  19.783           nstop =         1068

      relative heating profile for constant r values

  0.33   0.57   0.73   0.86   0.98   1.08   1.18   1.26   1.35   1.42   1.50   1.57
 = = = = = = = = = = = = = = = = = = = = = = = = = = = = = = = = = = = =
  0.16   0.01   0.00   0.00   0.00   0.00   0.00   0.00   0.00   0.00   0.00   0.00
  0.22   0.01   0.00   0.00   0.00   0.00   0.00   0.00   0.00   0.00   0.00   0.00
  0.42   0.03   0.00   0.00   0.00   0.00   0.00   0.00   0.00   0.00   0.00   0.00
  0.64   0.10   0.00   0.00   0.00   0.00   0.00   0.00   0.00   0.00   0.00   0.00
  1.08   0.31   0.01   0.00   0.00   0.00   0.00   0.00   0.00   0.00   0.00   0.00
  1.58   0.87   0.11   0.00   0.00   0.00   0.00   0.00   0.00   0.00   0.00   0.00
  0.79   1.74   0.59   0.05   0.00   0.00   0.00   0.00   0.00   0.00   0.00   0.00
  0.18   1.26   1.69   0.42   0.02   0.00   0.00   0.00   0.00   0.00   0.00   0.00
  0.40   0.73   1.39   1.41   0.14   0.00   0.00   0.00   0.00   0.00   0.00   0.00
  0.68   1.59   1.52   2.37   0.63   0.02   0.00   0.00   0.00   0.00   0.00   0.00
  0.84   2.73   2.46   2.23   1.46   0.11   0.00   0.00   0.00   0.00   0.00   0.00
  1.11   4.12   4.28   2.15   2.25   0.36   0.00   0.00   0.00   0.00   0.00   0.00
  1.46   5.18   6.19   3.15   2.51   0.85   0.03   0.00   0.00   0.00   0.00   0.00
  1.62   6.24   7.85   4.55   2.49   1.36   0.06   0.00   0.00   0.00   0.00   0.00
  1.73   6.75   8.98   5.31   2.50   1.63   0.08   0.00   0.00   0.00   0.00   0.00
  1.74   6.93   8.80   5.03   2.48   1.62   0.07   0.00   0.00   0.00   0.00   0.00
  1.62   6.28   7.85   4.45   2.58   1.32   0.05   0.00   0.00   0.00   0.00   0.00
  1.59   5.30   6.24   3.17   2.56   0.82   0.02   0.00   0.00   0.00   0.00   0.00
  1.21   4.22   4.42   2.17   2.23   0.37   0.00   0.00   0.00   0.00   0.00   0.00
  1.01   2.88   2.27   2.22   1.54   0.12   0.00   0.00   0.00   0.00   0.00   0.00
  0.65   1.57   1.47   2.35   0.61   0.03   0.00   0.00   0.00   0.00   0.00   0.00
  0.33   0.71   1.98   1.37   0.17   0.00   0.00   0.00   0.00   0.00   0.00   0.00
  0.11   1.24   1.80   0.43   0.02   0.00   0.00   0.00   0.00   0.00   0.00   0.00
  0.74   1.74   0.67   0.08   0.00   0.00   0.00   0.00   0.00   0.00   0.00   0.00
  1.49   0.84   0.13   0.00   0.00   0.00   0.00   0.00   0.00   0.00   0.00   0.00
  1.01   0.28   0.01   0.00   0.00   0.00   0.00   0.00   0.00   0.00   0.00   0.00
  0.63   0.08   0.00   0.00   0.00   0.00   0.00   0.00   0.00   0.00   0.00   0.00
  0.41   0.02   0.00   0.00   0.00   0.00   0.00   0.00   0.00   0.00   0.00   0.00
  0.24   0.01   0.00   0.00   0.00   0.00   0.00   0.00   0.00   0.00   0.00   0.00
  0.17   0.00   0.00   0.00   0.00   0.00   0.00   0.00   0.00   0.00   0.00   0.00

  computer time this run  2:11.7    cpu fraction  0.089
  total computer time  2:11.7

* ** ** ** ** ** ** ** ** ** ** ** ** ** ** ** ** ** ** ** ** ** ** ** *

  radial starting positions
```

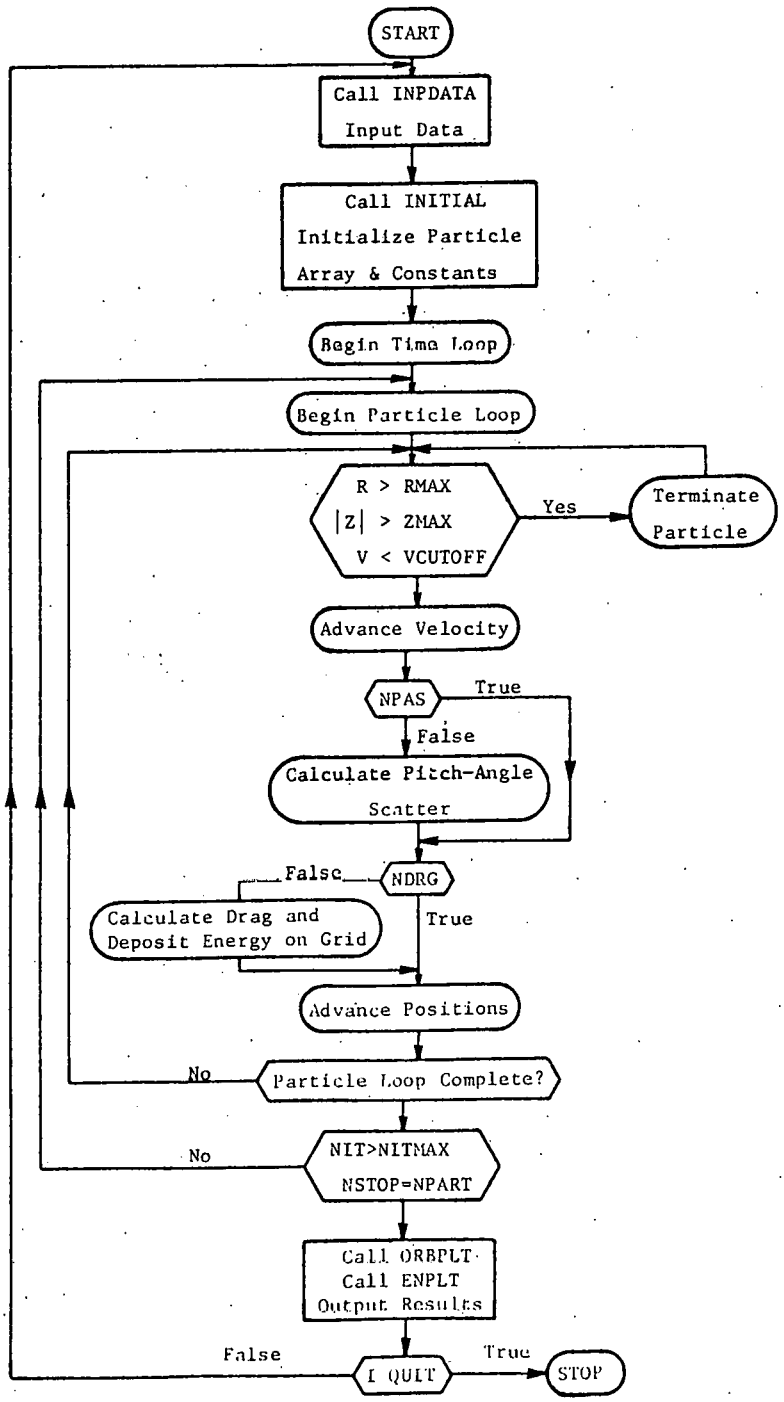

Figure B-1. MCFRM Flow Chart.

VITA

Daniel Edward Driemeyer was [redacted]

He was raised in Edwardsville, IL and attended elementary and secondary schools there, graduating from Edwardsville Sr. High School in May of 1970. In September of 1970 he entered the University of Illinois at Urbana-Champaign, and in May of 1974 he completed the requirements for a B.S. degree in Computer Engineering, graduating with high honors. During his undergraduate work, he was nominated for membership in several honorary societies including Pi Eta Sigma, Eta Kappa Nu, and Sachem.

Having been awarded a nine month AEC traineeship, he entered the graduate program in Nuclear Engineering at the University of Illinois in June of 1974 and received an M.S. degree in August of 1975. Throughout the remainder of his graduate work, he served as a research assistant in the Fusion Studies Laboratory, except for the summer of 1978 when he was employed as a Computational Physicist at Lawrence Livermore Laboratory, Livermore, CA. He has co-authored numerous papers relating to his research work on advanced-fuel fusion reactor concepts and received an award for the best student contributed paper at the spring 1979 meeting of the Mathematics and Computation Division of the American Nuclear Society. He is currently a member of the Fusion Energy group at McDonnell Douglas Astronautics Company, St. Louis, MO.